DEPARTMENT OF COMMERCE
LUTHER H. HODGES, Secretary

WEATHER BUREAU
F. W. REICHELDERFER, Chief

MONTHLY WEATHER REVIEW

JAMES E. CASKEY, JR., Editor

Volume 89, Number 11 | Washington, D.C. | November 1961

ANALYSIS OF SATELLITE INFRARED RADIATION MEASUREMENTS ON A SYNOPTIC SCALE [1,2]

MELVIN WEINSTEIN, LT. COL., USAF [3]
Air Weather Service
and
VERNER E. SUOMI
University of Wisconsin, Madison, Wis.

[Manuscript received May 22, 1961; revised September 12, 1961]

ABSTRACT

Long-wave radiation loss maps, based on Explorer VII measurements of terrestrial radiation at night, are analyzed and compared with composite nephanalyses and frontal analyses. Results indicate a definite relationship between the radiation centers and their corresponding surface low and high pressure centers, their locations, 24-hour intensifications and movements, and the conformity of these movements to the 500-mb. geostrophic flow. Some of the potential applications to analysis and forecasting are noted.

1. INTRODUCTION

The radiation-balance experiment aboard the International Geophysical Year satellite, 1959 Iota (Explorer VII) was developed by a University of Wisconsin team and is described in [8].

The primary purpose of the experiment is to measure the solar, reflected, and terrestrial radiation currents to obtain the radiant heat flow to and from the earth, and ultimately to obtain a clearer understanding of the driving force behind the circulation of the atmosphere. Observations of the long-wave radiation currents from the shadow zone portion of the earth measured by the omnidirectional bolometer were used to draw composite radiation loss maps. The relationship of these maps to other meteorological analyses and parameters and their application to analysis and forecasting are described in this paper.

[1] This research was supported by the National Aeronautics and Space Administration under contract no. NASw-65 and the National Academy of Sciences as part of the International Geophysical Year.

[2] A portion of the material contained in this paper is from a thesis by Melvin Weinstein submitted in partial fulfillment of the requirements for the degree of Master of Science at the University of Wisconsin.

[3] Present address Air Weather Service Member, Meteorological Satellite Laboratory, U.S. Weather Bureau, Washington 25, D.C.

2. LONG-WAVE RADIATION LOSS MAPS

RADIATION OBSERVATIONS

The satellite's orbit is inclined 50.3° to the earth's equator and varies in altitude from 1,100 km. at apogee to 550 km. at perigee. During the period studied, early December 1959, the satellite came out of the sun at 50° N., traveled southeastward and entered the sunlight zone in the Southern Hemisphere. The orbital period is 101 minutes and radiation observations are taken every 42 seconds, during which the satellite travels 2.5° of latitude (fig. 1). Limitations of this orbit are the restriction of observations to between 50° N. and S., the variation of local time along the orbit, and scarcity of observations at lower latitudes.

The spherical sensor integrates the radiation received from the entire field of view. The amount received from a unit area of the earth is weighted according to its position with respect to the satellite, being inversely proportional to the square of the distance from the point on earth to the satellite and directly proportional to the cosine of the angle between the local zenith and a line to the satellite as observed from that point [3]. For example, at satellite altitude of 700 km. the total radius

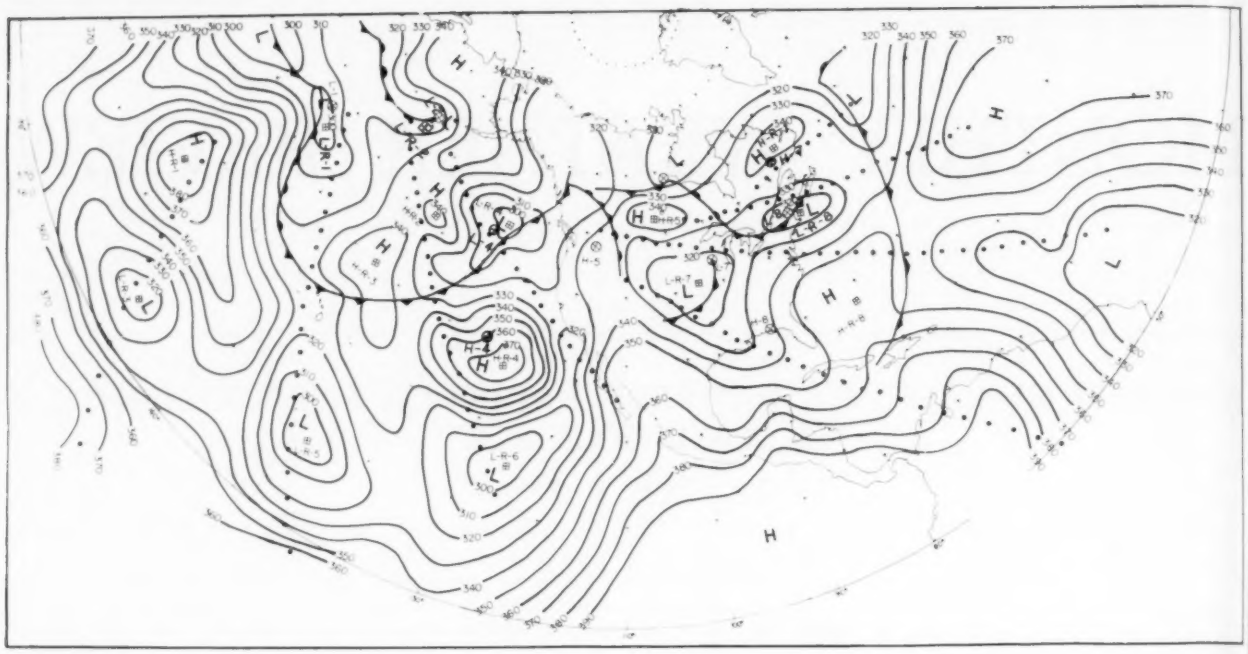

FIGURE 1.—Long-wave radiation loss map, December 1, 1959. Lines are isolangleys, connecting equal long-wave radiation loss values in Langleys per minute $\times 10^{-3}$. Surface pressure centers and fronts are composite to the satellite passage time. Surface pressure centers, marked by circles, are designated L for Low and H for High, plus an Arabic number (thus L–1). Radiation centers, marked by squares, are distinguished from surface centers by the inclusion of R (thus L–R–1 is radiation Low number 1 which is associated with surface Low L–1). Satellite observation points and orbit path are shown by dots.

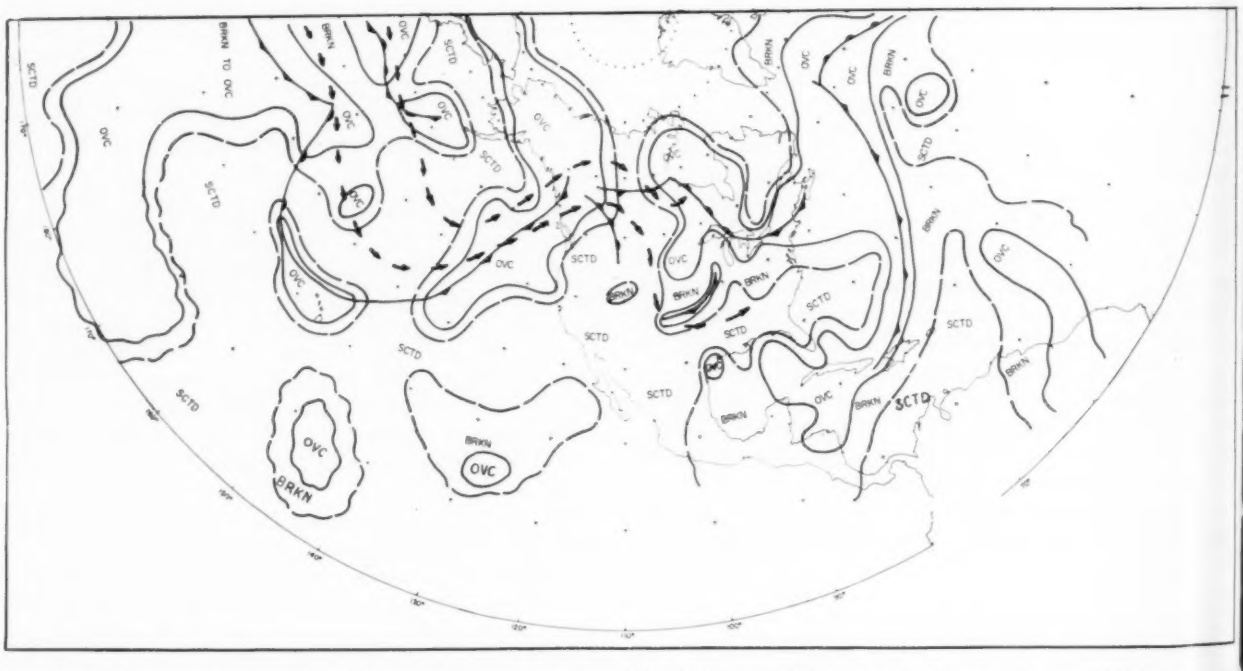

FIGURE 2.—Composite nephanalysis, December 1, 1959, based on 0000, 0600, and 1200 GMT surface maps. Overcast (OVC) areas are enclosed within solid lines. Broken lines separate the clear to scattered (SCTD) areas from the broken, 5/8 to 7/8 (BRKN). Wavy lines indicate the actual cloud area edge is unknown due to lack of data. Arrows show regions of maximum winds, from the 0000 GMT 300-mb. chart.

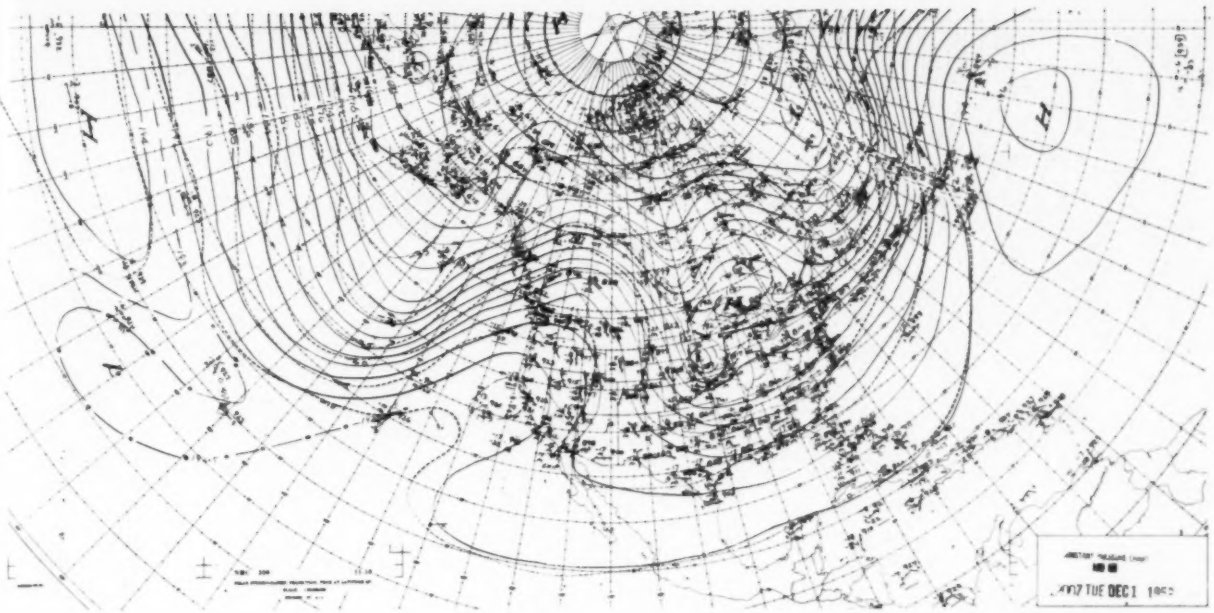

FIGURE 3.—500-mb. map, 1200 GMT, December 1, 1959.

of the circular area viewed on the earth is 25.8° of latitude (2,855 km.) measured from the subsatellite point. However, 50 percent of the radiation comes from a relatively small area whose radius is 6.6° of latitude and which comprises only 7.6 percent of the total area viewed. Nine-tenths of the radiation comes from only 33.2 percent of the area viewed [4]. As a result, the changes in radiation are heavily weighted toward the area just below the satellite.

The surface of the earth or of a cloud radiates essentially as a black body. A portion of this radiation is transmitted through the atmosphere and the remainder is absorbed by atmospheric gases, principally CO_2, H_2O, and O_3. The atmosphere itself reradiates energy. In fact, most of the energy leaving the top of the atmosphere comes from the atmosphere itself. Nocturnal radiation measurements were used in this study because radio reception from the satellite is much better at night when there is greater ionospheric transparency. This results in more data and better global coverage. In addition, calculations for the nighttime case are much simpler because the white hemisphere is measuring only long-wave radiation.

The bolometer is a thin hemispherical shell thermally isolated from a mirror large enough so that no part of the satellite itself is seen by the bolometer. Since the satellite is spinning rapidly on an axis parallel to the mirror surface, the hemispherical bolometer acts like a sphere in space. The heat transfer by conduction and long-wave radiation to the mirror is small but not negligible compared to radiative transfer from the earth and to space. The energy balance equation for a spinning mirror-backed hemisphere in space in the shadow zone of the earth reduces to

$$\alpha\beta\frac{R\uparrow}{2}=2\pi\epsilon\sigma T_w^4-H\frac{\partial T}{\partial t}-K(T_w-T_m) \tag{1}$$

$$R\uparrow=\frac{1}{\beta}\left[\frac{4\pi\epsilon\sigma T_w^4}{\alpha}-\frac{2H}{\alpha}\frac{\partial T}{\partial t}-\frac{2K}{\alpha}(T_w-T_m)\right] \tag{2}$$

where $R\uparrow$ is the total radiation received by the bolometer, β is the solid angle to the earth, α and ϵ are the infrared absorptivity and emissivity of the sensor, σ the Stefan-Boltzmann constant, H a term equivalent to the time constant of the sensor, and K the thermal conductivity between the temperatures of the sensor (T_w) and the mirror (T_m).

Actually H is a function of temperature because the heat transfer process, principally radiation, is temperature dependent. K is also temperature dependent because there is radiation exchange between the inside of the hemisphere and the mount. However, in order to simplify the hand calculations, both H and K are assumed to be constant. Even so, since $\alpha=\epsilon$ from Kirchoff's law, the value of the first term in the brackets, the greatest of the three, is determined by the absolute temperature T_w. A most pessimistic value of its error would be ± 1 °C.; a more likely value is about one-fourth of that. However, even an error of 1° C. would give rise to an error of only 2.5 percent in the final value of $R\uparrow$. The satellite altitude and therefore the solid angle β is known to good accuracy. An error of 100 percent in K will give an error of 10 percent in the final result. Finally, while at equilibrium the second term goes to zero, it might be significant

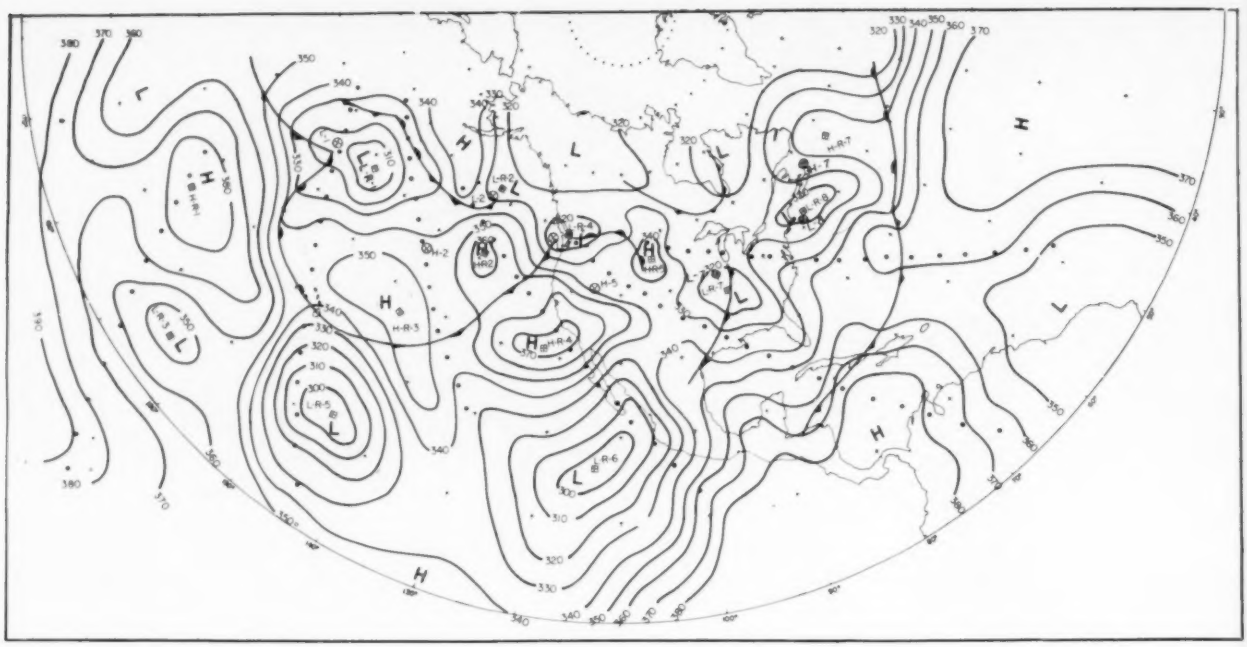

FIGURE 4.—Long-wave radiation loss map, December 2, 1959. (See fig. 1 for legend.)

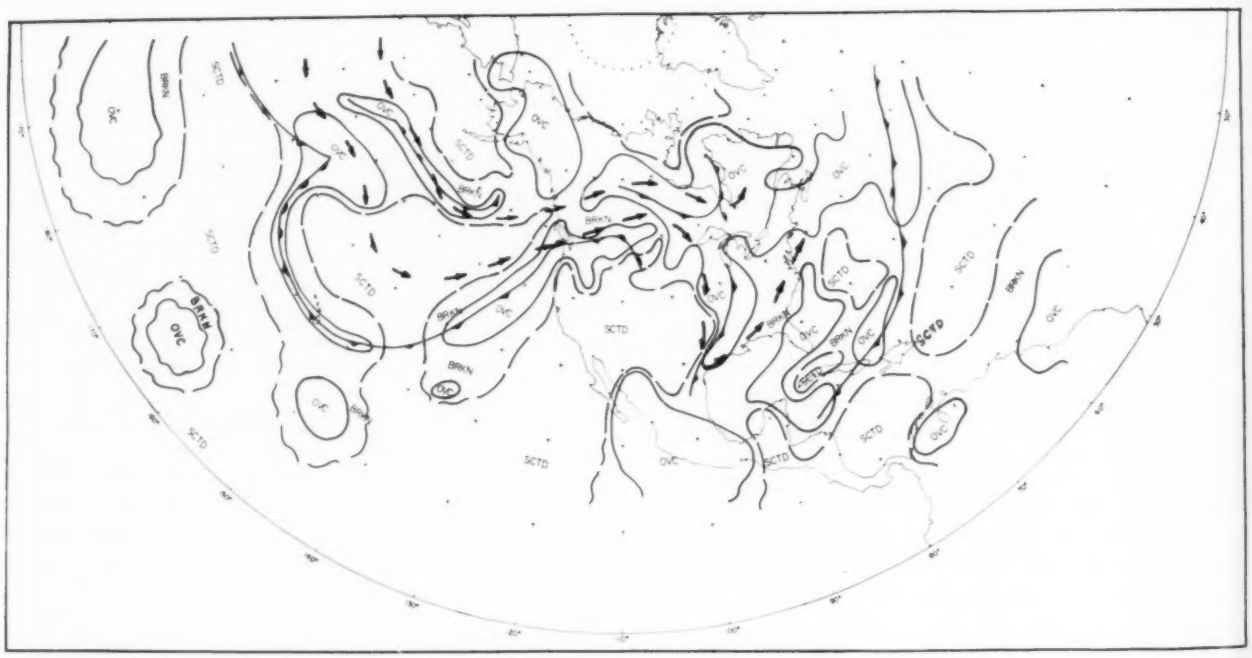

FIGURE 5.—Composite nephanalysis, December 2, 1959. (See fig. 2 for legend.)

just as the satellite comes out of the sun. One is tempted to say, therefore, that the radiation values at 50° N. are probably too high. Our feeling is that it is best to await the more complete calculations being done on a computer. However, it will be a surprise if they differ by more than 10 percent from what we are showing here. In any case these results are sufficient to show changes in the patterns of outgoing radiation.

Thus the radiation observation values used in the long-wave radiation maps are probably within 10 percent of the absolute values. However, the values for three maps which do not cover the complete hemisphere should

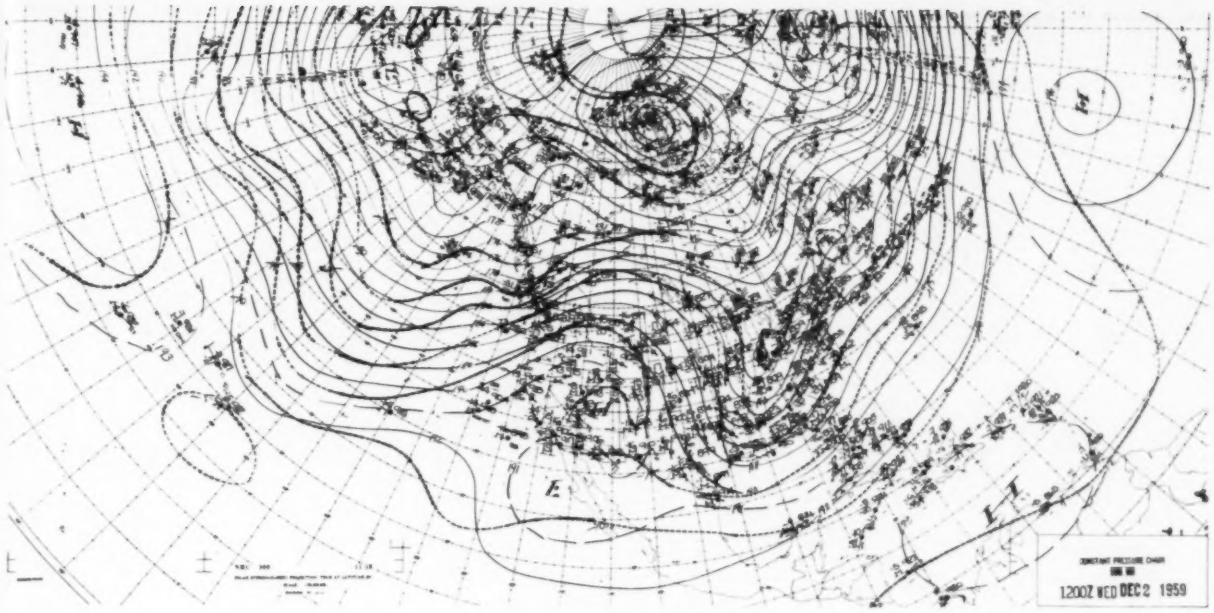

FIGURE 6.—500-mb. map, 1200 GMT, December 2, 1959.

not be used for comparison with average hemispheric values. From a synoptic point of view, the radiation observations are extremely useful because they are comparable to each other relatively so that the radiation patterns and their continuity have meaning.

ANALYSIS PROCEDURE

Because the spherical sensor integrates the radiation over a large segment of the earth, it is possible to draw a composite radiation map using data from successive satellite orbit paths, even though there is a time difference of 1 hour and 40 minutes between orbit paths. Lines of equal long-wave radiation loss, in Langleys per minute $\times 10^{-3}$ (isolangleys) are drawn on the radiation map, using the same principles as those for drawing isobars on a surface map or contours on an upper air map.

Since the radiation maps are not synoptic, composite surface frontal and nephanalysis maps, which coincide as closely as possible with the times of the radiation observations, are constructed based on National Weather Analysis Center analyses. The composite nephanalysis is drawn separating overcast, broken, and clear to scattered areas. Fog and sky-obscured reports are considered as overcast. The lack of data over oceanic and tropical areas is a limiting factor to both composite analyses.

First the radiation maps were drawn as completely and independently as possible. The composite nephanalyses were then drawn. In the areas north of 35° N. to 40° N., where there were sufficient data for independent radiation and nephanalyses, the close relationship between the two analyses was apparent. Hence the nephanalysis, where available, was used to supplement the radiation analysis in those areas where data were sparse. While not an ideal method, it was considered best in these few, early radiation maps to permit as much study as possible of their potential value. With increased density of radiation observations, a completely independent radiation map could be drawn.

It is interesting to note that in those large sections of the oceans and Tropics where there are no surface observations for a nephanalysis, the major source of data was the satellite radiation observations. Because of the large gaps between orbit paths in the Tropics, interpolation in drawing isolangleys is difficult. Here 24-hour continuity in radiation observations proves invaluable.

3. RADIATION MAP FEATURES AND RELATIONSHIPS

The fact that clouds dominate in determining the radiation pattern is apparent when comparing the radiation analyses (figs. 1, 4, and 7) with the nephanalyses (figs. 2, 5, 8) in those areas north of 40° N. where data were sufficient for their independent analysis. Since most mid-latitude extensive cloud systems of variable vertical development are caused by surface low pressure centers and fronts, the resulting radiation map patterns also reflect these sources. Where the surface Low or front is most intense, the cloud tops are higher and colder, and the outgoing long-wave radiation is less. As the cloud tops lower, the radiating temperature rises and the amount of radiation measured by the satellite sensor increases. On the radiation map this results in a radiation Low over the area of maximum cloud development, and higher isolangley values over the area of lower cloud tops. The highest radiation readings are found over

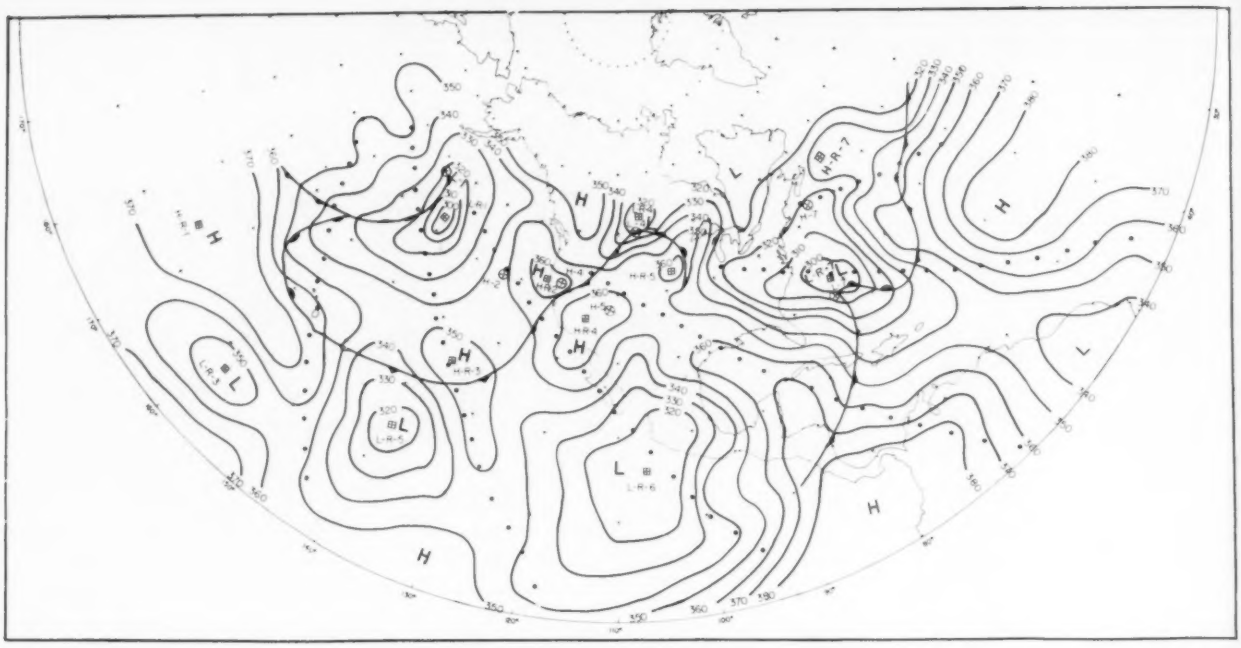

FIGURE 7.—Long-wave radiation loss map, December 3, 1959. (See fig. 1 for legend.)

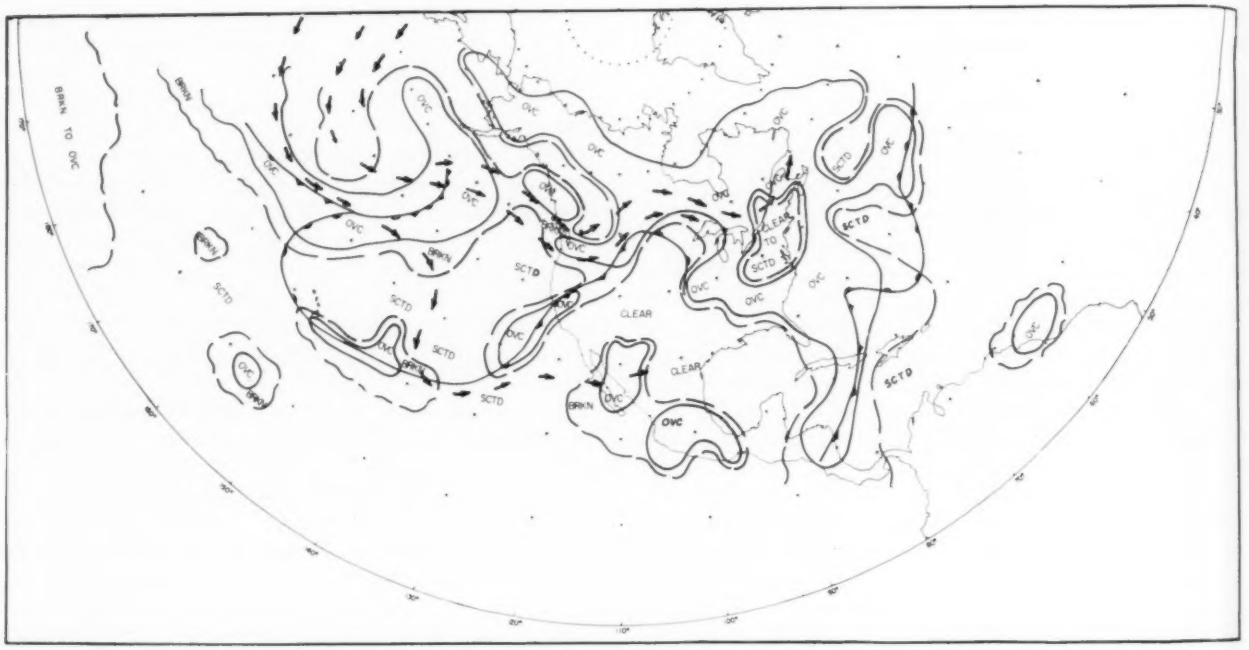

FIGURE 8.—Composite nephanalysis, December 3, 1959. (See fig. 2 for legend.)

the central and eastern sections of surface Highs where clear to scattered conditions generally prevail.

From the above relationships, one would expect to find the radiation low center east of the mid-latitude surface low center and the radiation high center east of the mid-latitude surface high center; and one does find this occurring in 24 of the 25 cases for which data are available (fig. 11).

An example of the usual relationship is radiation Low L–R–1, located southeast of surface Low L–1 and the associated Pacific occlusion on December 3, 1959 (fig. 7). It is interesting to note that the orientation of the radiation

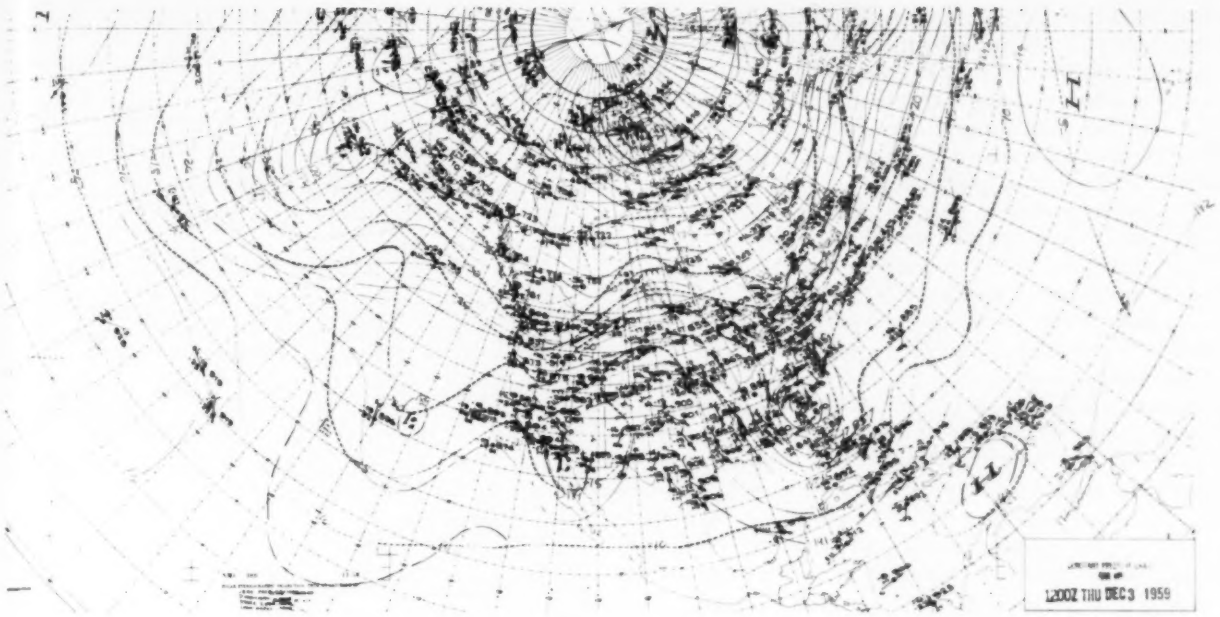

FIGURE 9.—500-mb. map, 1200 GMT, December 3, 1959.

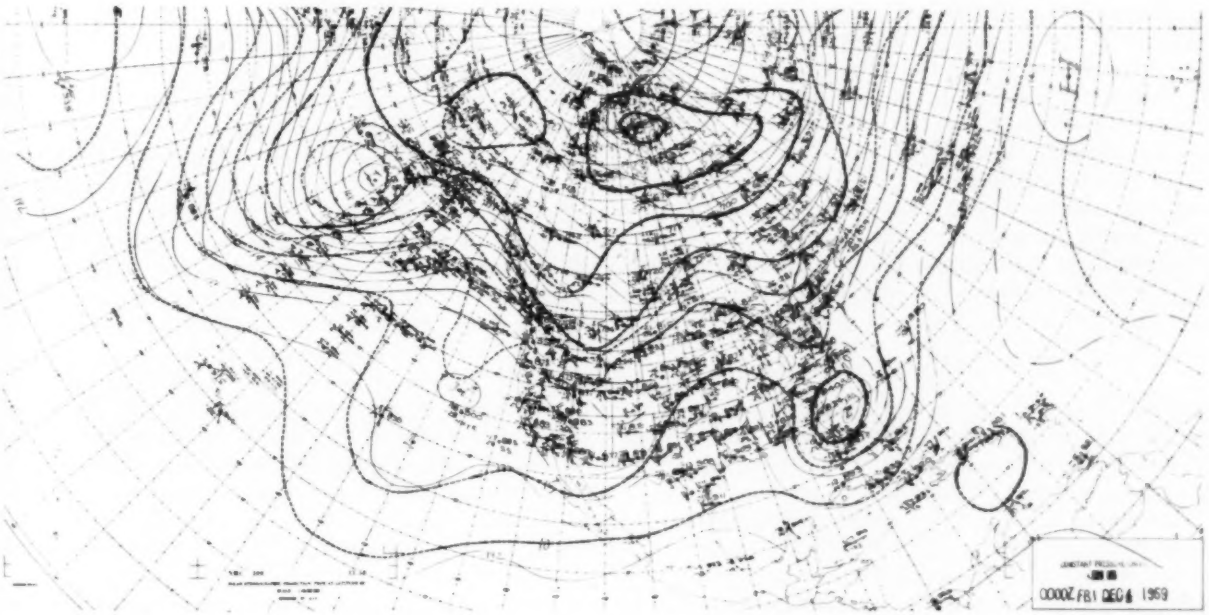

FIGURE 10.—500-mb. map, 0000 GMT, December 4, 1959.

Low and trough parallels the occlusion and area of maximum intensity, and the radiation pattern's spiral-like extension northwestward resembles TIROS cloud photographs of occlusions.

In addition to frontal location, the radiation trough, by its sharpness and strength of isolangley gradient, indicates frontal intensity, and by the interdiurnal change in these criteria, 24-hour frontal changes. An example is the cold front which starts in northwestern Canada from the remnants of an old occlusion and extends southwestward into the Pacific (fig. 1). The radiation map correctly indicates that the front is stronger in the region where its clouds produce L–R–4 and the sharp radiation trough to its southwest, weaker through the area

where radiation High H–R–3 reflects only clear to scattered clouds (fig. 2), and again more intense as it becomes a warm front leading into the unstable wave of surface Low L–1 where the radiation trough strengthens toward L–R–1. The weakening of the radiation trough off the Pacific coast on December 2 (fig. 4) reflects the decreased activity of the surface cold front.

The entire radiation trough pattern from L–R–4 to L–R–1 and then southwestward resembles a cyclone "family" and, in fact, is the radiation map reflection of one. The development of family "member" L–1, from an unstable wave to an occlusion can also be followed on the radiation maps during the succeeding days.

The arrows representing the pattern and location of maximum winds on the U.S. Weather Bureau 0000 GMT 300-mb. maps have been plotted on the nephanalyses. On December 1, 1959, (fig. 2) the maximum upper wind and frontal patterns conformed to that given by [10] and [2] for the relationship of the jet stream to a cyclone family. Again, the radiation patterns of Lows and troughs show the same relationship to the jet stream as do the surface Lows and fronts of the cyclone family.

While a radiation Low is usually the reflection of a surface Low or front, it can also be caused by a cold or snow surface or an extended sheet of high clouds. Both of these sources may generally be distinguishable by radiation map analysis and continuity. There are no snow surfaces indicated in this series of maps. However, it is very likely that extended sheets of high clouds caused the tropical radiation Lows which are not related to identifiable synoptic features. Such large areas of high clouds in the Tropics have been reported by [1, 7, 5, 9]. It is felt that if there were sufficient radiation observations above an easterly wave, the resulting radiation pattern would show a minimum over the high clouds in the convergence area. Synoptic data available do not indicate any easterly waves for these dates.

4. 24-HOUR CHANGES IN INTENSITY

During the intensification of a surface or upper air Low there is an increase in size, vertical development, and meridional expansion of the cloud pattern. These changes are reflected in the radiation pattern.

The changes in value of the radiation center reflect the interdiurnal change in intensity of its surface counterpart for five of eight high centers and four of six low centers studied here (figs. 11a and b). Reasons for the "misses" are difficult to determine but some possiblities are: the pressure changes may have been too small to result in changes in clouds and radiation intensity; the clouds may already have been at maximum height. From the limited examples available, one can say that in all four cases when the 24-hour change in magnitude of the surface Low was greater than 10 mb., the change in radiation Low intensity was in the same sense.

Intensification of a surface center is also indicated by 24-hour shifts in the relative positions of its related radiation center. For example, radiation Low L–R–7 moved from southeast to north-northeast of its intensifying surface Low from December 2 to 3, 1959 (fig. 11a). Limited data in the Pacific indicate that L–R–1 was located east-southeast of surface Low L–1 on December 1, moved to its east-northeast on the 2d, and then to its southeast after occlusion took place. On both dates L–1 deepened. Reasons for the last change are not readily apparent. With an intensifying system such as L–1 moving northeastward, one would normally expect some northward motion of the radiation Low relative to the surface Low, reflecting the movement of highest clouds. However, in this case, the radiation Low and trough were apparently in the region of most intense convergence and vertical motion just ahead of the surface position of the occlusion (figs. 7, 9, 10). It was also noted in the few available cases that radiation Lows related to surface Lows which were weakening or not changing retained their same relative position. L–2 and L–4 and their radiation Lows are good examples.

TABLE 1.—*Surface and radiation center motions*

Radiation center	24-hr. motion (kt.)	Surface center	24-hr. motion (kt.)	500-mb. geostrophic wind	
				At radiation center location (kt.)	Radiation center motion/V_g (percent)
December 1-2, 1959					
H–R–1	E 11	None			
H–R–2	E 22	H–2	ENE 25	W 40	55
H–R–3	SE 19				
H–R–4	NE 20	H–4 to H–2	E 7	Light	
H–R–5	S 16	H–5	SSE 16	NNW 35	46
H–R–6					
H–R–7	ESE 21	H–7	ESE 22	NW 45	45
L–R–1	NE 26	L–1	ENE 24	WSW 45	53
L–R–2	E 35	L–2	E 35	WSW 60	58
L–R–3	E 15				
L–R–4	ENE 26	L–4	ENE 36	SW 65	40
L–R–5	NNE 19				
L–R–6	E 25				
L–R–7	ESE 15	L–7	SE 14	W 35	43
L–R–8					
December 2-3, 1959					
H–R–1	E 11				
H–R–2	E 29	H–2	ENE 32	WNW 50	58
H–R–3	SE 27				
H–R–4	NE 20	H–4 to H–2	NE 22	NW 20	100
H–R–5	SE 10	H–5	SE 11	NW 30	33
H–R–6					
H–R–7					
L–R–1	NE 36	L–1	NE 42	SW 80	45
L–R–2					
L–R–3	E 17				
L–R–4	ENE 31	L–4	E 35	WSW 75	41
L–R–5	NE 18				
L–R–6	E 15				
L–R–7	SE 39	L–7	SE 42	Upper Low extends to 300 mb.	
L–R–8	ESE 11	L–8 to L–7			

Another indication of surface Low intensification, based on radiation map data *alone*, is the change in orientation of a radiation low pattern from east-west to north-south coupled with a decrease in magnitude of the radiation center. This occurred with L–R–1 and L–R–7 over the 3 days of maps. The reverse applies to a weakening system, as exemplified by L–R–2 and L–R–4.

5. 24-HOUR MOTION AND 500-MB. GEOSTROPHIC FLOW

Figures 11a and b and table 1 show a possibly useful

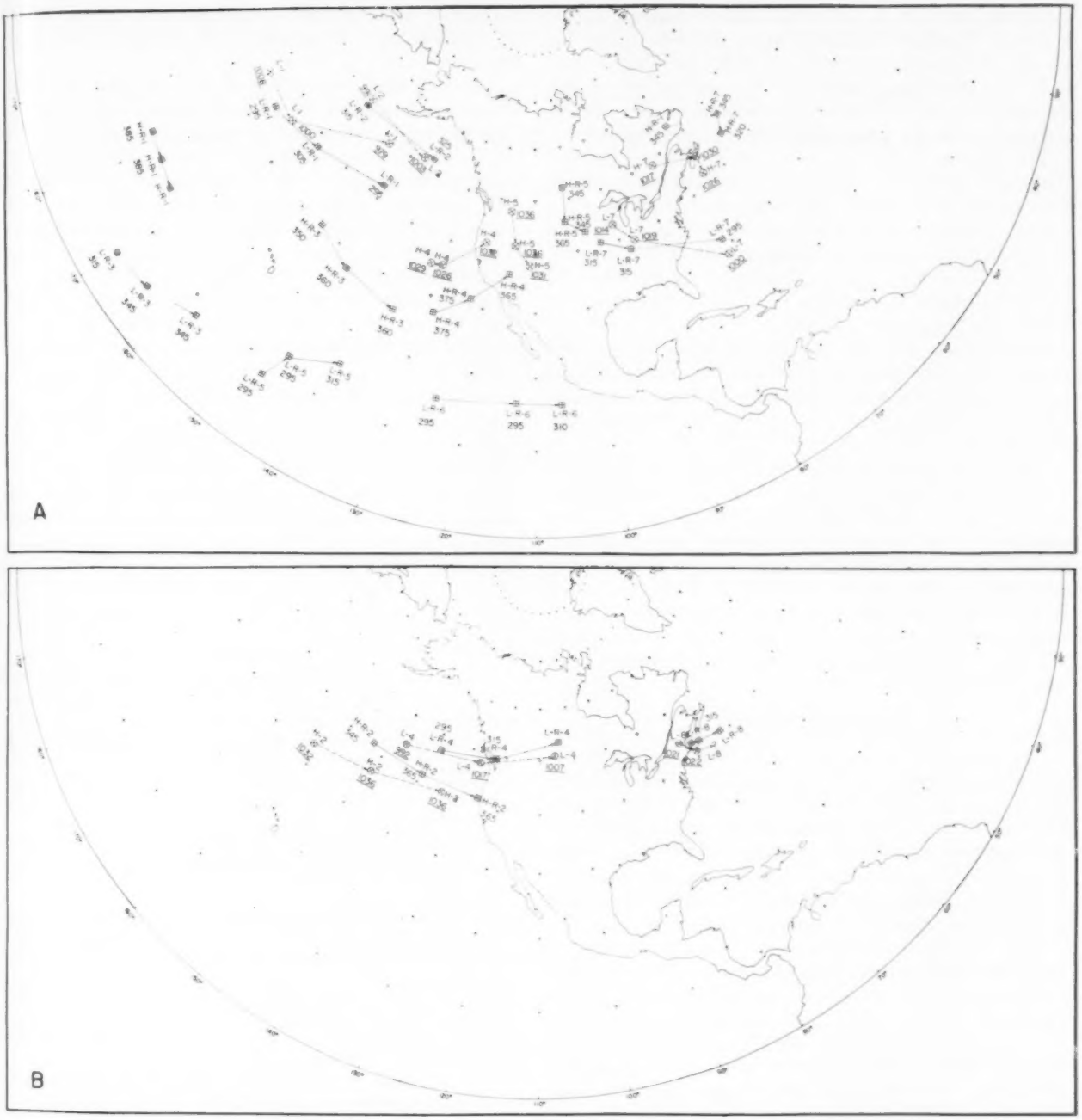

FIGURE 11.—(a) Surface and radiation center continuity, December 1–3, 1959. The surface pressure center locations are indicated by circles, their values in millibars are underlined, and their 24-hour locations are connected by a dashed line. The radiation center locations are indicated by squares, their values are in Langleys per minute $\times 10^{-3}$, and their 24-hour locations are connected by a solid line. (b) Additional surface and radiation center continuity, December 1–3, 1959.

relationship between the interdiurnal movements of the mid-latitude surface and associated radiation Lows and Highs. The 24-hour motion of six of the seven radiation Highs available for study was within about 20° and 10 kt. of that of their related surface system. The seventh example, comparing the motions of H–R–4 and H–4, is complicated by H–4's becoming absorbed in surface High H–2. The 24-hour movements of *all seven* radiation Lows followed that of their surface Low within these same limits.

A positive relationship is found between the 24-hour motion of the radiation low center and the average 500-mb. geostrophic wind velocity over its area of motion.

613342—61——2

Computations were made from contour spacings on the National Weather Analysis Center 500-mb. maps for December 1 through 4, 1959 (figs. 3, 6, 9, 10). The motions of four of seven radiation Highs were within 20° of the direction and between 40 and 60 percent of the speed of the related 500-mb. geostrophic wind velocity (table 1).

The radiation Lows' motions show even better correlation. *Six of the seven cases* for which data are available were within these limits. The seventh case involves the intense surface Low L–7 and radiation Low L–R–7 on December 3. A closed Low also developed in the upper air maps to at least 300 mb. (highest level available for study) and hence the 500-mb. level cannot be considered a "steering" map for that system.

These results indicate that the radiation low center's motion could be used to determine the 500-mb. flow pattern, and the approximate location of the corresponding surface Low center, its movement, and possible changes in its intensity.

The cirrus clouds causing the tropical radiation Lows were probably between 12 and 16 km. Although the 500- and 300-mb. analyses extend only to 15°–20° N., the contour pattern indicates the westerly flow continued farther south at these and higher levels, causing the generally eastward motion of H–R–1, L–R–5, and L–R–6. L–R–3 could have been under the influence of the equatorial westerlies which, according to [6], can extend to 16 km. These subtropical centers also showed good continuity (fig. 11a).

6. CONCLUSIONS

The relatively simple omnidirectional white radiation sensor aboard Explorer VII measures long-wave radiation at night which, when converted to Langleys per minute, can be used to produce radiation maps. In mid-latitudes, where adequate data exist, the radiation pattern is consistent with the nephanalysis pattern and with synoptic features. Analysis techniques are similar to those presently used for surface and upper air maps.

The radiation map appears to offer many aids to analysis and forecasting, particularly for areas of sparse data, which should be confirmed by further study. Best results are for the mid-latitude low center relationships. The radiation low center gives an approximation of the location, motion, and change of intensity of the surface low center. In addition, in limited areas where the direction of motion of the radiation Low is available, the upper air pattern and 500-mb. winds may be approximated. A special synoptic situation, the cyclone family, is recognizable and the general location of the associated maximum winds may be determined. In all latitudes the radiation analysis whether determined by radiation data alone, nephanalysis alone, or a combination of both, shows good continuity (figs. 11a and b).

It may also be possible to determine vertical motion patterns from the radiation map patterns, particularly when combining the low resolution, quantitative radiation map figures from Explorer VII with the high resolution, qualitative cloud pictures from TIROS. Research on this relationship is being conducted at the University of Wisconsin.

Radiation measurements from two satellites in polar orbits would increase observation density and make the maps more nearly synoptic, increasing their accuracy and value. Data storage capability aboard a single satellite would make it possible to have radiation maps for the entire earth using just single, or a few, readout stations.

The conclusions arrived at are based on data not always as complete as desirable and on maps which are both nonsynoptic and few in number. However, these limitations are mitigated by the consistency of the relationships over the 3-day period and, in the northern latitudes, by the density of radiation observations which lessened subjectivity.

ACKNOWLEDGMENTS

It is not possible to acknowledge individually the very many persons who made the satellite flight, data collection and reduction, and radiation map analysis possible even though their contribution is enormous. To avoid any possible unintentional omission we wish to acknowledge the large contribution and support given by the National Aeronautics and Space Administration, the National Academy of Sciences, the U.S. Weather Bureau, the University of Wisconsin, and the U.S. Air Force Air Weather Service.

REFERENCES

1. A. E. Cole, "Clouds," *Handbook of Geophysics for Air Force Designers*, 1st Ed., U.S. Air Force, Geophysics Research Directorate, 1957, pp. 7-1—7-7.
2. A. H. Glaser, "Meteorological Utilization of Images of the Earth's Surface Transmitted from a Satellite Vehicle," Report under contract AF 19(604)-1589, (AFCRC TR-57-241, ASTIA-AD-146764), Harvard University, Blue Hill Meteorological Observatory, Milton, Mass., 1957, 145 pp.
3. L. Holloway, "Correcting for Unavoidable Smoothing of Artificial Satellite Data," Paper presented at 155th Meeting, American Meteorological Society, Washington, D.C., April 29–May 2, 1957.
4. F. B. House, "On the Interpretation of Long-Wave Radiation Data from Explorer VII Satellite," Paper being prepared at University of Wisconsin, Department of Meteorology, Madison, Wis.
5. H. M. Johnson, "Use of Satellite Data in Tropical Meteorology," Semiannual technical summary report No. 1, contract AF 19(604)-6156, prepared for U.S. Air Force, Geophysics Research Directorate, Bedford, Mass., July 1960, 25 pp.
6. C. E. Palmer, "The General Circulation between 200 mb. and 10 mb. over the Equatorial Pacific," *Weather*, vol. 9, No. 11, Nov. 1954, pp. 341-349.
7. R. G. Stone, "A Compendium on Cirrus and Cirrus Forecasting," *Air Weather Service Technical Report 105-130*, U.S. Air Force, Mar. 1957, 156 pp.
8. V. E. Suomi, "The Thermal Radiation Balance Experiment on Board Explorer VII," Chap. 11 in *JUNO II Summary Project Report*, vol. III, Explorer VII, NASA, George C. Marshall Space Flight Center, Huntsville, Ala., 1960, pp. 247-278.
9. V. E. Suomi and P. M. Kuhn, as yet untitled paper on infrared radiometer soundings in the Caribbean, 1961.
10. J. Vederman, "The Life Cycles of Jet Streams and Extratropical Cyclones," *Bulletin of the American Meteorological Society*, vol. 35, No. 6, June 1954, pp. 239-244.

SATELLITE PICTURES AND METEOROLOGICAL ANALYSES OF A DEVELOPING LOW IN THE CENTRAL UNITED STATES[1]

ANDREW TIMCHALK AND LESTER F. HUBERT

Meteorological Satellite Laboratory, U.S. Weather Bureau, Washington, D.C.

[Manuscript received May 1, 1961; revised July 28, 1961]

ABSTRACT

TIROS I satellite pictures for a 3-day period about a developing "Low system" over the central United States are shown. Cloud distribution about surface fronts and upper-air troughs was examined and compared to the "ideal" (classical) distribution. The pictures and analyses reveal that cloud patterns were significantly changed by strong subsidence and advection of dry air along a low-level wind maximum. The cloud patterns when compared to the 600-mb. vertical motions computed routinely by the Joint Numerical Weather Prediction Unit showed only partial agreement.

A strong relationship between low cloud cover and surface relative humidity was found; this relationship may be useful under certain conditions in determining the stability of the air over areas where upper-air data are sparse.

1. INTRODUCTION

This study was undertaken to investigate the cloud distribution, as indicated by satellite pictures in addition to the usual synoptic methods, for several stages in a developing low pressure system in the central United States. Analyses of the pictures and meteorological data were made in the following manner:

1. Latitude-longitude grids were drawn and superimposed on selected satellite pictures taken over the low pressure system on May 19 through May 21, 1960.

2. To the pictures were added surface analyses and selected data. For example see figure 1.

3. Surface analyses and upper-air analyses were made. (Only the surface maps are shown with the 500-mb. trough positions superimposed.) For example see figure 3b.

4. Simplified schematic diagrams made from cloud pictures were transferred to polar stereographic maps of cloud data and frontal positions. Over the United States cloud types were taken from the nearest 3-hourly observation time (i.e., 1800 or 2100 GMT). For example see figure 3a.

5. The relationships between cloud distribution and (a) synoptic situation, (b) low-level wind maximum, (c) vertical motions, (d) surface relative humidity, were examined for each of the three days.

2. CLOUD DISTRIBUTIONS AND ANALYSES, MAY 19, 1960

Figures 1 and 2 picture the cloud fields which are schematically represented on figure 3a. Figure 3b is the corresponding surface analysis with the 500-mb. trough position superimposed.

SYNOPTIC SITUATION

Figure 3a shows that the bulk of the cloudiness associated with the surface cold front lay well to the rear of the front and to the northwest of the wave centered in southern Kansas. Further, the region immediately about and ahead of the cold front was clear, with the exception of the small zones of scattered to broken cumulus clouds. This type of distribution differs completely from the "ideal" distribution model [1] in which the bulk of the cloudiness lies ahead of the cold front with rapid clearing to the rear.

The bulk of the cloudiness to the rear of the cold front was located in and ahead of the 500-mb. trough and agreed with the findings of Oliver and Oliver [2] that clouds are located at and ahead of their respective upper-air troughs. There were small zones of cloudiness behind the 500-mb. trough; these however, were probably the result of orography since they lay over the highest peaks of the Rockies.

The brightness and high reflectivity of the homogeneous-appearing clouds immediately ahead of the warm front (fig. 2) can probably be attributed to the high water content of the clouds since continuous precipitation was reported in this area. This low cloud mass, whose trailing edge coincided closely with the surface warm front, extended about 300 miles ahead of the front where the cloud deck abruptly rose to 10,000 ft. or higher and extended about 600 mi. ahead of the front. This cloud distribution conformed nicely with the "ideal" warm frontal model [1].

LOW-LEVEL WIND MAXIMUM

At 1800 GMT, May 19, a low-level wind maximum at 5,000 ft. was located near Louisville, Ky. and extended into upper Michigan. A weaker wind maximum (about 30–40 kt.) also at 5,000 ft. extended through central

[1] This research has been supported by the National Aeronautics and Space Administration.

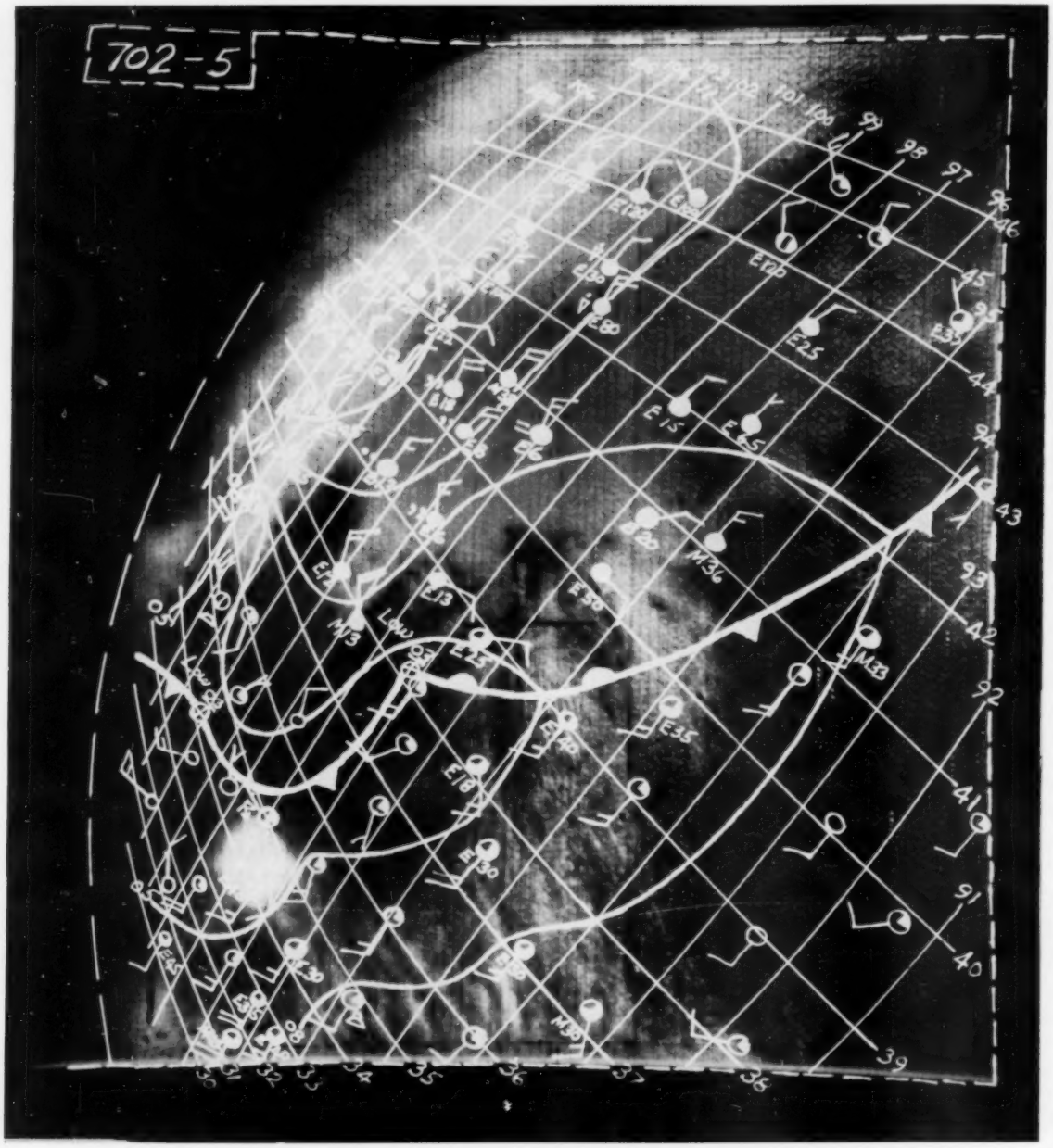

FIGURE 1.—TIROS picture for 2001 GMT, May 19, 1960 with data and latitude-longitude grids superimposed.

Texas and northward into Oklahoma and southern Kansas. At this time however, there was no apparent relationship between the cloud distribution and the wind maximum.

VERTICAL MOTIONS

The 600-mb. vertical motions, as computed by the Joint Numerical Weather Prediction Unit (JNWP) and interpolated linearly for 2000 GMT, May 19, showed that clouds were found in areas of computed downward motion and that clear to scattered regions were located in areas of computed upward motion. The magnitude of these motions was small. For example, in the area of the "square cloud" (fig. 1 at 34° N., 99° W.), which is believed to have been a tornado-producing cloud [3], the computed upward motion was only 1 cm. sec.$^{-1}$ The comparison of the computed vertical motions with cloud pictures in this

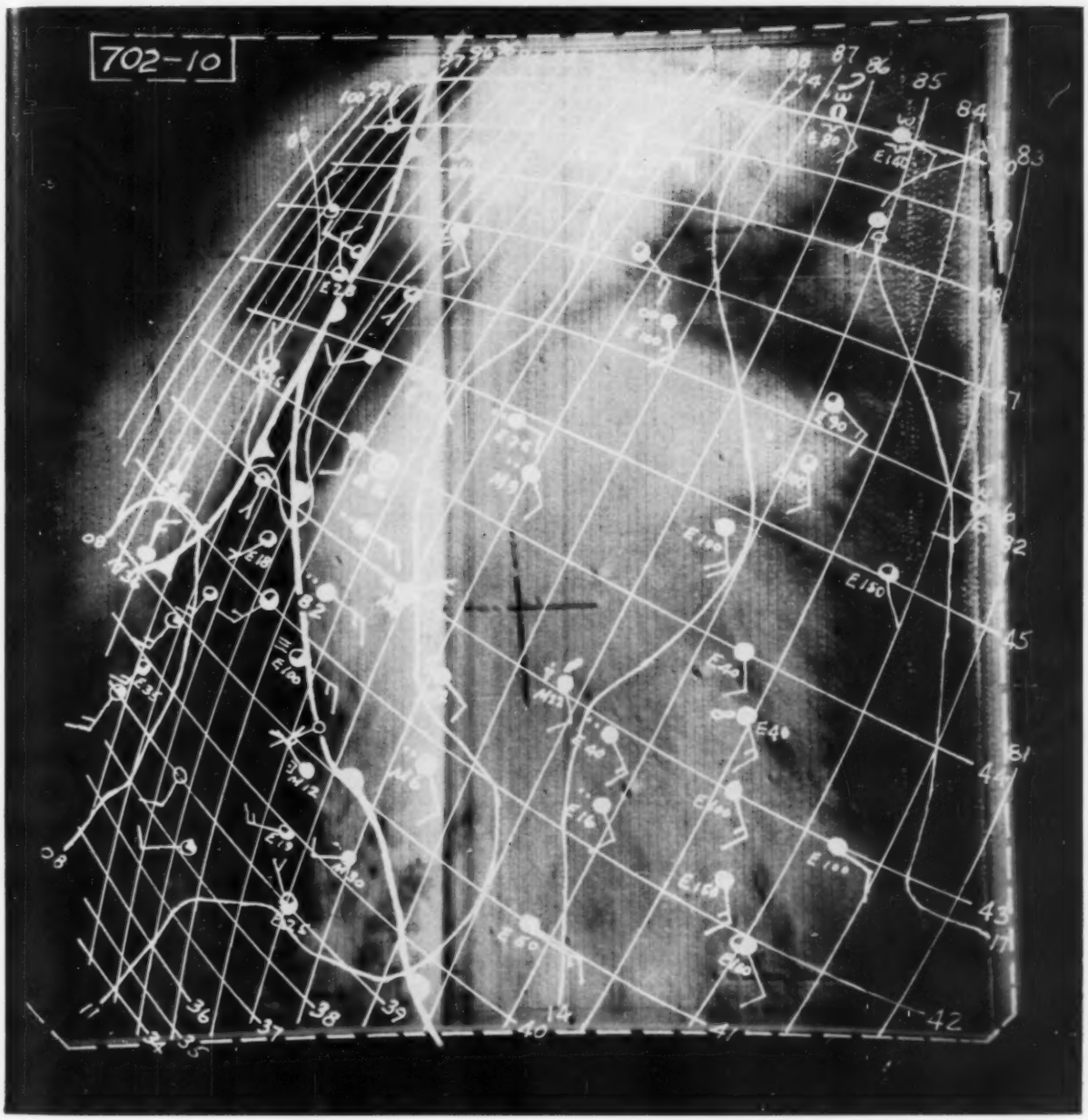

FIGURE 2.—TIROS picture for 2003 GMT, May 19, 1960 with data and latitude-longitude grids superimposed.

case may not be valid due to the fact that vertical motions computed with the present JNWP model reflect only large-scale motion, while cloud fields are frequently produced by mesoscale systems and convective overturning.

SURFACE RELATIVE HUMIDITY

During the course of this study, it was noticed that the surface relative humidity patterns were well correlated with cloud cover below 5,000 ft. Although the low clouds on all three days largely reflected the influence of afternoon convection, some low ceilings occurred with fronts where the same humidity relationship was evident, though less marked.

A reasonable explanation may be that in areas where surface heating produces convection, a mixed subcloud layer should display the same humidity pattern at the surface and at cloud level. Even under frontal clouds, mixing may occur in the subcloud layer, but it is likely that higher humidities might be produced by the cloud

FIGURE 3.—(a) Schematic nephanalysis 2001-2003 GMT, May 19, 1960. Opaque-appearing broken and overcast regions are represented by hatching and stippling, respectively. Clear, scattered, and hazy-appearing areas are left unshaded. (b) Surface data and analysis 2000 GMT, May 19. (c) Broken (hatched) and overcast (stippled) cloud ceilings below 5,000 ft. with surface relative humidity isopleths (percent), 2000 GMT, May 19, 1960.

cover itself by holding down temperatures during the afternoon, thus preventing the afternoon decrease of relative humidity that accompanies heating with a constant specific humidity. In addition, of course, clouds associated with a front may precipitate, in which case there should be a very good correlation between cloud and humidity.

Some practical use might be made of this relationship, at least over convective areas, because it appears that the agreement or disagreement of surface humidity with low cloud ceilings depends largely on vertical mixing. This mixing, in turn, is a function of the stability; i.e., where stability is strong surface heating can produce only few clouds, and where the stability is weak the heating quickly produces a cloud ceiling. Therefore, where high surface humidities can be inferred independently, lack of a cloud ceiling implies great stability, and a low cloud ceiling indicates instability. Even qualitative information of this type over data-free regions would be valuable.

Figure 3c shows the surface humidity patterns superimposed on the low cloud nephanalysis for 2000 GMT, May 19. On this and subsequent figures, isopleths of

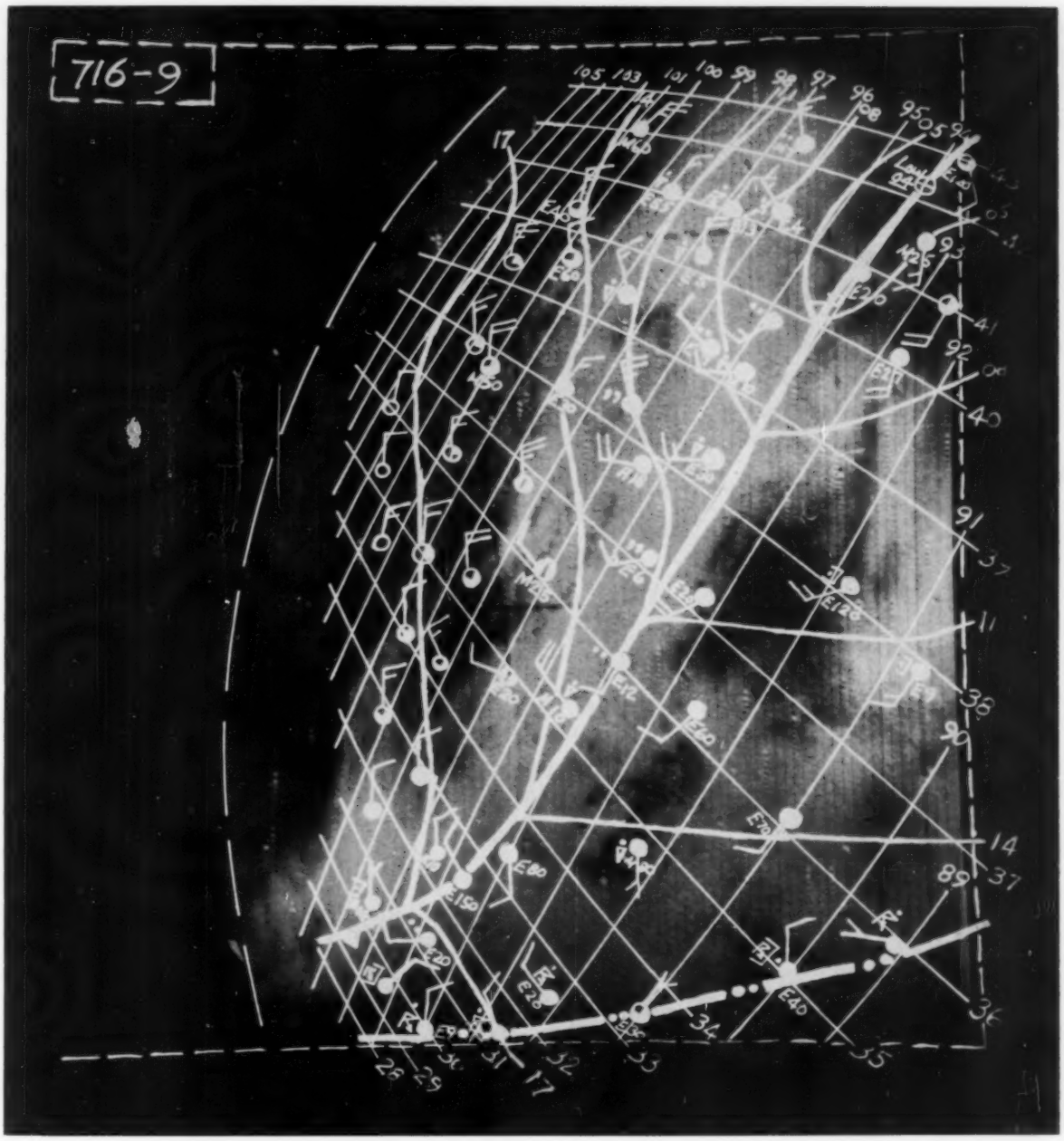

FIGURE 4.—TIROS picture for 1908 GMT, May 20, 1960 with data and latitude-longitude grids superimposed.

relative humidity were drawn to station data and therefore do not display the detail of the low cloud nephanalyses which were made from station reports and cloud pictures.

Allowing for these differences, it is seen that in almost all of the areas where low cloud ceilings existed, the surface humidity was greater than 70 percent. Only Belleville, Ill., Dayton, Ohio, McAlester, Okla., and St. Louis, Mo. failed to report low cloud ceilings. Where the humidity was below 50 percent, almost no low ceilings were reported. Only Waco, Tex., Cheyenne, Sheridan, and Yellowstone Park, Wyo. reported low ceilings in this case.

Examination of the vertical temperature distribution between 1 and 2 km. at 0000 GMT, May 20, for the exceptions showed that the lapse rates were quite small (stable conditions) over the four stations where the humidity was greater than 70 percent and no low cloud ceilings existed. Conversely, the lapse rates over the four stations where low ceilings existed over low surface humidity

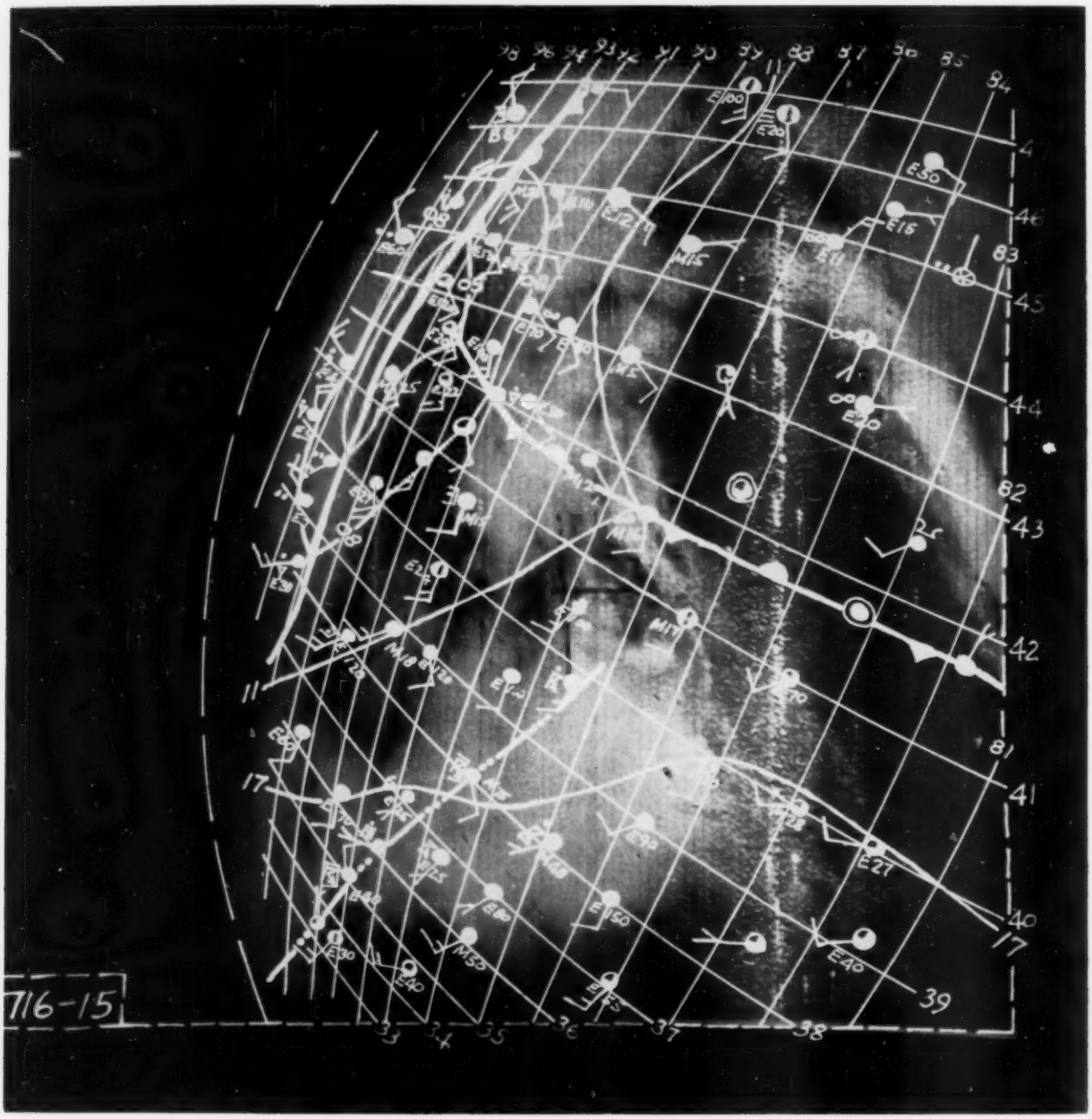

FIGURE 5.—TIROS picture for 1910 GMT, May 20, 1960 with data and latitude-longitude grids superimposed.

were quite large (unstable conditions)—a curious relationship noted on the other days as well, but a relationship that is not of direct utility in the context just mentioned.

3. CLOUD DISTRIBUTIONS AND ANALYSES, MAY 20, 1960

Figures 4 and 5 show the cloud patterns about the Low and frontal systems at 1908 and 1910 GMT, while figures 6 and 7 show the area to the north at 2053 and 2054 GMT. The cloud schematic diagrams of these pictures were combined and are shown in figure 8a. Figure 8b gives the corresponding surface analyses with the 500-mb. trough superimposed.

SYNOPTIC SITUATION

By 1900 GMT, May 20, the surface Low in Manitoba, Canada had filled and a new low center had developed in Iowa along the cold frontal trough. This development marked the first strong cyclonic circulation of the low

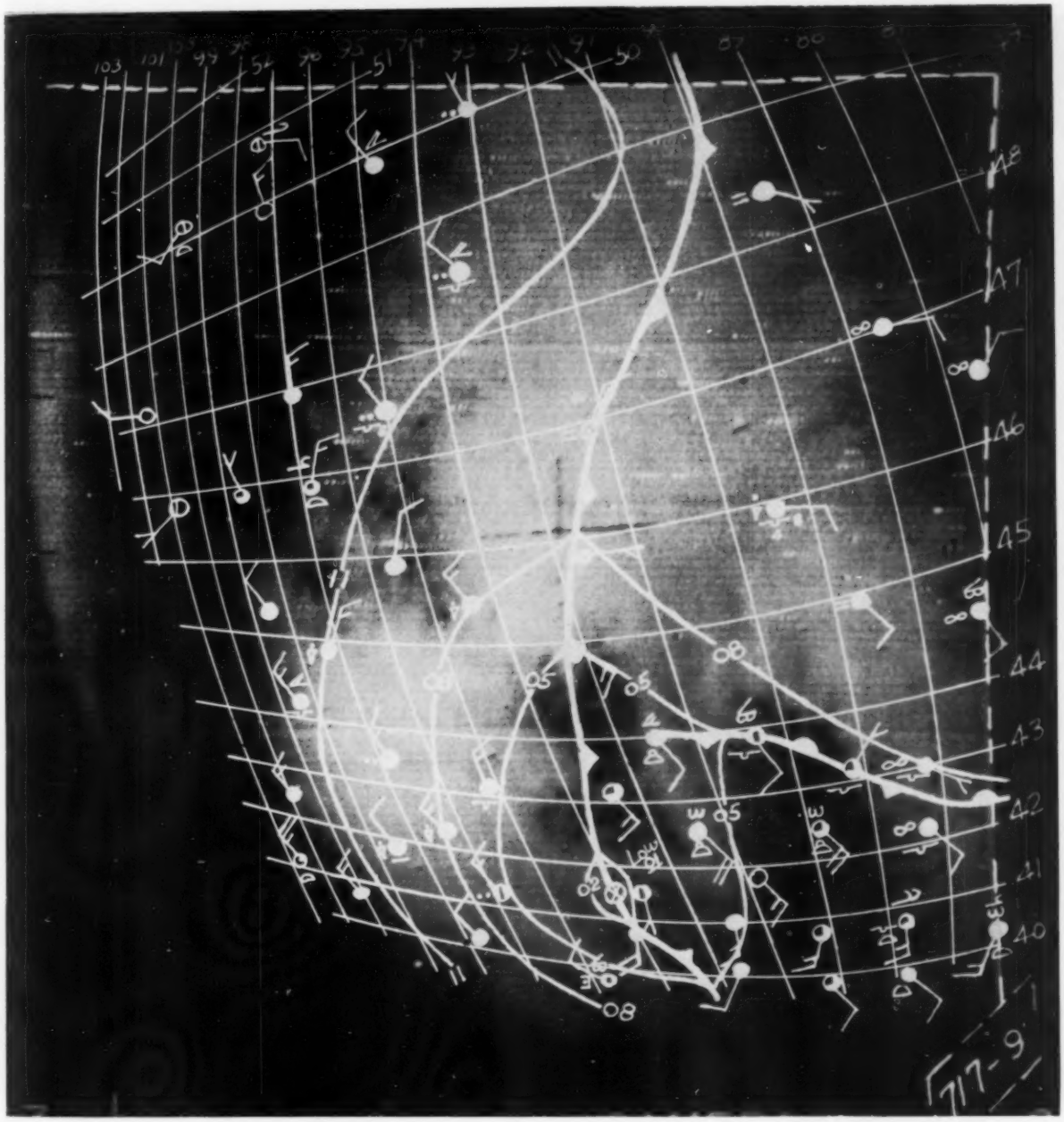

FIGURE 6.—TIROS picture for 2053 GMT, May 20, 1960 with data and latitude-longitude grids superimposed.

system. Both the warm and cold frontal systems in Iowa remained stationary, while the southern portion of the cold front and the eastern portion of the warm front moved slowly eastward and northeastward, respectively.

A very active squall line had developed and extended all the way from Indianapolis, Ind. to Galveston, Tex. The low-level southwesterly winds which extended northward through central Texas during the development of the squall line on the night of May 19 (between 0000 and 0300 GMT, May 20) and the presence of a zone of low-level stability (small lapse rates) offer strong support to the theories of Rossby [4] and Cahn [5] and the work of Tepper [6] in which he speculates that "The development of eastward propagating pressure-jump lines (associated with squall lines) was due to the addition of momentum to the low level southerly flow by a marked increase in the southerly component of winds during the night."

The cloud field had become organized into a broad

613342—61——3

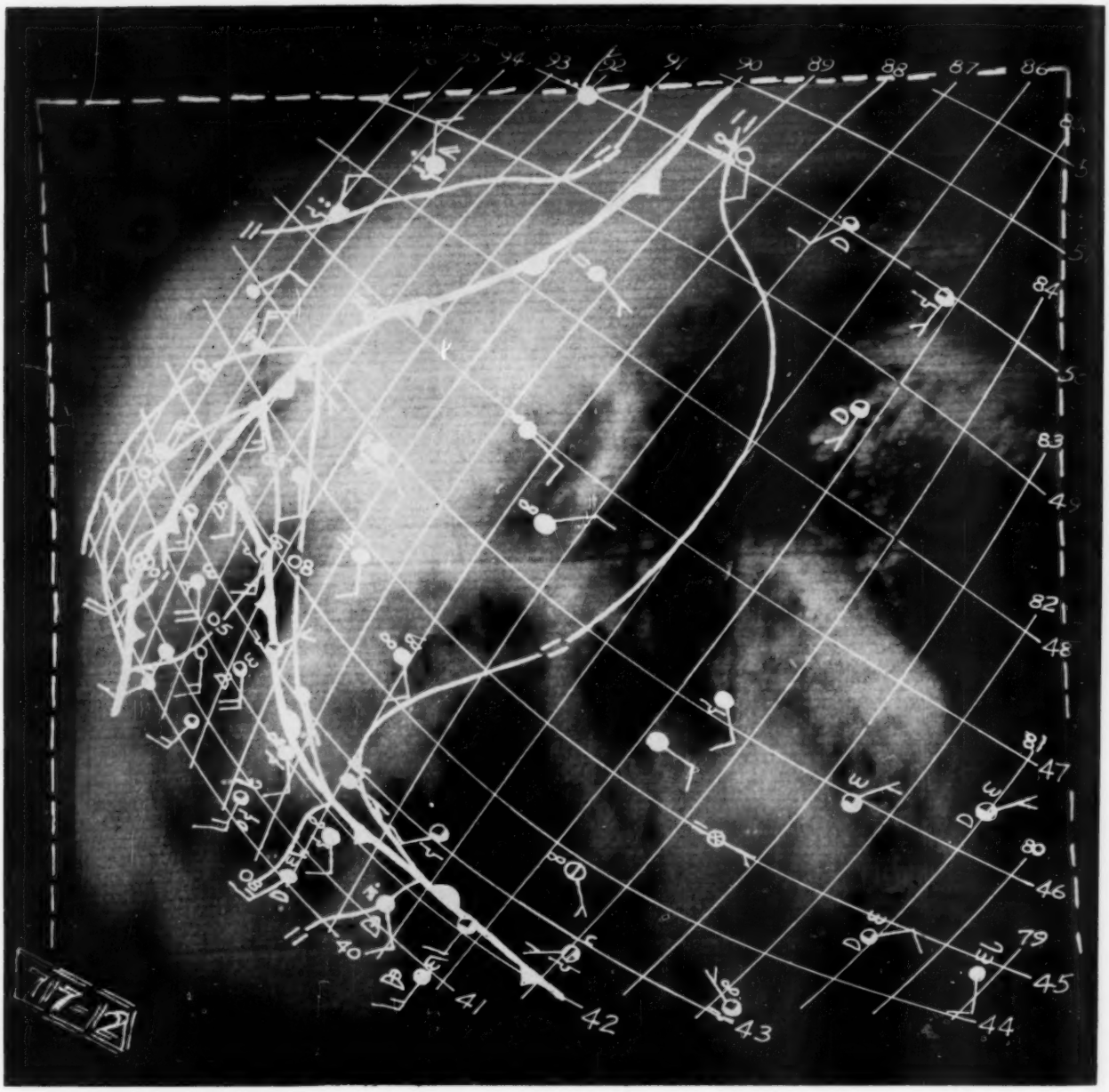

FIGURE 7.—TIROS picture for 2054 GMT, May 20, 1960 with data and latitude-longitude grids superimposed.

north-south band (fig. 8a). The cloud distribution which lay well behind the surface cold front on the previous day had now assumed a position over the front and the squall line in a pattern following the "ideal" cold frontal model. Middle and high clouds still remained at and ahead of the 500-mb. trough; but by the steepening of the surface to 500-mb. trough slope from 1/180 to 1/50, middle and higher clouds were brought over the low cloud deck thus forming the broad north-south band with rapid clearing to the rear.

The breaks in the overcast band (fig. 8a) indicate the separation between that portion of the cloud band associated with the cold front and that associated with the squall line. These small clearing areas between 92° and 93° W. and the weakening of the cloud band at about 35° N. are best viewed on figure 4. It was in this region, at this time, that the clear tongue photographed on the next day (May 21) was beginning to form.

On figures 5 and 7 note that the cloud field ahead of the warm front (now stationary) had become less extensive,

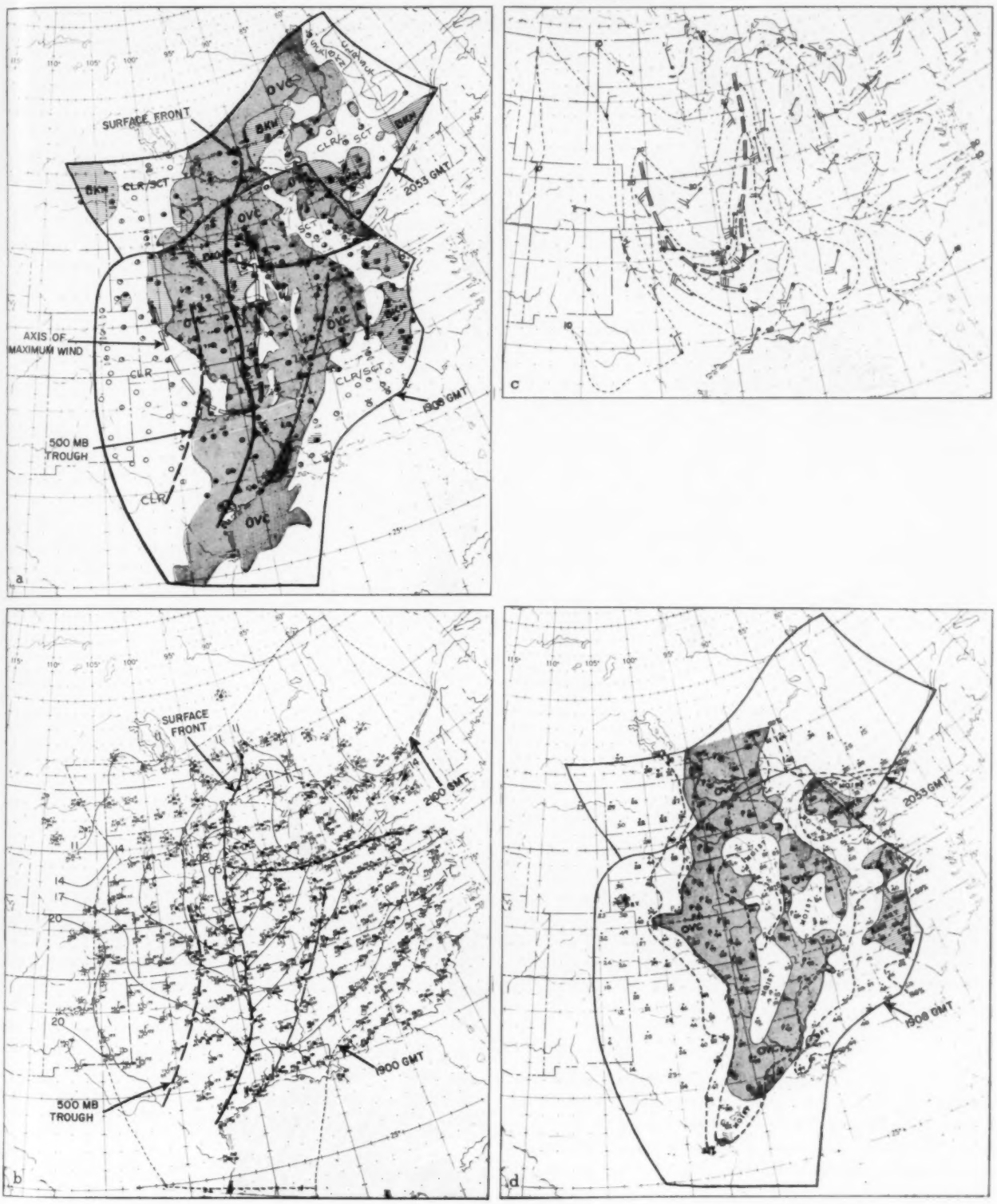

FIGURE 8.—(a) Schematic nephanalysis 1908–1910 and 2053–2054 GMT, May 20, 1960. Broken line shows axis of maximum wind at 5,000 ft. (from map c). (b) Surface data and analyses 1900 and 2100 GMT, May 20, 1960. (c) Wind data, axis of maximum wind, and isotachs (kt.) at 5,000 ft., 1800 GMT, May 20, 1960. (d) Broken and overcast cloud ceilings below 5,000 ft. with surface relative humidity isopleths (percent) 1900 and 2100 GMT, May 20, 1960.

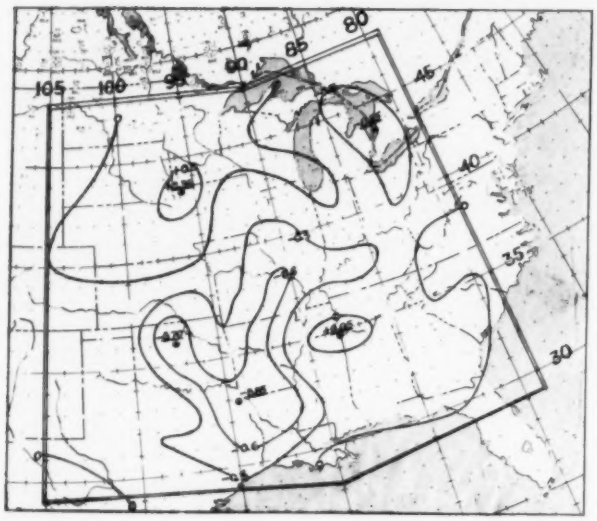

FIGURE 9.—850-mb. horizontal moisture advection (gm. kg.$^{-1}$ hr.$^{-1}$), 0000 GMT, May 21, 1960.

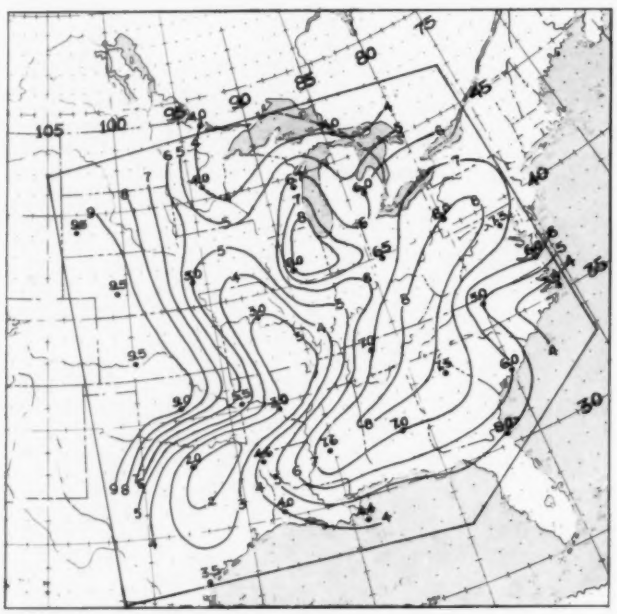

FIGURE 10.—Lapse rates between 1 and 2 km. (°C. km.$^{-1}$), 0000 GMT, May 21, 1960.

less dense, and somewhat disorganized from that seen on the previous day. The zone of scattered clouds extending across and ahead of the front in the vicinity of 85° W. is believed to have been caused by horizontal advection of dry air and is discussed below.

LOW-LEVEL WIND MAXIMUM

Figure 8c shows the wind analysis at 1800 GMT, May 20, 1960 for the 5,000-ft. level; the axis is also shown on figure 8a. The clearing in the region of the maximum wind and its long narrow shape suggest it may have been produced by the advection of dry air in the low-level jet.

To examine this possibility, the horizontal advection of moisture was computed for 0000 GMT, May 21, and is shown in figure 9. This computation revealed that the strongest advection was taking place south of the wind maximum. The advection of dry air across the stationary front near 85° W. was primarily the result of a large moisture gradient while the advection to the south of the jet maximum was caused by a large moisture gradient as well as high wind speeds. Because these large moisture gradients existed within the same air mass, it appears that vertical motions were creating extensive pockets of dry air, a matter that is investigated next.

VERTICAL MOTIONS

The 600-mb. JNWP vertical motions, interpolated for picture time, showed upward motions between 0 and 1 cm. sec.$^{-1}$ over the eastern half of the United States with a very small zone of upward motion greater than 1 cm. sec.$^{-1}$ centered near Jackson, Miss. The zero isopleth closely delineated the trailing edge of the broad north-south cloud band to the rear of the cold front. The clearing associated with the low-level wind maximum, the zone of scattered clouds across the stationary front in the vicinity of 85° W., and the region of clear to scattered clouds ahead of the squall line (see fig. 8a) were all located in the region of computed large-scale upward motion.

SURFACE RELATIVE HUMIDITY

Figure 8d shows the 1900 and 2100 GMT surface humidity patterns superimposed on the corresponding low cloud nephanalysis for May 20, 1960. The 70 percent humidity isopleth again showed a tendency to outline the regions of low cloud ceilings while there was generally an absence of low cloud cover where the humidity was below 50 percent.

Of the 215 stations shown, 41 stations violated the stipulated 50 percent and 70 percent limitations: 8 stations, located in areas labeled "DRY" showed broken low cloud ceilings with surface humidities less than 50 percent; 33 stations, located in areas labeled "MOIST", had humidities greater than 70 percent but no low cloud ceilings.

Examination of the lapse rates about the 850-mb. level approximately 5 hours after picture time indicated that the violations were again related to the low-level stability. In figure 10, which shows the lapse rates between 1 and 2 km. for 0000 GMT, May 21, it is seen that the lapse rates over the areas corresponding to the regions labeled "MOIST" were quite stable; while over the regions labeled "DRY" the lapse rates were quite unstable.

4. CLOUD DISTRIBUTIONS AND ANALYSES, MAY 21, 1960

Figures 11 and 12 show the spiral cloud band about the cold front and the clear tongue to the rear at 1816 and 1817 GMT. Figures 13 and 14 show the northern por-

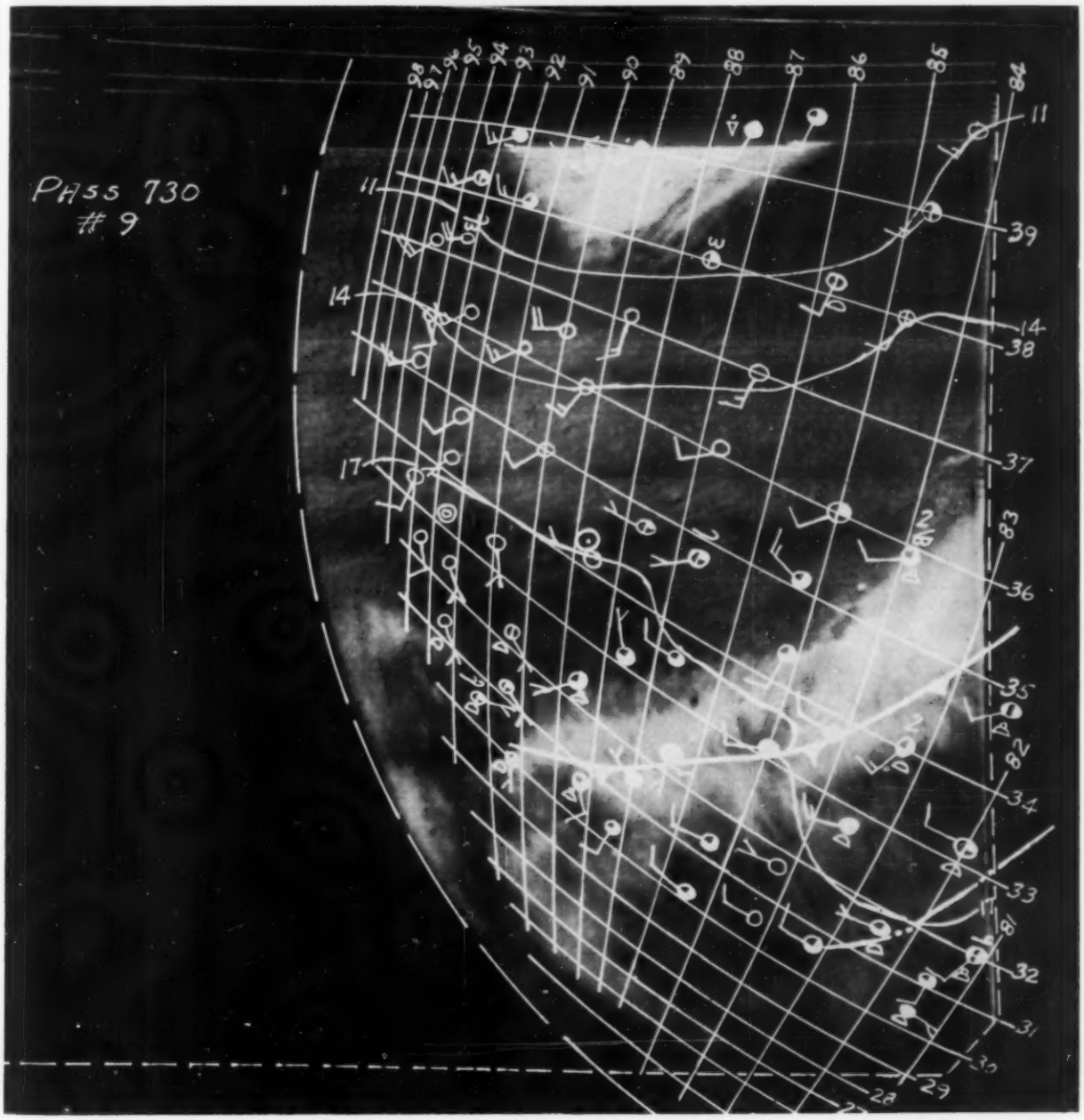

FIGURE 11.—TIROS picture for 1816 GMT, May 21, 1960 with data and latitude-longitude grids superimposed.

tion of the clear tongue and the spiral band associated with the vortex at 2000 and 2001 GMT. The combined schematic nephanalysis for these photos is shown in figure 15a. Figure 15b gives the corresponding surface analyses. The 500-mb. trough is not shown because there was uniform curvature about the closed system with no pronounced trough.

SYNOPTIC SITUATION

By 1800 GMT, May 21, the surface low center had moved 180 mi. northeastward while the upper-air Low had deepened, become closed, and moved approximately 300 mi. to the northeast; this movement made the axis of the low system very nearly vertical. During the previous 23 hours, the winds in the low levels had under-

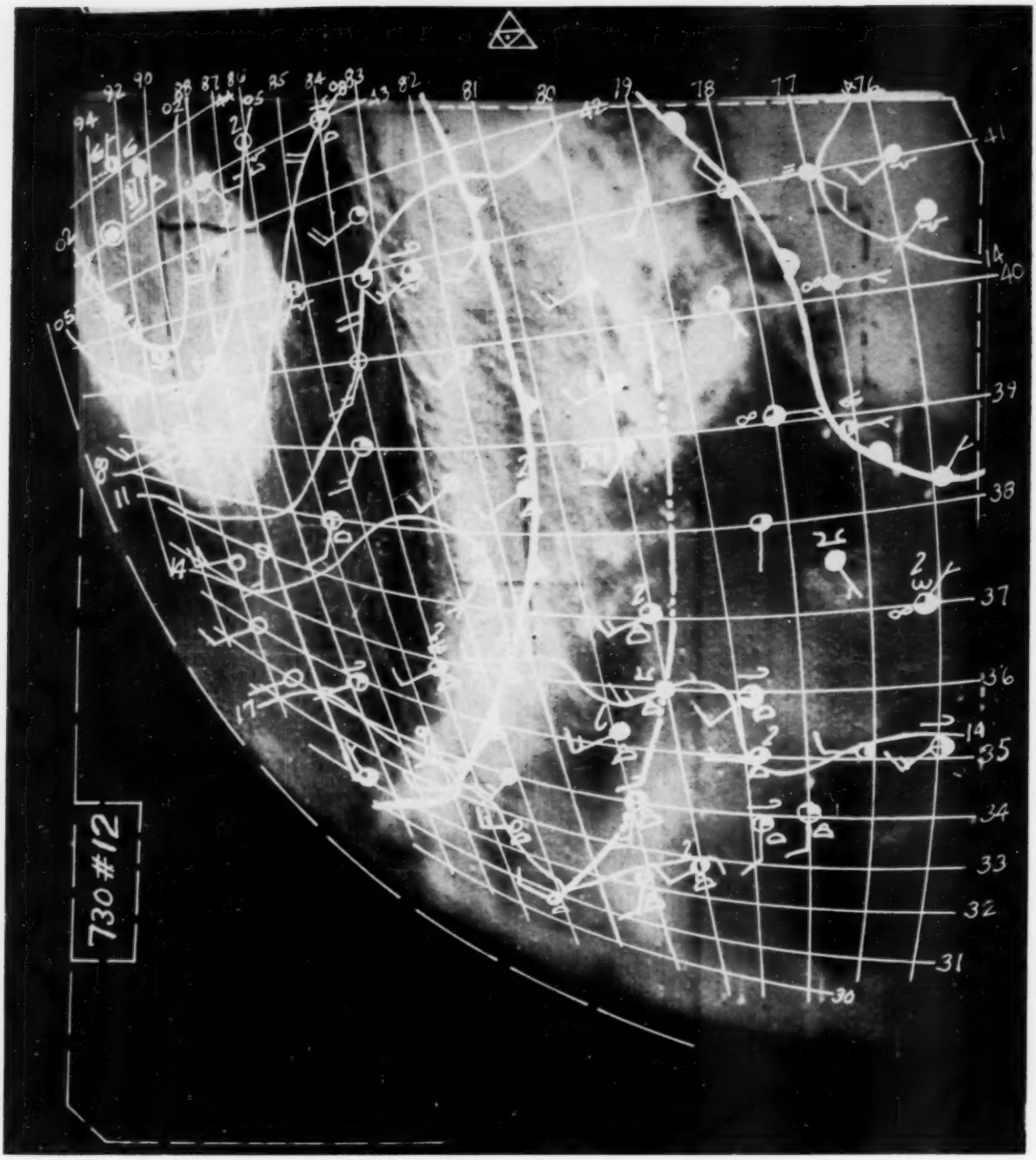

FIGURE 12.—TIROS picture for 1817 GMT, May 21, 1960 with data and latitude-longitude grids superimposed.

gone a 10-kt. increase and the rapid movement of the cold front produced a long bent-back occlusion over the Great Lakes. The cold front, especially south of 35° N., was undergoing frontolysis and had become shallow and diffuse.

A large change in the cloud distribution had taken place from that shown in figure 8a for the previous day. The cloud field associated with the cold front had become a very narrow band lying over the upslope side of the Appalachians and an expansive clear area with a long

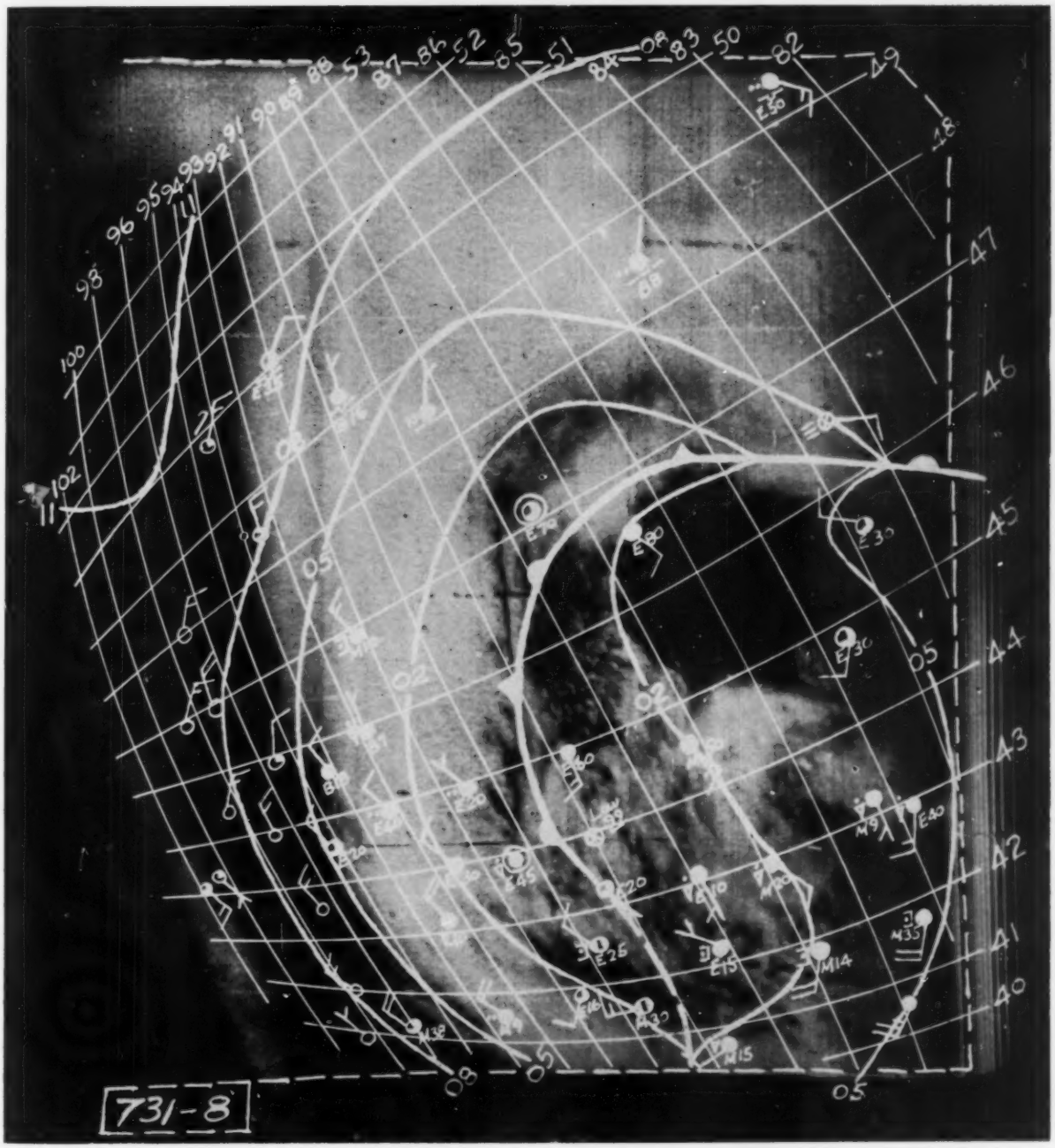

FIGURE 13.—TIROS picture for 2000 GMT, May 21, 1960 with data and latitude-longitude grids superimposed.

narrow curved clear tongue had developed behind the front. The broken section of clouds about 200 mi. east of the cold front partly reflected the weak instability line.

Cloud patterns on this day complied very nicely with the "ideal" distribution model.

LOW-LEVEL WIND MAXIMUM

Figure 15c shows the wind analysis at 1800 GMT, May 21, 1960 for the 5,000-ft. level. Figure 15a shows the nephanalysis with the axis superimposed. Notice that the axis coincided very closely with the sharp edge of the

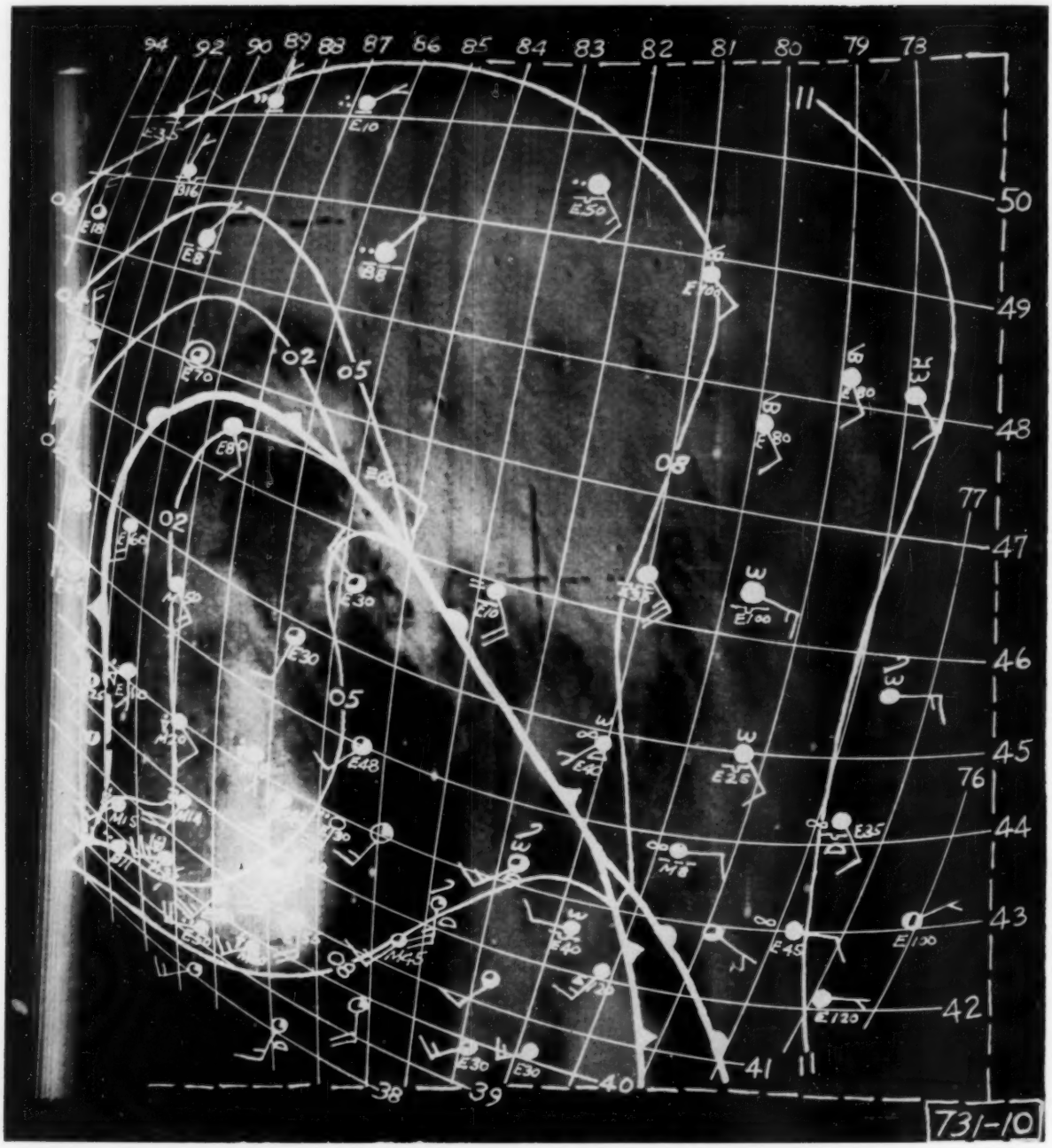

FIGURE 14.—TIROS picture for 2001 GMT, May 21, 1960 with data and latitude-longitude grids superimposed.

low cloud mass which was associated with the vortex to the north.

Examination of the vertical distribution of winds in this area showed that the jet stream at 35,000 ft. was positioned very nearly vertically above the maximum at 5,000 ft., while the intermediate axes about the 14,000-ft. level were located approximately 100 mi. toward the south.

The horizontal moisture advection computed for 1200 GMT, May 21 is shown in figure 16. Again, the strongest advection of dry air was occurring to the south of the maximum axis.

VERTICAL MOTIONS

The 600-mb. JNWP vertical motions showed broadscale downward motion over the Plains States west of the Mississippi Valley and a broad zone of upward motions en-

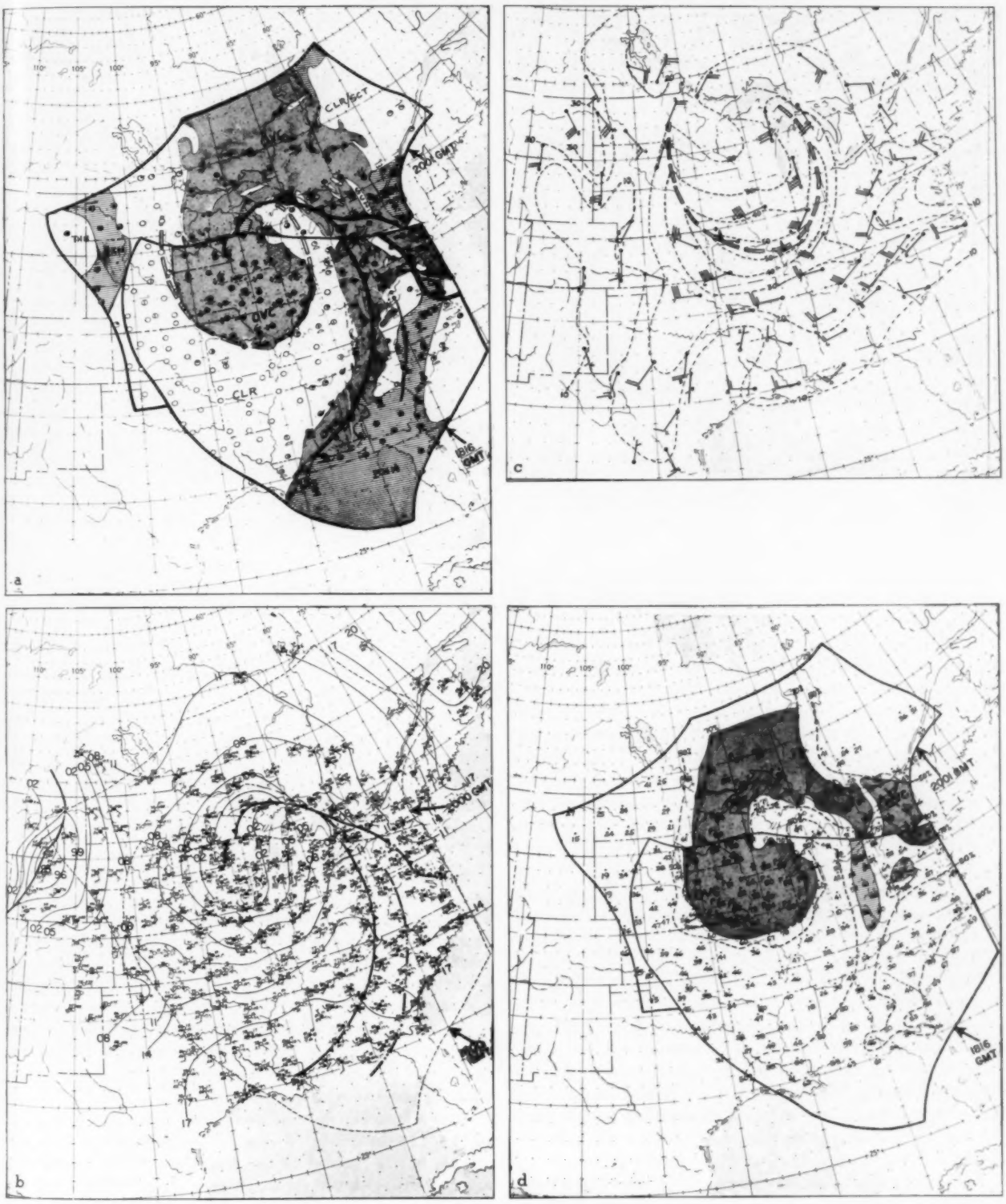

FIGURE 15.—(a) Schematic nephanalysis 1816–1817 and 2000–2001 GMT, May 21, 1960. Broken line shows axis of maximum wind at 5,000 ft. (from c). (b) Surface data and analyses 1800 and 2000 GMT, May 21, 1960. (c) Wind data, axis of maximum wind, and isotachs (kt.) at 5,000 ft., 1800 GMT, May 21, 1960. (d) Broken and overcast cloud ceilings below 5,000 ft. with surface relative humidity isopleths (percent), 1800 and 2000 GMT, May 21, 1960.

613342—61——4

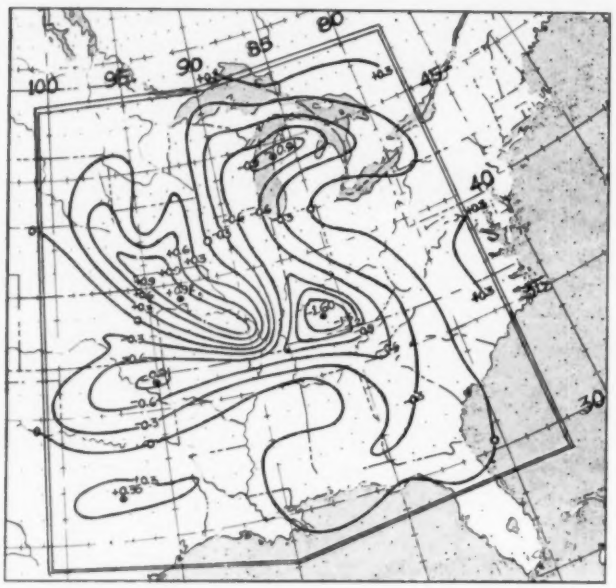

FIGURE 16.—850-mb. horizontal moisture advection (gm. kg.$^{-1}$ hr.$^{-1}$), 1200 GMT, May 21, 1960.

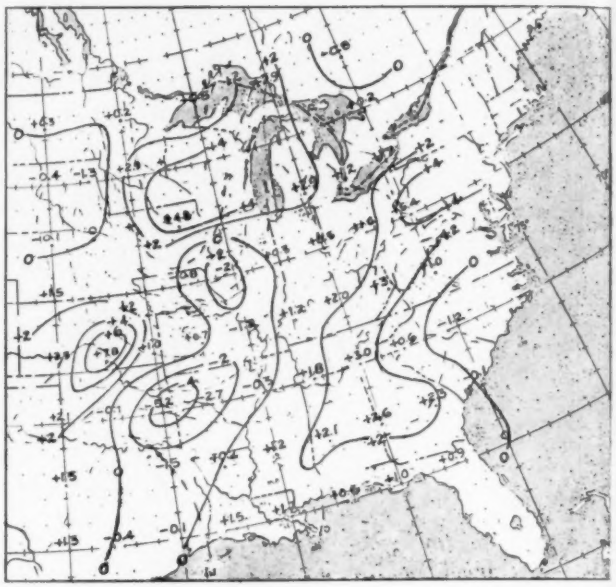

FIGURE 17.—850-mb. vertical motions (cm. sec. $^{-1}$) computed by the adiabatic method, 0000–1200 GMT, May 21, 1960.

gulfing the clear tongue and a portion of the large clear area to the rear of the cold front.

Careful nephanalyses of several sets of surface observations indicated that the strongest development of the clear tongue occurred between 1800 GMT, May 20 and 1200 GMT, May 21. For that reason, the mean vertical motions for the period 0000 to 1200 GMT, May 21 were computed by the adiabatic method [7] for the 850-mb. and 700-mb. levels. Figure 17 shows the vertical motions at 850 mb.

Areas near the Great Lakes were covered with clouds so that the computed vertical motions were based on moist adiabatic processes. At the grid points on figure 17 showing no values, the actual lapse rates were approximately equal to the moist adiabatic lapse rates and hence these computations failed because the stability approached zero. While it is not entirely satisfactory to use the adiabatic method at the 850-mb. level because of the influence of surface radiation, it is very likely that the downward motion yielded by this computation was correct in sign. This follows because the diabatic cooling of air from 7:00 p.m. to 7:00 a.m. would produce fictitious upward motions in the computation, so that downward motions were shown despite the masking effect of cooling. Upward motions, by the same token, are suspect and the vertical motion over the Appalachian Mountains may be spurious because the diabatic influence was maximized in that region.

Reliability of the computed motions was further attested to by the lapse rates about the 850-mb. level. Comparison of vertical motions at 850 mb. (fig. 17) and the lapse rates between 1 and 2 km. (fig. 10) indicated that the tongue of small lapse rates, about 3°–4° C. km.$^{-1}$, was being produced by the similarly oriented tongue of downward motions.

Vertical motions at the 700-mb. level were similar to those computed at 850 mb., with some slope toward the north of the center at 35° N., 95° W. The secondary center of downward motion at 40° N., 90° W. was overlain with upward motion at 700 mb. In summary, from these computations it appears that subsidence in the low troposphere was concentrated on the anticyclonic shear side of the low-level jet and was producing dry air which was then advected rapidly into the long clear tongue that is shown in the pictures on May 21, 1960.

SURFACE RELATIVE HUMIDITY

Figure 15d shows the surface relative humidity patterns and the low cloud nephanalysis for May 21, 1960. The 70 percent humidity isopleth again closely delineated the areas of low cloud ceilings. Of the 235 stations for which surface humidity was available, not one station reported a low cloud ceiling when the humidity was below 50 percent; only 5 stations violated the prescribed 70 percent limitation by showing no low cloud ceilings with greater than 70 percent relative humidity.

Over these 5 stations, the lapse rates at 0000 GMT, May 22 again indicated that low-level stability was prevailing in the regions of the violations. The increase in area of greater lapse rates (greater than 6°C.km.$^{-1}$) from that of the previous day further suggests that surface humidity is better correlated with low cloud cover when the air is nearly unstable and substantial mixing is occurring.

5. SUMMARY

Over the 3-day period, cloud distribution about the surface fronts conformed nicely with the "ideal" distribution models with the exception of the distribution about the cold front on May 19, 1960. On this day, clouds were found well to the rear of the cold front because the 500-mb. trough, with which the bulk of the clouds was associated, was located approximately 500 mi. to the rear of the surface frontal position. In such north-south cold frontal systems, the amount of cloudiness behind the surface front may be an indicator of the slope of the upper-air system.

The long clear tongue shown in figures 12 and 14 developed in the region of a low-level wind maximum. This striking feature, which appears to be a frequent mark of this type of synoptic situation, was caused by the development of a strong band of subsidence on the anticyclonic shear side of the low-level wind maximum. This strong subsidence at both the 850- and 700-mb. levels, on the anticyclonic shear side of the maximum wind speed intensified the horizontal advection of dry air and hence the clearing far downstream from the isotach maximum.

The 600-mb. JNWP vertical motions computed by the present model reflected some large-scale vertical motion fields. Clouds were sometimes photographed in areas of computed downward motion and often no clouds were found in areas of upward motion. The vertical motions computed by the adiabatic method for the period 0000–1200 GMT, May 21 agreed quite well with the cloudiness observed at 0600 GMT, May 21.

There was a high correlation between surface humidity and low cloud cover. Over the 3-day period, of the 660 stations examined, only 54 violated the 50 percent and 70 percent limitations and each of these 54 violations fell within 120 miles of the prescribed humidity isopleth. In general, the following relationships were seen: (a) low cloud cover was overcast where surface humidity was 80 percent or greater; (b) low cloud ceilings (broken to overcast) were observed where the surface relative humidity was 70 percent or greater; (c) relative humidities of 50 percent to 70 percent were the middle ground where low cloud coverage was both smaller and greater than 5/10; (d) low cloud ceilings were not reported where surface humidity was below 50 percent.

The strong relationship between surface humidity and low cloud cover appears to be characteristic of summer afternoon regimes where strong surface heating produces instability in the low levels and thus allows substantial mixing of the subcloud layer. It was seen that the poorest agreement of the surface humidity and low cloud cover existed over areas of very small lapse rates (stable conditions). On the other hand, when lapse rates were larger (more unstable conditions) there was considerable vertical mixing of a moist layer such that surface humidities were closely related to low cloud cover.

ACKNOWLEDGMENTS

Special acknowledgment is given to: Harold P. Thompson for assistance in obtaining input data for the picture grids; Morris Frankel for the program computation of the grids; Norman Springer for printing the pictures; Carlos Noboa for his assistance in preparing the figures; National Meteorological Center for the use of synoptic charts and data; and Lawrence A. Hughes who reviewed the first draft and offered many helpful suggestions.

REFERENCES

1. H. R. Byers, *General Meteorology*, McGraw-Hill Book Co., Inc., New York, 1944 (see Chap. XIV, p. 317)
2. V. J. and M. B. Oliver, "Forecasting the Weather in Middle Latitudes from the Direction and Change of Direction of the Winds at 10,000 Feet," *Handbook of Meteorology*, McGraw-Hill Book Co., Inc., New York, 1945, (Rules 3 and 5, pp. 814–815).
3. L. F. Whitney, Jr. and S. Fritz, "A Tornado-Producing Cloud Pattern Seen From TIROS 1," *Bulletin of the American Meteorological Society*, vol. 42, No. 9, Sept. 1961, pp. 603–614.
4. C.-G. Rossby, "On the Mutual Adjustment of Pressure and Velocity Distributions in Certain Simple Current Systems," *Journal of Marine Research*, vol. 1, 1938, pp. 239–263.
5. A. Cahn, "An Investigation of the Free Oscillations of a Simple Current System," *Journal of Meteorology*, vol. 2, No. 2, June 1945, pp. 113–119.
6. M. Tepper, "On the Generation of Pressure-Jump Lines by the Impulsive Addition of Momentum to Simple Current Systems," *Journal of Meteorology*, vol. 12, No. 4, Aug. 1955, pp. 287–297.
7. H. Panofsky, "Determination of Vertical Motion from the First Law of Thermodynamics," *Introduction to Dynamic Meteorology*, Pennsylvania State University, University Park, Pa., 1956, Chap. II.

New Weather Bureau Publications

Research Paper No. 43, "The Measurement of Secular Temperature Change in the Eastern United States," J. Murray Mitchell, Jr., U.S. Weather Bureau, Washington, D.C., 1961, 80 pp. For sale by Superintendent of Documents, U.S. Government Printing Office, Washington 25, D.C. Price: 35 cents.

In the selection of stations on the basis of long series of temperature and precipitation observations for the Climatological Benchmark Network program, final selection was to be predicated on the statistical verification of the homogeneity of their records. For the case of mean temperature data the investigation reported on in this paper leads to a new scheme of homogeneity analysis adopted for the Benchmark program. In the paper it is shown under what circumstances this scheme is justified and of what it consists. Application is then made to seasonal-mean temperature series at a number of stations in eastern United States.

Technical Paper No. 40, "Rainfall Frequency Atlas of the United States for Durations from 30 Minutes to 24 Hours and Return Periods from 1 to 100 Years," David M. Hershfield, U.S. Weather Bureau, Washington, D.C., 1961, 115 pp. For sale by Superintendent of Documents, U.S. Government Printing Office, Washington 25, D.C. Price $1.75.

A summary of empirical relationships, working guides, and maps useful in practical problems involving rainfall frequency data. Part I consists of a description of the rainfall analyses, and Part II contains 49 rainfall frequency maps covering the contiguous United States.

ANOTHER VIEW FROM TIROS I OF A SEVERE WEATHER SITUATION MAY 16, 1960[1]

LINWOOD F. WHITNEY, JR.

U.S. Weather Bureau, Washington, D.C.

[Manuscript received April 25, 1961; revised August 25, 1961]

ABSTRACT

On May 16, 1960, TIROS I televised a series of pictures over the central United States during a severe local storm situation. Comparisons are made between the location of the isolated, bright cloud elements seen in those pictures and (1) the location of surface weather and synoptic features, (2) the location of sferics observations, and (3) the location of the upper-level jet maxima believed important in the development of severe local storm activity. Comparison is made of the cloud cover shown in the pictures to the cover indicated by the surface observations. Apparent brightness and cloud cover of the pictures is discussed in relation to both the weather activity occurring at the surface, and cloud types and cover observed at the surface. Also, cloud streets which appear in the photographs are discussed relative to the observed wind patterns and vertical temperature structure.

Evidence is presented indicating that the severe local storm activity occurred beneath three bright mesoscale cloud masses—the more vigorous activity occurring beneath two masses which were largely isolated from the large-scale patterns. Further, the latter two clouds masses are shown to be correlated well in location with sferics observations and jet stream maxima in the lower levels of the atmosphere

1. INTRODUCTION

Large-scale, bright cloud areas have frequently appeared in the many pictures received from the TIROS meteorological satellites. A limited number of these pictures have shown small-scale very bright cloud patches somewhat isolated from the large-scale patterns. These patches, because of their relative isolation, strong reflectivity, and mesoscale proportions, have suggested intense convective activity, such as a system of well developed thunderstorms perhaps capable of producing a family of severe local storms. In at least one instance to date, such a case has been documented [11].

On May 16, 1960, during pass 659, TIROS I televised a sequence of pictures showing bright, isolated masses of clouds over the central United States during a severe weather situation. A study of that case was undertaken to provide evidence supporting the hypothesis that these distinctive cloud masses were associated with the occurrence of severe weather in the Middle West. In particular, these clouds were investigated relative to synoptic observations, analyses, and sferics. In addition, the photographs were compared with surface cloud observations to aid in identifying the clouds in the pictures. Also, rather prominent wave clouds or cloud streets appearing in the satellite pictures were examined relative to the theoretical models of cloud streets.

[1] This research has been supported by the National Aeronautics and Space Administration.

2. DISCUSSION OF PICTURES

Five wide-angle TIROS I pictures were photographed at approximately 30-second intervals between 205433 GMT and 205831 GMT on May 16, 1960 over the central United States. To facilitate discussion of the pictures, State borders have been superimposed on each of the five pictures (figs. 1–5). Rectification and gridding was done using the procedures discussed in [10].

Two of the three cloud features of interest (A, B, and C) are shown in the figures 2–4. Note that the three major bright areas were located (A) in northern Missouri and southeastern Iowa, (B) over the Illinois and Missouri border, and (C) over Indiana. The cloud mass C, since it is not isolated as are the clouds A and B, does not stand out as clearly. While the western border is well defined, very bright, and easily distinguished, the eastern border blends into the large-scale cover.

The cloud masses described above appeared considerably brighter on the transparencies than in reproduction here. Unfortunately, prints of satellite pictures do not usually differentiate scales of brightness as adequately as do the original 35-mm. transparencies.

Several other prominent and interesting cloud patterns appearing in the pictures are worthy of mention here. For instance, over central Oklahoma and northern Texas (figs. 1 and 2) the clouds are organized in parallel lines or streets. The lines are rather closely spaced and appear comprised of small cloud elements much like cumulus

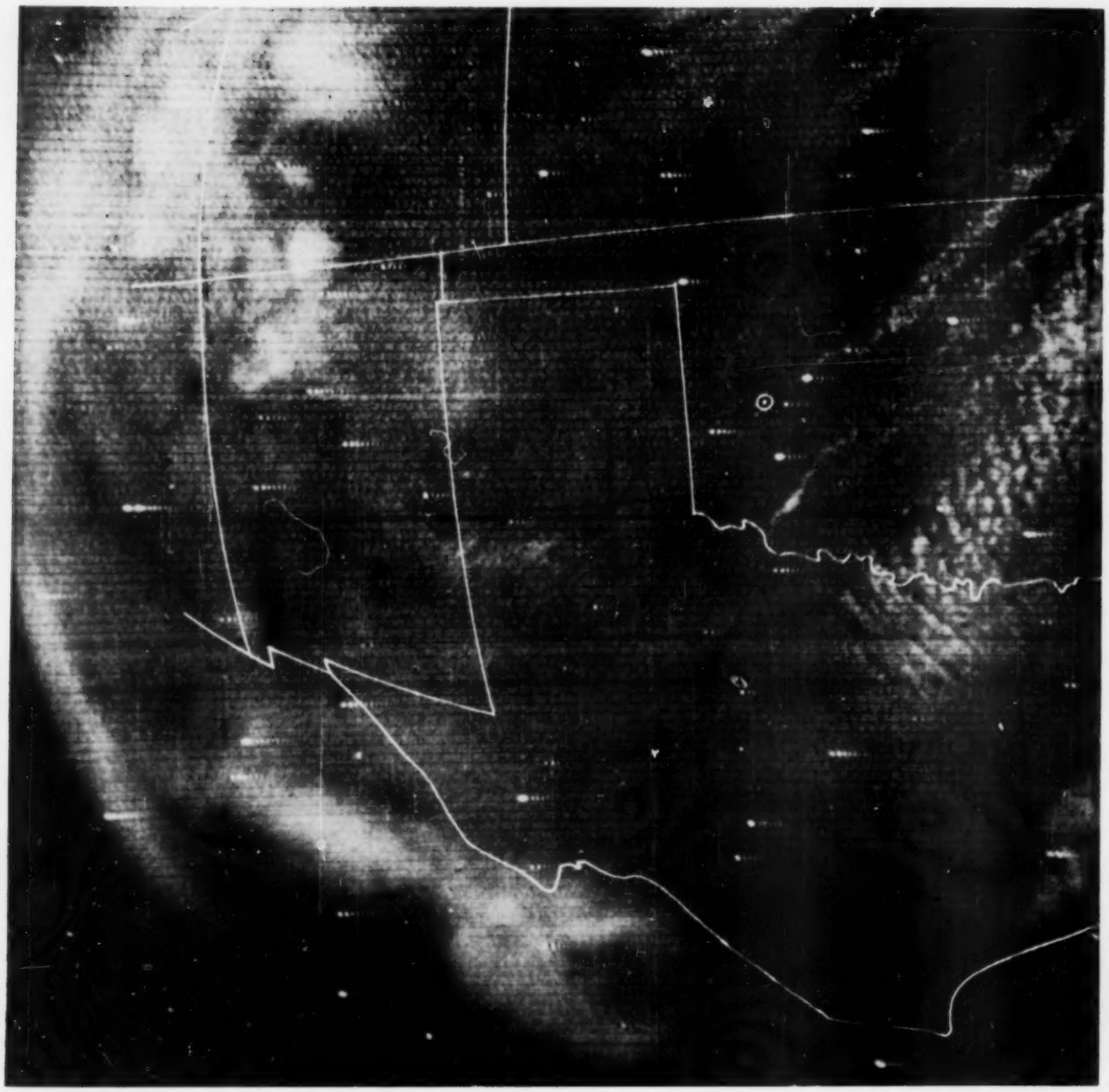

FIGURE 1.—Gridded photograph of frame 4 from the TIROS I pass 659, May 16, 1960, 2100 GMT. Cloud streets are seen at the right in the picture.

cells. Farther to the east, a long, moderately bright cloud band may be seen oriented northeast-southwest through central Arkansas (fig. 2). This band suggests a line of cumuliform clouds.

In figure 3 the moderately bright, extensive cloud cover across the top of the picture was located in the western Lakes area westward into Minnesota and northwestern Iowa. Immediately to the east, over the eastern Great Lakes area (fig. 5), the clouds became filmy and streaked, suggesting that they were cirriform.

Figure 6 is a schematic of the essential features in the five TIROS I photographs. The cloud features are described by the prominence of the boundaries and relative brightness. This presentation, hopefully, will permit the reader to view the features in composite.

3. COMPARISONS OF PICTURES AND METEOROLOGICAL ANALYSES

SURFACE ANALYSIS

The surface chart prepared from the 2100 GMT surface airways observations corresponds to the picture times.

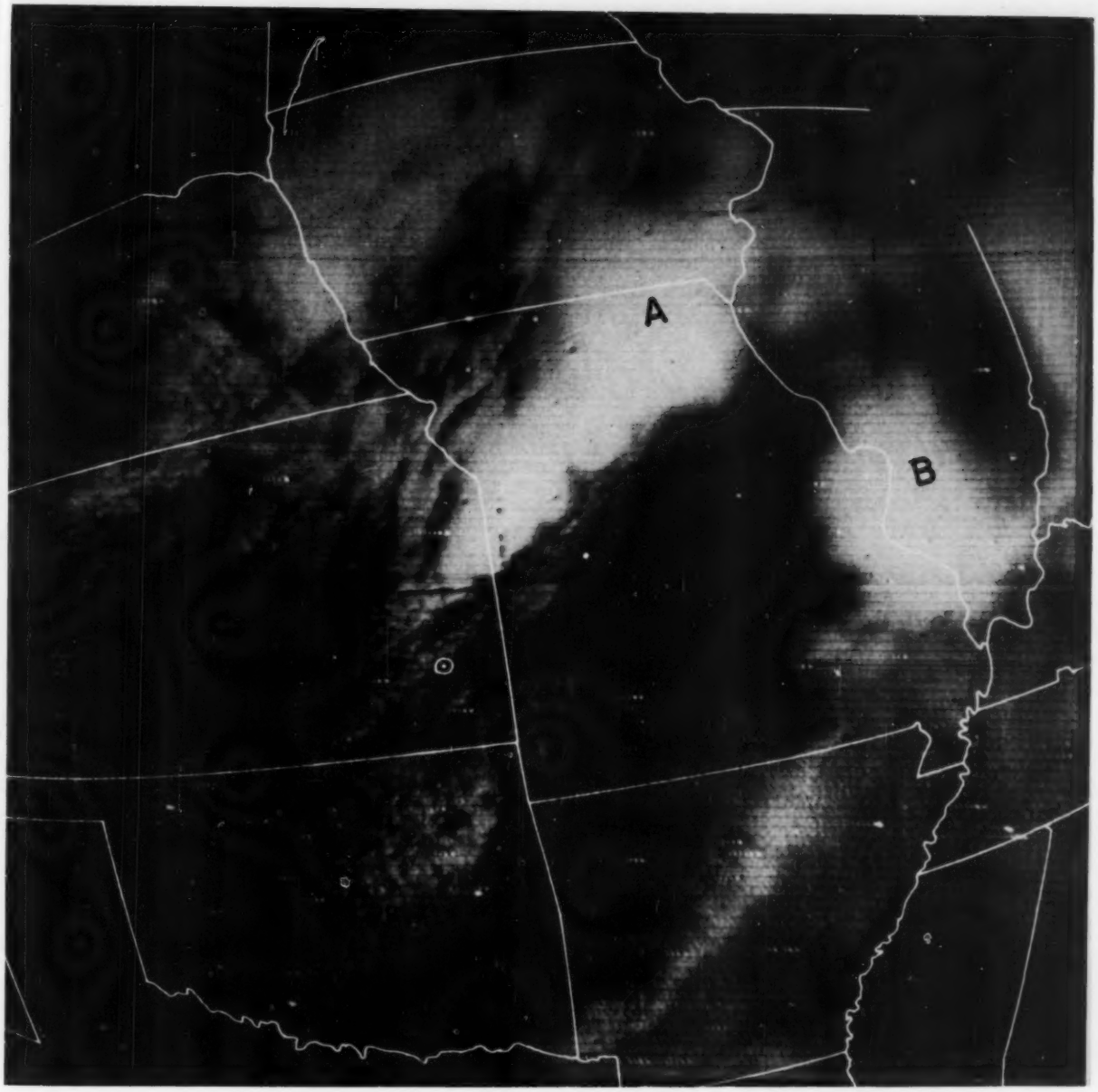

FIGURE 2.—Gridded photograph of frame 7 from the TIROS I pass 659, May 16, 1960, 2100 GMT. Two of three very bright cloud masses associated with severe weather are designated A and B.

A series of hourly charts was prepared to observe short-period changes and to check the continuity of the 2100 GMT analysis. In order that these analyses might be as objective as possible, they were performed independently of the picture rectifications (geographical location of the cloud elements).

In the interest of brevity, only the 2100 GMT surface analysis is shown here (fig. 7). Two small waves appeared on the cold front—one in eastern Kansas and another in western Oklahoma. A warm front extended from the Iowa low pressure center southeastward into West Virginia. Continuous light rain fell to the north of the Iowa low pressure center. A few rain showers were reported in Michigan north of the warm front.

Of primary interest were the thunderstorms and associated severe weather reported in the warm sector. One group of thunderstorms produced some hail along the cold front in northern Missouri; a second group was accompanied by tornadoes and strong winds near the Illinois-Missouri border; and a third group spawned a

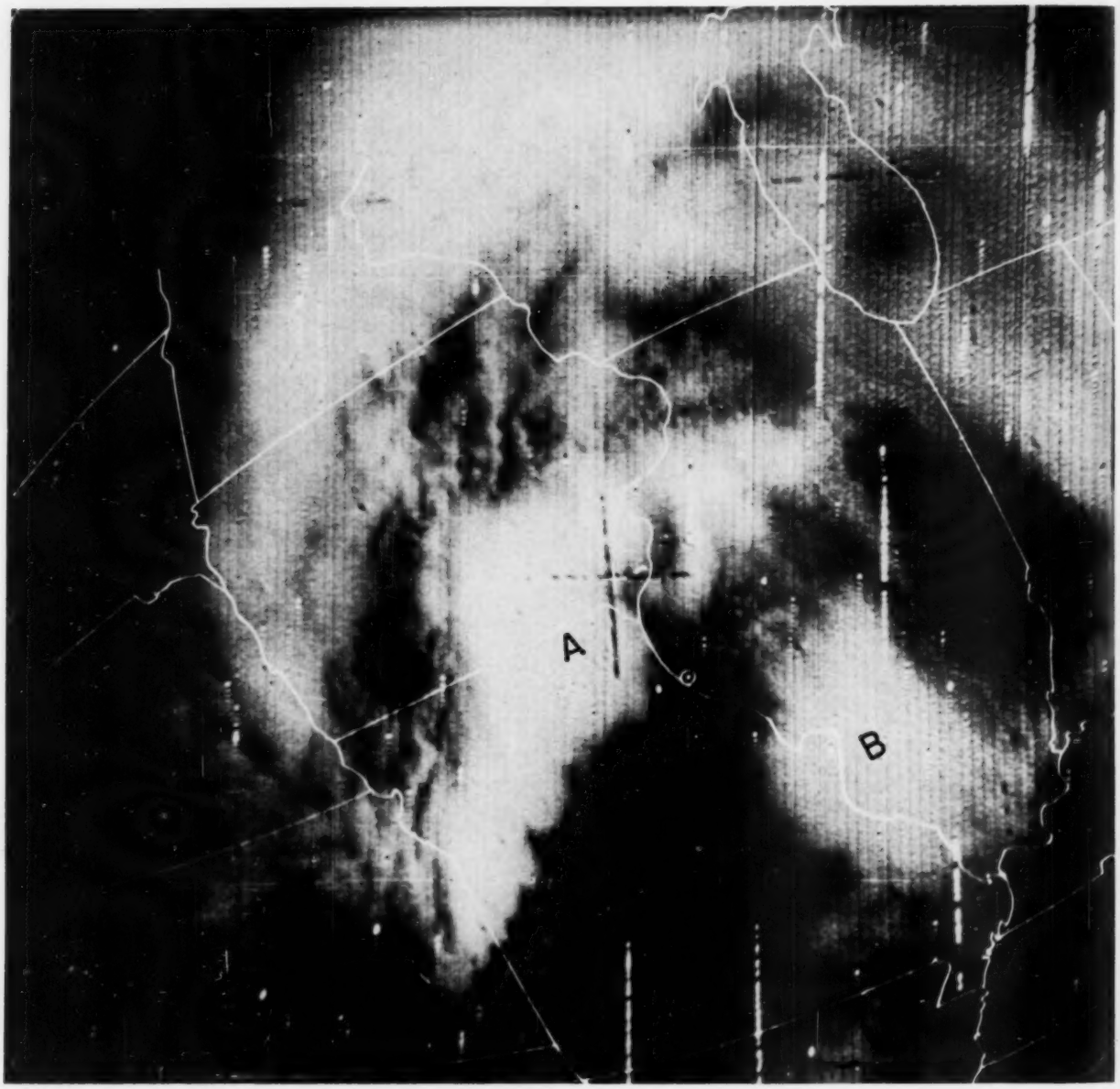

FIGURE 3.—Gridded photograph of frame 11 from the TIROS I pass 659, May 16, 1960, 2100 GMT. The cloud masses A and B are the same two which appear in figure 2. These two masses are somewhat isolated from the large-scale cover to the north.

lone tornado in Indiana. The convective systems are designated A, B, and C, respectively, in figure 7.

Severe weather occurred over a span of 5 hours between 1830 and 2330 GMT (fig. 8) but a good portion of the activity was observed within one hour of 2100 GMT—the time of the TIROS pictures. Though the severe weather during this period was outside the Severe Local Storms Research Network, four mesoscale pressure systems could be detected (fig. 7)—two mesohighs and two mesolows. These systems were analyzed from the airways observations through close examination of the behavior of the wind, pressure, temperature, and weather in time. The analysis of these pressure systems is crude in comparison with that which might be prepared from a dense network of accelerated microbarograph and thermograph traces [5].[2] For the scope of this report there appears to be sufficient evidence that pressure disturbances of the type indicated did exist in the areas shown. In short, the

[2] Dr. Tetsuya Fujita of the University of Chicago has been performing a very detailed mesoanalysis of this situation.

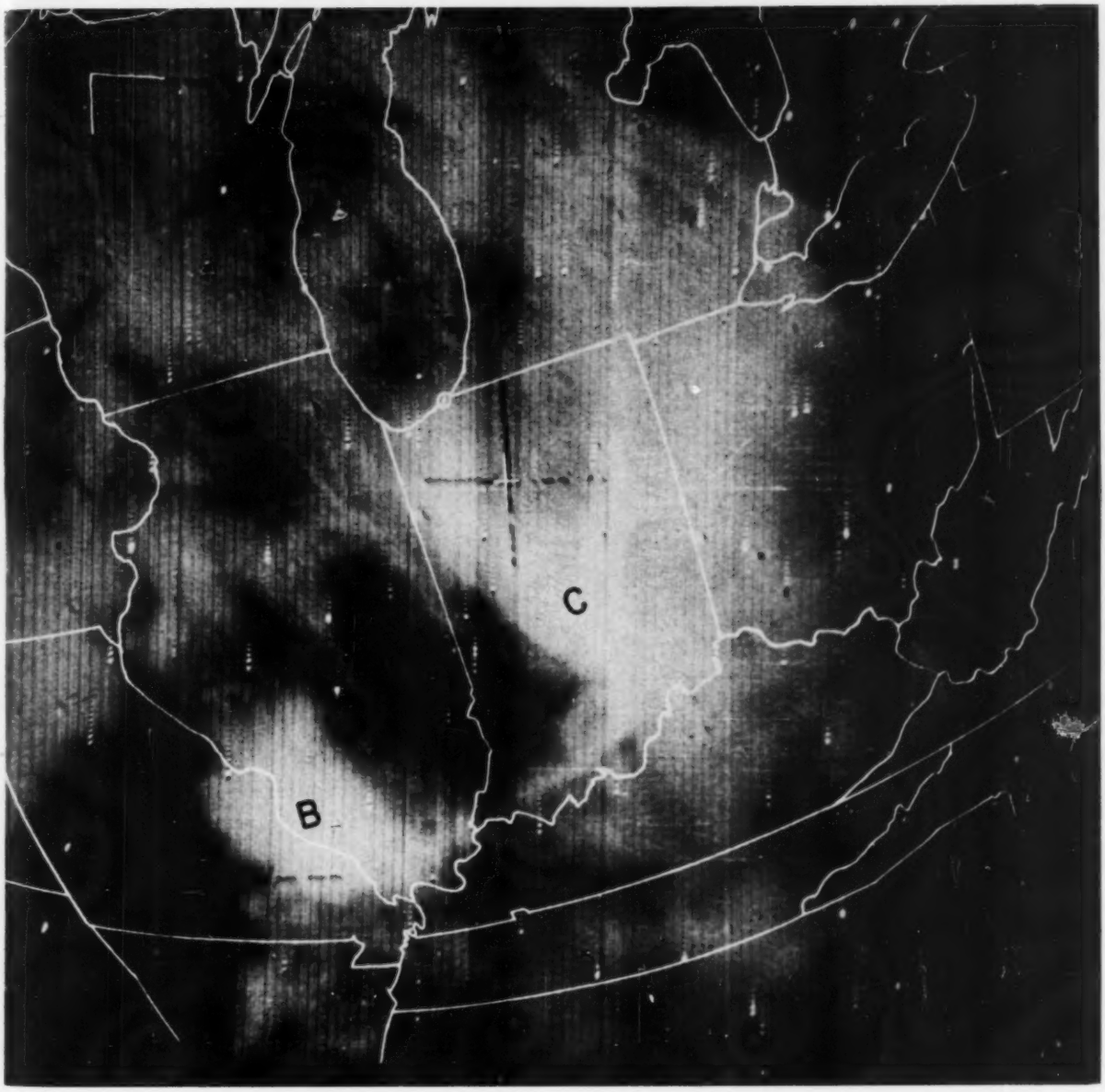

FIGURE 4.—Gridded photograph of frame 15 from the TIROS I pass 659, May 16, 1960, 2100 GMT. The third bright cloud mass appear here as area C. This cloud mass is not isolated from the large-scale cloud cover as are clouds A and B.

severe weather activity in eastern Missouri and that in Indiana were each associated with a mesohigh and the accompanying pressure rise or pressure jump line. It appears that the storms in northern Missouri were associated with the cold front, although one should not rule out the possibility of a mesosystem there. The location of the cold front in Missouri was somewhat nebulous because of the convective activity present.

The convective system C, over Indiana, was less severe at 2100 GMT than were the two disturbances to the west. The only tornado associated with it developed 45 minutes earlier. Its history dated back several hours, having earlier passed through central Illinois and northern Missouri. In all likelihood the system was in a state of decay.

There was no definite indication of unusual weather activity within the two mesolows. Possibly, though, the mesolow in northern Indiana was a tornado-Low or the remnants of the tornado observed in Indiana (figs. 7 and 8).

613342—61——5

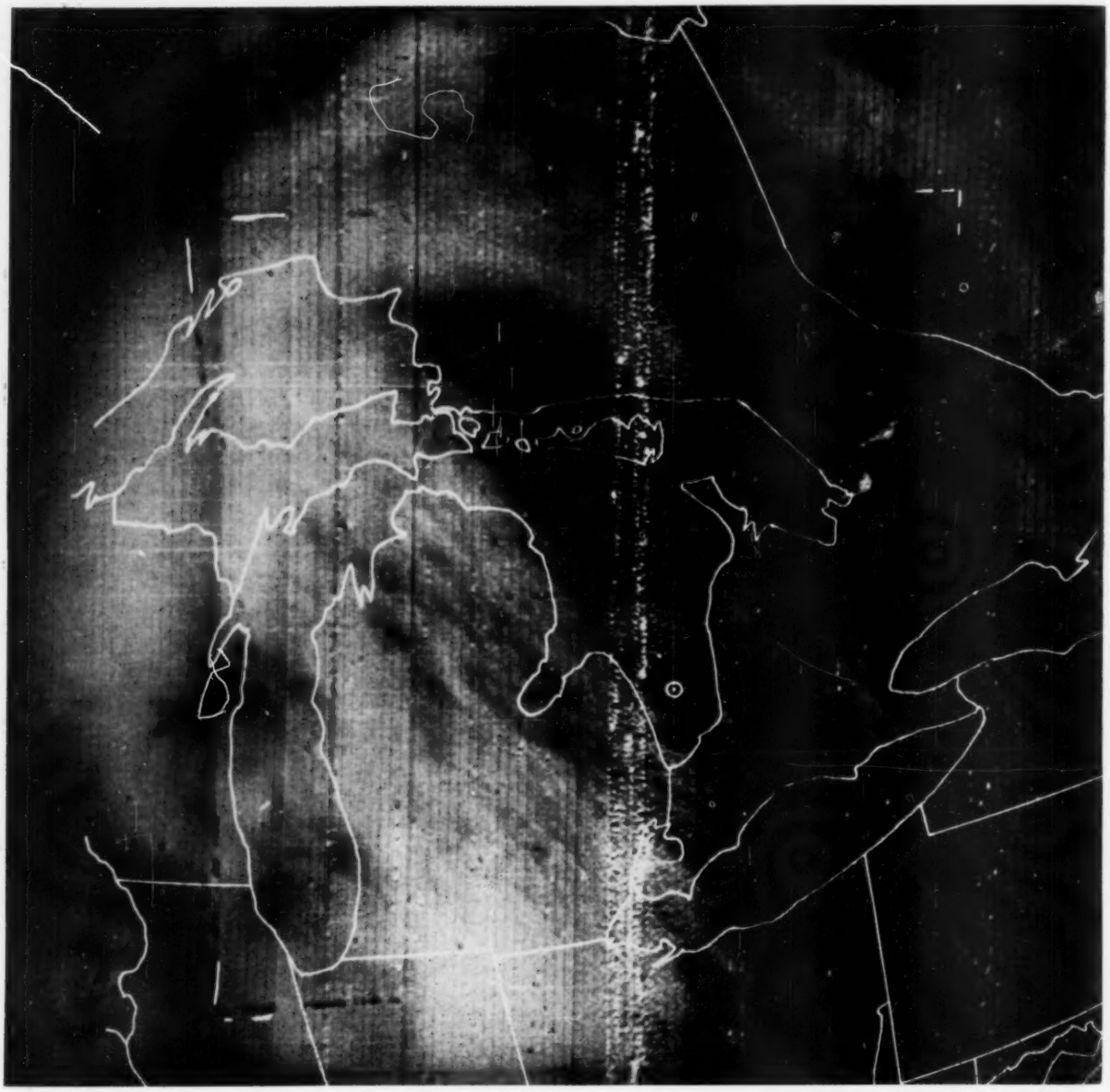

FIGURE 5.—Gridded photograph of frame 19 from the TIROS I pass 659, May 16, 1960, 2100 GMT. A portion of the large-scale cloud cover appears at the left. The filmy and streaked clouds through the center of the picture are associated with cirrus reported in the Great Lakes area.

The severe weather reports within 1 hour of 2100 GMT, and the major surface synoptic features and the surface weather from the 2100 GMT surface chart are shown in composite with the rectified cloud schematic in figure 9 to expedite comparisons. One notes immediately the excellent correlation between the location of the thunderstorm and the severe storm reports relative to two of the three bright cloud masses—one in northern Missouri and southeastern Iowa (area A), and the other in eastern Missouri and southwestern Illinois (area B). The cold front "slices" through the center of the first mass and a squall or pressure jump line through the second.

Geographical agreement between the mesosystem and the third bright cloud mass, C, is not as striking as for the two systems to the west. Thunderstorms were reported both within and without the bright cloud while the squall line, as analyzed, is not aligned with the long dimension of the bright cloud. Lack of agreement may have been influenced by two factors. One, the eastern portion of cloud mass C was very diffuse with the bright-

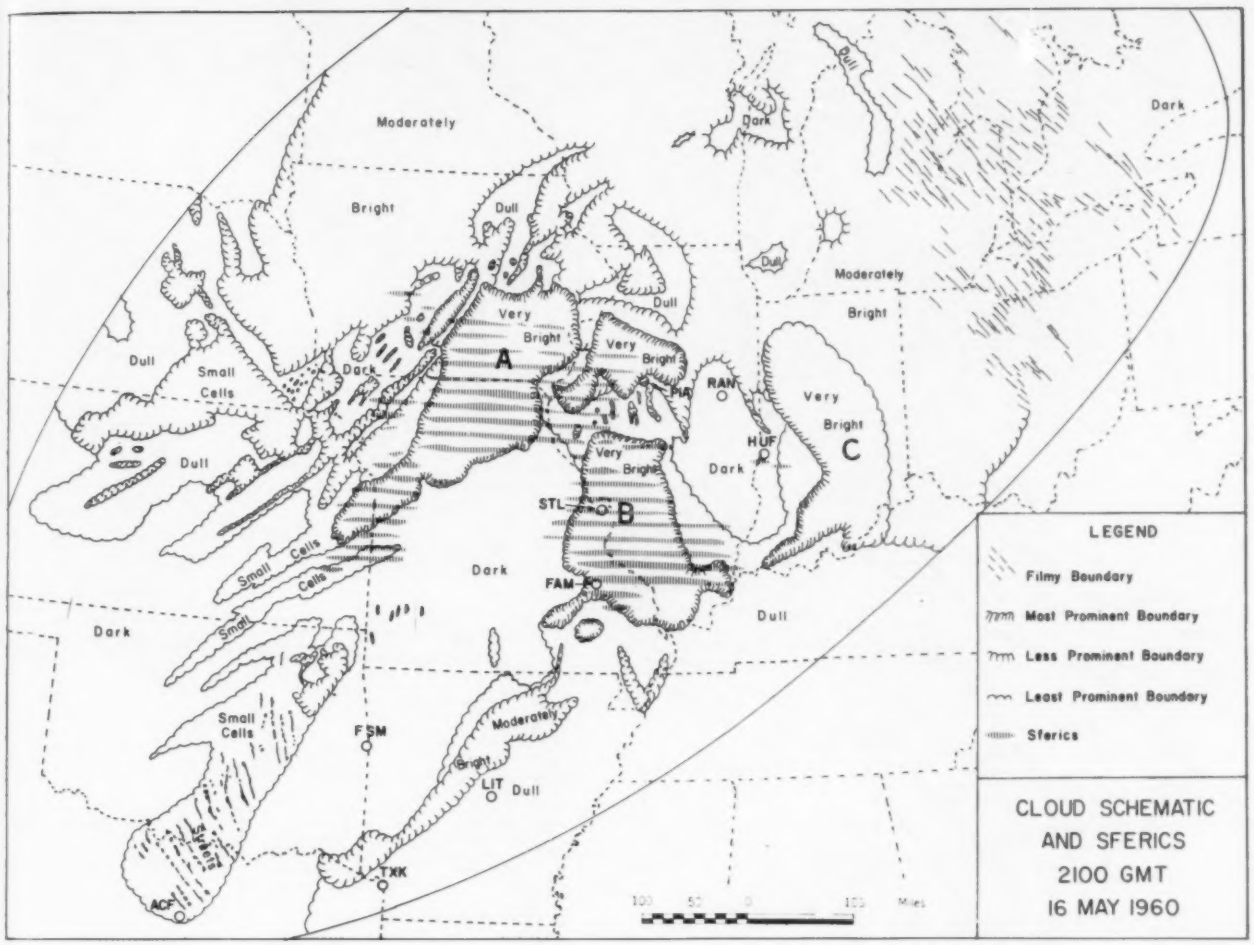

FIGURE 6.—Schematic rectification of the cloud features appearing in figures 1–5. Areas A, B, and C correspond both to those identically lettered cloud masses in figures 2–4 and the severe storm systems in figure 7. All brightness descriptions were determined subjectively from the pictures. Superimposed on the schematic are the 2100 GMT sferics locations taken from figure 10.

ness decreasing toward the east, eventually blending into the large-scale cloud cover (fig. 4) and thus precluding clear delineation of the eastern border. Two, since the disturbance in Indiana was old and decaying, it was not sharply defined.

SFERICS

Figure 10 represents the 50 kc. sferics observations from four station fixes during the interval 2055–2100 GMT, May 16, 1960. Quite obviously there was distinct and frequent sferics return from the area of northern and northwestern Missouri and southeastern Iowa and from the area of east-central Missouri and southwestern Illinois. Comparison of figures 7 and 10 shows these sferics reports correspond extremely well in location with two of the three areas of small-scale convective activity, areas A and B of figure 6, described earlier. In fact, these sferics reports probably outline, in greater detail than the surface observations, those areas where rather vigorous convective activity was taking place.

There was little or no 50 kc. sferics return of consequence at this time in Indiana, area C, even though observations of thunderstorms were made there. Several explanations may be given for this but a plausible one is that the Indiana storms, being less active and decaying, were emitting electrical disturbances in a different frequency range [4] than those to the west and southwest where the systems were vigorous and developing or regenerating, producing severe storms until 2330 GMT.

Since two convective areas (A and B) were shown to have been within the bounds of bright clouds seen from TIROS I, then the sferics observations and bright clouds should be expected to exhibit a measure of correlation. Figure 6, a composite of the sferics return and cloud schematic, reveals a correlation beyond expectation. The bright cloud areas match the greater portion of the sferics

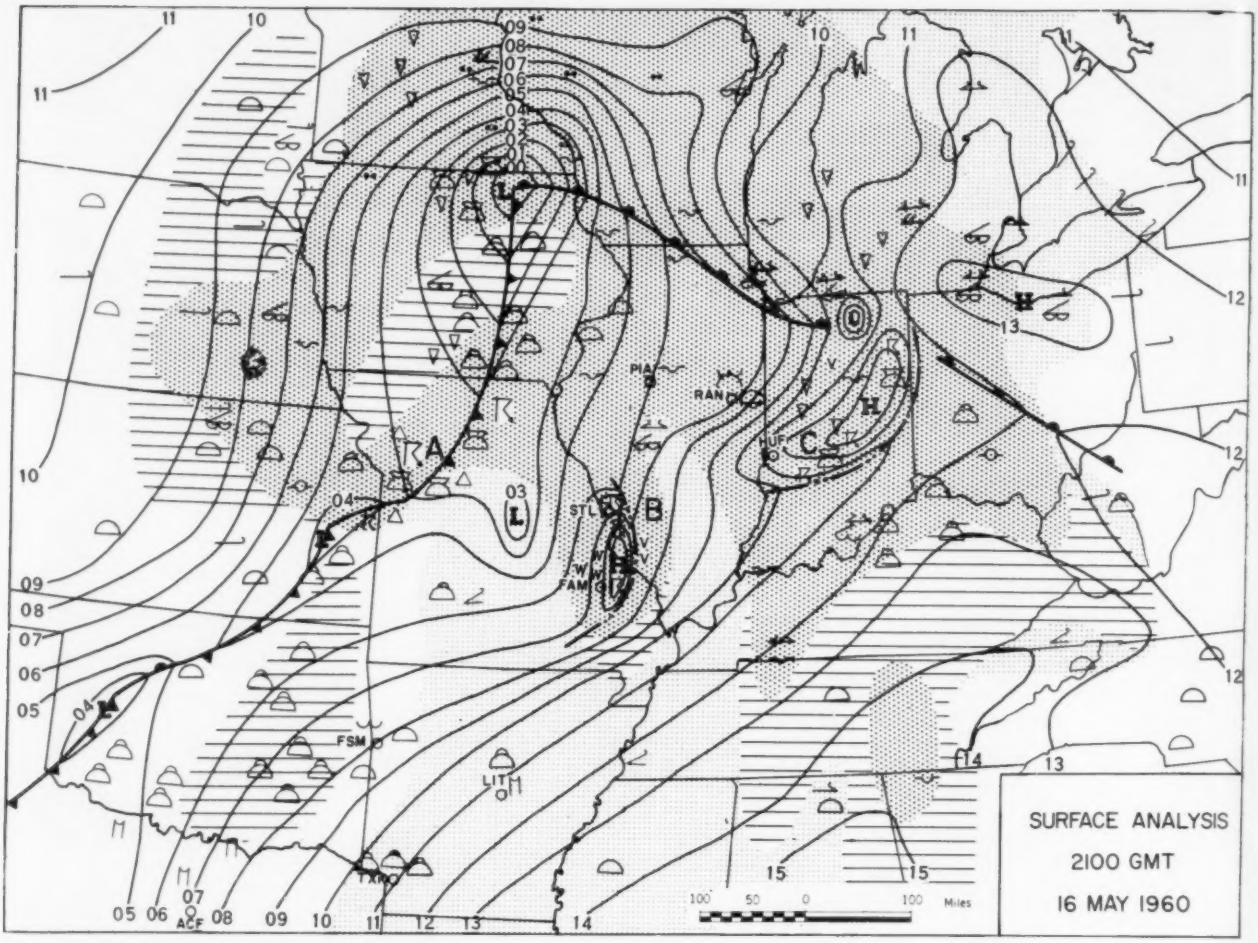

FIGURE 7.—Surface chart for 2100 GMT, May 16, 1960, showing, in addition to the pressure and frontal analysis, the observed cloud cover, observed cloud types, and observed weather. The cloud cover is separated into the four categories described in the text. Successive categories are lighter in shading. Category 1 (essentially overcast) is described by heaviest shading, while category 4 (clear or scattered) is unshaded. Cloud types, weather, fronts, etc., are represented by the usual symbols. The legend of figure 9 also applies.

return area to the extent that the boundaries are coincident at many points.

UPPER AIR STREAMLINE ANALYSES

Streamline analyses were performed (after the technique of Palmer et al. [9]) for the 5,000- and 20,000-ft. levels from the 1800 GMT May 16, 1960 and the 0000 GMT May 17, 1960 upper air observations over the central portion of the United States (figs. 11 and 12). The object of the analyses was to determine the configuration of low- and high-level jet streams and jet maxima for the purpose of locating a convective mechanism, as proposed by Beebe and Bates [1], which might be related to the bright clouds appearing in the TIROS I pictures from pass 659.

In short, the Beebe and Bates divergence models for location of the convective mechanism were evolved from a determination of the divergence fields about jet maxima at both low and high levels. The divergence field may be determined from the divergence term of the vorticity equation by evaluating from the wind field alone the advection of relative vorticity about a jet maximum. If the configuration of a high-level jet maximum over a low-level jet maximum is such that divergence is occurring over convergence, Beebe and Bates propose that the vertical motion and modification of the temperature distribution would release convective instability.

The analyses shown in figures 11 and 12 cannot be considered unique because of the sparseness of upper-air observations. A quantitative evaluation of the divergence term from these analyses would then be somewhat presumptuous for the scale we are considering here. Therefore, the models were applied on the 5,000- and 20,000-ft. charts to locate the convective mechanisms at the times considered. The models are the cases of (1) a jet stream of no curvature (fig. 11a), (2) a cyclonically

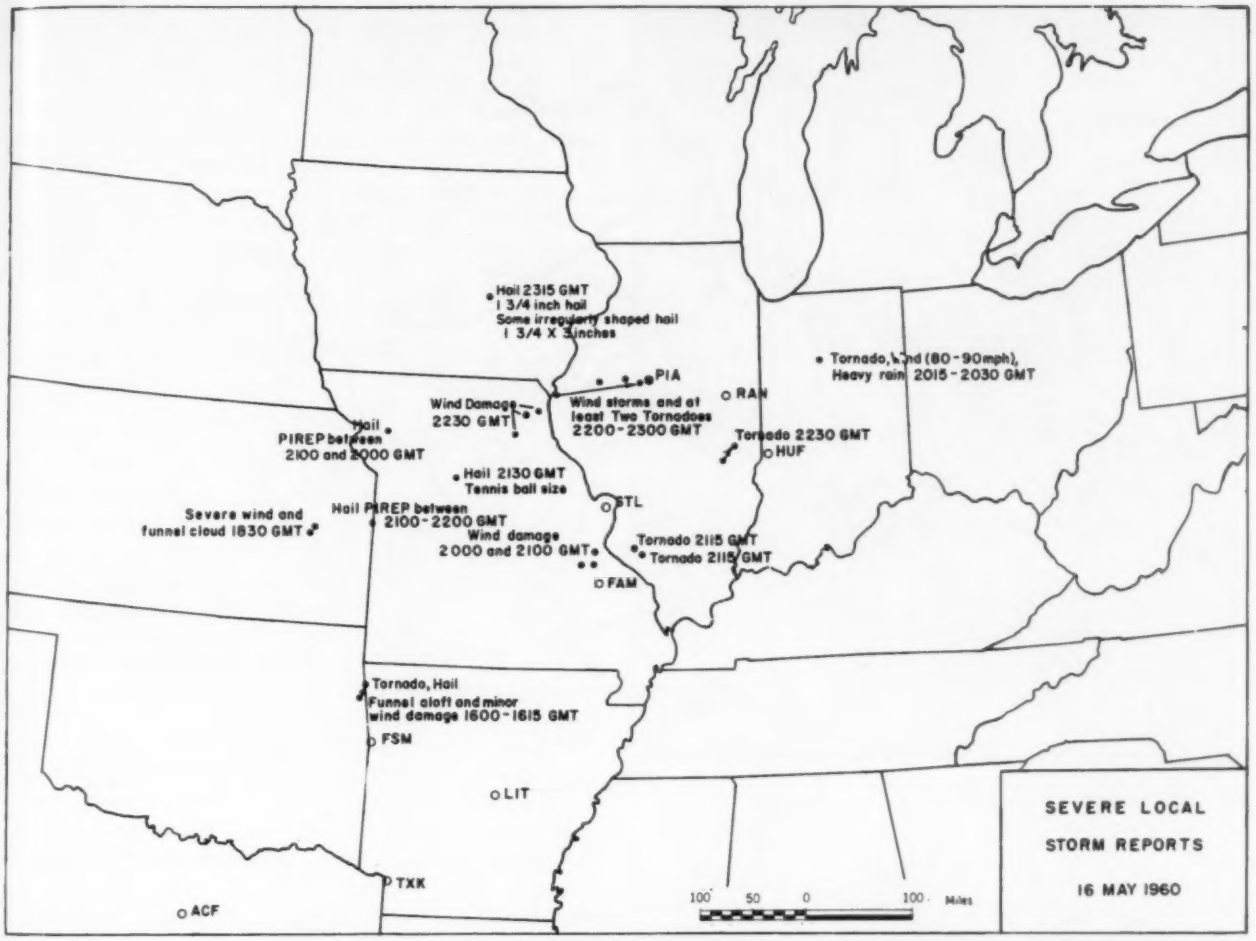

FIGURE 8.—Severe storm reports in the Middle West on May 16, 1960, Greenwich time. Other storms occurred in Kansas and Oklahoma, but these reports are not shown since they had no direct relation to the storms in the Middle West.

curved jet with the wind maximum located at the point of maximum curvature (figs. 12 a and b), and (3) an anticyclonically curved jet with the wind maximum located at the point of maximum curvature (fig. 11b). These models are simplified compared with the many jet structures which may occur, but nonetheless they are useful tools in synoptic meteorology.

Based on the 5,000-ft. and 20,000-ft. streamline charts for 1800 GMT, it was possible using the models to delineate with confidence one area where divergence occurred over convergence. That area (shaded in figs. 11 a and b) east of the jet axes lay over southern Missouri and northern Arkansas or just southeast of cloud mass B where severe weather began breaking out at 2000 GMT.

By 0000 GMT of May 17, 1960, the jet convective mechanism lay over portions of southeastern Iowa, northeastern Missouri, and western Indiana (shaded in figs. 12 a and b). Wind damage and tornadoes occurred in that area with system A during the 2-hour period prior to 0000 GMT. Numerous thunderstorms and some hail within cloud mass A (fig. 3) were forerunners of the tornadoes.

Thus, over the 6-hour interval between 1800 and 0000 GMT, low- and high-level jet maxima and consequently the dynamic convective mechanism were restricted to the immediate vicinity of the two areas of severe weather associated with the cloud masses A and B. Certainly agreement in location between the cloud masses at 2100 GMT and the mechanisms at 1800 and 0000 GMT is not as good as it might be. One must remember that a precise fix of the mechanism is hampered by the wide spacing of the upper air observations, and, in this case, by the lack of time agreement of the upper air observations with the TIROS pictures.

Significantly, the third group of thunderstorms (area C) was neither as severe as the more western systems nor directly under the influence of the jet maxima. During the interval 1800–0000 GMT, system C continually moved eastward away from the dynamic mechanism, lending further support to a decaying thunderstorm situation over Indiana.

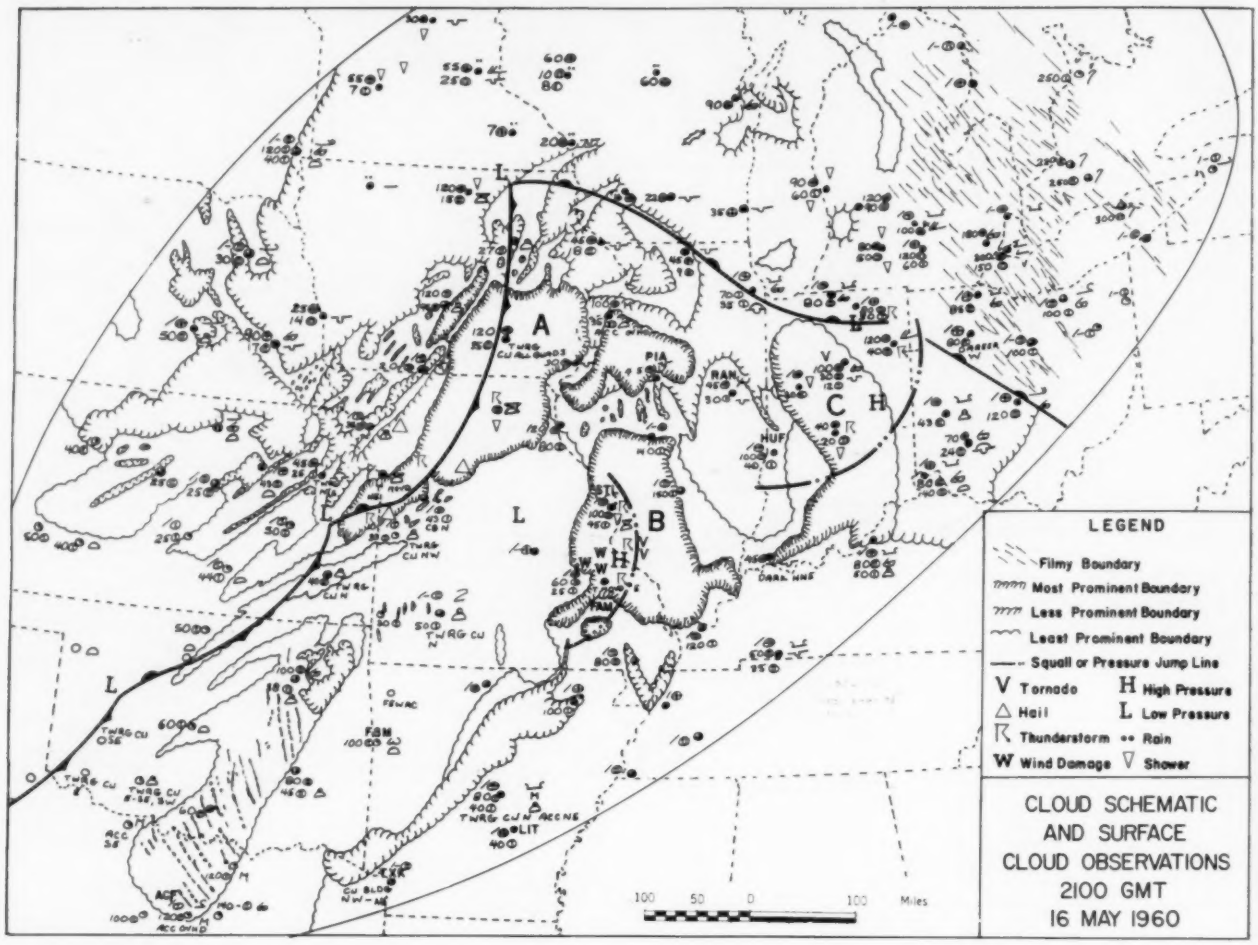

FIGURE 9.—Composite of TIROS cloud schematic and surface observations. Individual station plots give cloud cover, cloud heights, and cloud types. Other features of the diagram are given in the legend.

SURFACE NEPHANALYSIS

The surface-observed sky condition was analyzed according to the following four categories:

1. Overcast low and/or middle clouds; or overcast high clouds with at least broken low and/or middle clouds.
2. Broken low and/or middle clouds but high clouds not overcast if any appear.
3. Broken to overcast high clouds with clear to scattered low and/or middle clouds.
4. Clear skies or scattered low and/or middle clouds.

This form of nephanalysis was adopted since it might better correspond to the apparent cloud cover and brightness seen in the pictures, particularly if the premise is accepted that high clouds are not always readily visible in earth satellite photographs. Experience has shown that unless cirriform clouds are dense, the TIROS cameras do not usually detect them.

In the following few paragraphs, comparisons are made between the TIROS pictures (figs. 1–5) and the surface nephanalysis (fig. 7). The reader may find it beneficial to refer also to the TIROS schematic in figure 6.

In the cold air the overcast area (fig. 7) as described by category 1 above, conforms closely to the standard model of heavy clouds and steady precipitation extending from the warm front counterclockwise around the low pressure center. This overcast region may be discerned in figure 3 as an area of continuous, moderately bright cloud cover.

A second area of overcast skies (category 1) was located in the northern portion of the warm sector. That area contained the cloud masses A, B, and C (figs. 2 and 3).

Areas of broken low and/or middle cloudiness (hatched areas of fig. 7) over Oklahoma and in the central Plains States are reflected in the TIROS pictures as small-scale patches of clouds or as individual cloud elements, some organized into cloud streets.

Those areas on the surface nephanalysis (fig. 7) classi-

fied, under category 3, as broken or overcast high cloud (light dotted areas), are seen as either clouds of dull filmy appearance or areas of no cloudiness. In the eastern Lakes area (fig. 5), the clouds were filmy. Over south-central Missouri, figure 3 pictures a very dark area. Yet broken to overcast cirriform cloud cover with few or no lower clouds was reported in both locations (fig. 7). The observations indicated that the high clouds were dense over the eastern Lakes but thin over south-central Missouri.

4. CLOUD INTERPRETATION

In figure 9, the schematic of the five TIROS pictures is shown in composite with the surface cloud observations. From the preceding discussion of the nephanalysis in figure 7 and by inspection of figure 9, one may see that the surface observed cloud cover agrees well with the TIROS observed cloud cover.

There are several positions where the rectified clouds are not consistent with surface observations. These discrepancies indicate a maximum rectification error of about 20 miles. Two examples are Rantoul, Ill. (RAN) and Terre Haute, Ind. (HUF). Both stations reported considerable cloudiness yet lie in a dark portion of the picture which indicates little or no cloudiness. One can see from figure 9 that only a slight geographical readjustment in the rectified cloud schematic would be required to have these stations fall within a cloudy area.

Several interesting comparisons may be drawn from figure 9 with regard to observed clouds and the TIROS observations. For instance, those stations which fell within the bounds of the three very bright cloud masses (A, B, and C) all reported an overcast cover with at least broken clouds in the low and middle layers. These stations indicated a predominance of cumuliform clouds, with cumulonimbus and towering cumulus or showers and thunderstorms being most prevalent.

Observations of middle and high clouds between the numerous heavy cumulus structures suggest that the anvil tops united while spreading out under the influence of the strong winds in the upper levels. It is not surprising then that the cloud masses A, B, and C (figs. 3 and 4) should exhibit continuous cloudiness rather than individual, large cumulus clouds.

Figures 11b and 12b illustrate the strong flow present at 20,000 ft.; the flow pattern at 30,000 ft. (not shown) was very similar. The westerly and southwesterly winds over the clouds A, B, and C (fig. 9) explain the extension of the cloud masses to the east and northeast of the areas of heaviest convection. This effect is particularly noticeable in cloud B where the cloudiness protrudes 50 or more miles ahead of the squall or pressure jump line.

Another interesting feature of the pictures is the moderately bright cloud band oriented northeast-southwest through central Arkansas (fig. 2). Little Rock (LIT) and Texarkana (TXK) recorded towering cumulus to the north, and northwest through northeast, respectively (fig. 9). Both reports give credence to the cloud band position some 20 miles northwest of each station.

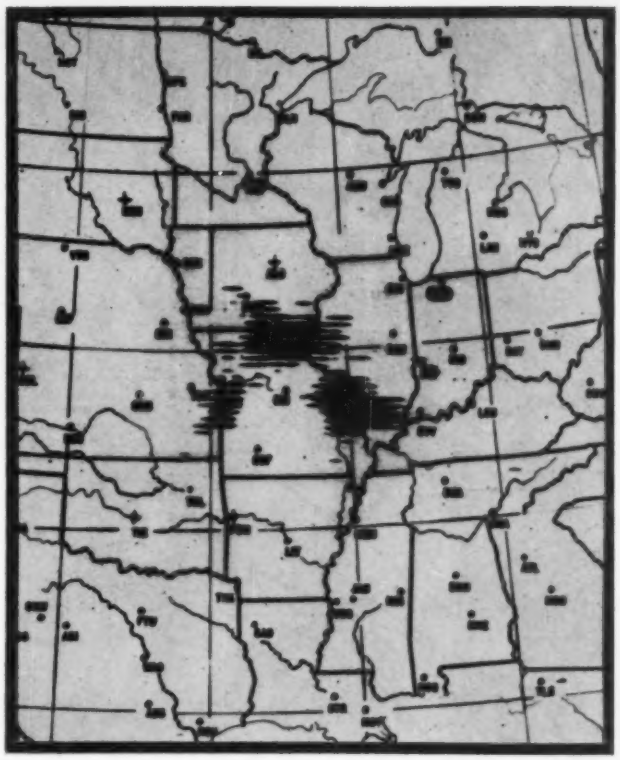

FIGURE 10.—Five-minute, four-station fixes of sferics observations at 2100 GMT, May 16, 1960.

A second apparently overcast area of moderate brightness as seen in the TIROS pictures occurred north of the warm front extending from the western Great Lakes area counterclockwise about the Iowa low pressure center into eastern Nebraska and western Iowa (fig. 9). Station observations within this area all indicated overcast skies while stratocumulus was the most predominantly reported cloud type.

In Kansas, portions of Nebraska, Oklahoma, and north central Texas, the pictures (figs. 1 and 2) convey the impression of broken to occasionally scattered cloud cover comprised largely of convective cells. Many small, individual elements can be seen, some grouped together in patches of irregular size and shape, and some organized into cloud streets. Though the surface observations (fig. 9) do not reveal the details of organization, scattered to broken cover of convective clouds was reported throughout the area—altocumulus castellanus in Texas and cumulus elsewhere.

5. CLOUD STREETS

Cloud streets have been a source of great interest with the advent of rocket and satellite photography.

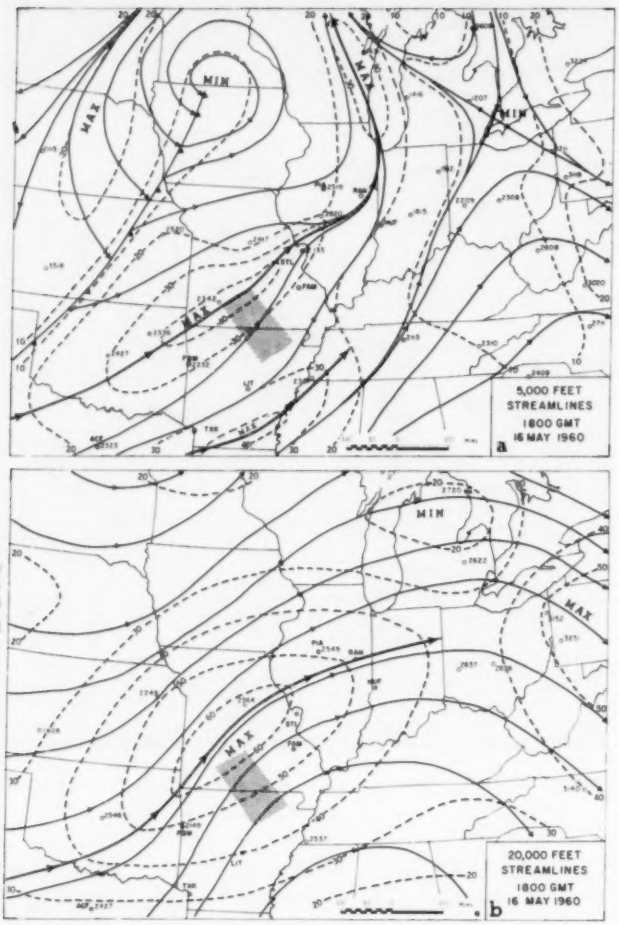

FIGURE 11.—Streamline analyses for May 16, 1800 GMT: (a) 5,000-ft. level; (b) 20,000-ft. level. Shaded area represents the region under the influence of the convective mechanism as determined by the Beebe and Bates [1] models using the 5,000- and 20,000-ft. levels. Jet streams are heavy solid lines; streamlines, light solid lines; and isotachs, dashed lines.

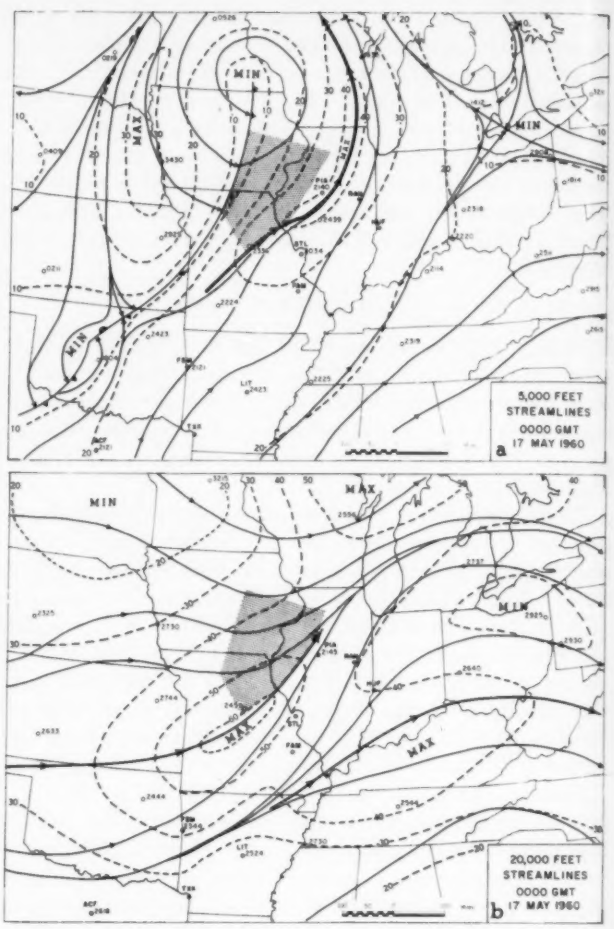

FIGURE 12.—Streamline analyses for May 17, 0000 GMT: (a) 5,000-ft. level; (b) 20,000-ft. level. See legend to figure 11.

The literature has suggested that cloud streets are related to the wind field. Meteorologists, therefore, have been hopeful that observations of cloud streets from satellite vehicles would aid in determining wind directions, particularly in sparse data areas.

Observations from rockets and satellites have shown streets both parallel and perpendicular to the flow or sometimes to the vertical shear. Theories supporting both extremes are propounded in the literature [6, 7]. Kuettner's [7] theory of winds parallel to the streets depends on a "nose" profile of wind speed where speed shear changes sign with height. Haurwitz's [6] theory, on the other hand, supports formation of either billow cloud rolls or cloud streets composed of polygonal cells at an internal boundary surface of density discontinuity, the rolls or streets being normal to the wind shear vector across the boundary.

Surface observations and a sounding in the vicinity of the cloud streets observed by TIROS I (figs. 1 and 2) over Oklahoma on May 16 suggest that these streets conform to the Haurwitz theory. The cloud bases were reported at 4,000 to 6,000 ft. (fig. 12) while the Fort Smith, Ark. (FSM) sounding (fig. 13a), though taken 3 hours earlier, indicated a temperature inversion at approximately the same altitude. The wind shear vector across the inversion surface or internal boundary at Fort Smith was normal to the cloud streets as rectified. Winds immediately below and above the inversion were 190° at 20 kt. and 230° at 37 kt., respectively, which determined a shear vector of 260° at 26 kt. The cloud streets generally formed an angle of 80° to 90° with the shear vector.

Haurwitz indicates that cloud rows can theoretically be at any angle except zero to the wind shear across an internal boundary surface but that normality to the wind

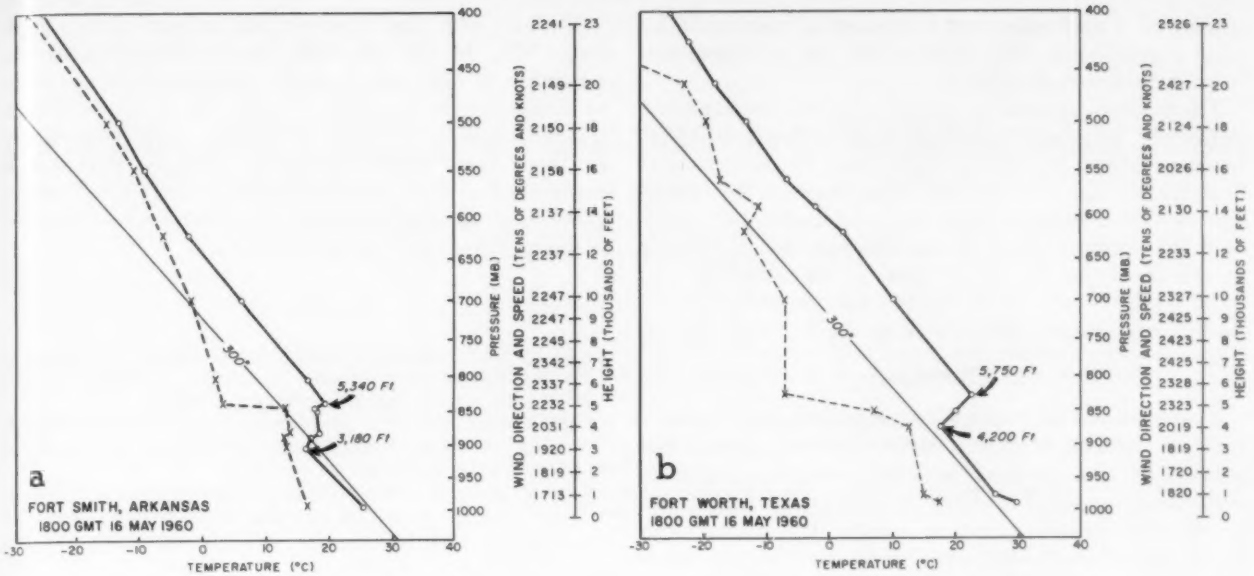

FIGURE 13.—(a) Fort Smith, Ark., sounding. (b) Fort Worth, Tex., sounding. The heavy solid line is the vertical temperature distribution; the broken line, the vertical dew-point distribution; and the light solid line, the 300° K. adiabat.

shear is the most plausible. For the case of perpendicularity, the simplified equation for maximum wavelength (L_∞) for rows or streets of infinite lateral extent is

$$L_\infty = \frac{\pi(\Delta U)^2 \overline{T}/g}{[\Delta T^2 + (\Delta U)^2 \overline{T}(\Gamma - \gamma)/g]^{1/2}} \qquad (1)$$

where g = acceleration of gravity
ΔU = shear speed across the internal boundary
$\overline{T}$ = mean absolute temperature of the two layers
ΔT = temperature difference across the boundary
Γ = adiabatic lapse rate or moist adiabatic rate if condensation occurs
γ = lapse rate of the atmosphere which is assumed equal either side of the boundary.

When the waves are of finite lateral extent, as when the streets are composed of cells, the wavelength according to equation (1) is modified as follows:

$$L = \frac{L_\infty}{[1 + L^2/\lambda^2]^{1/2}} \qquad (2)$$

where L equals wavelength of streets of finite lateral extent, and λ equals lateral wavelength or lateral spacing of cells.

Equations (1) and (2) were applied in the May 16 cloud street case using values from the 1800 GMT Fort Smith sounding. Though observed 3 hours earlier, the sounding was nearest the streets in time and space. The theoretical wavelengths or spaces between streets thus determined were 3.3 miles and 1.7 miles (assuming λ to be 1 mile) for waves of infinite and finite lateral extent, respectively. Since the cloud streets in the TIROS pictures appear to be made up of individual cloud cells, then the theoretical wavelength of 1.7 miles would seem to apply. However, the surface observations of cumulus congestus and size of the cloud elements in the pictures indicate the cellular structure is more complicated than the simple cells in streets of finite lateral extent. Then for purposes of this discussion the theoretical spacing of 3.3 miles as an initial condition will be considered. The cloud street spacing in the TIROS photographs is approximately 8 or 9 miles.

Riehl et al. [8] have noted apparent increases in cloud street spacing through enhancement of some streets and suppression of others, particularly when the cumulus became more vertically developed. Conover [3] has observed, through radar, major bands between which were minor bands, more closely spaced. He, too, has noted streets, using time lapse photography, that have disappeared or were suppressed within a pattern of streets. Though not speaking specifically of streets, Byers and Braham [2] observed preferred grouping of cells during the Thunderstorm Project in Florida.

Actually the theoretical treatment of Haurwitz is applicable only to clouds of small vertical development, whereas the streets seen in the pictures are composed of conglomerates of cumulus cells of considerable vertical development. It is reasonable to suppose that the internal boundary waves provided sufficient mechanical vertical motion to release the latent instability for the formation of cumulus congestus. Further, as the cumulus developed some streets were damped while others were accentuated, thus increasing the wavelength. The observed street

613342—61——6

spacing of 8 or 9 miles and a theoretical spacing of 3.3 miles suggest that every third street was enhanced and those in between suppressed.

The presence of cloud streets over extreme north central Texas (fig. 1) is not easily explained. The clouds were based at 12,000 ft., much higher than the inversion at Fort Worth (fig. 13b), and the shear between the 12,000- and 14,000-ft. levels, though small, approximately paralleled the streets. There is then no apparent relationship to the Haurwitz theory at time of the sounding. At cloud level, the wind and streets were perpendicular precluding any obvious relationship to the Kuettner theory.

6. SUMMARY

Evidence has been presented supporting the premise that the isolated brightest mesoscale cloud masses seen in the TIROS pictures of May 16, 1960 were organized systems of numerous thunderstorms capable of producing severe local storms. Further, two of the masses were developing where the strongest convective mechanism was present; that is, the clouds were associated with low- and high-level jet stream maxima and surface fronts or pressure jump lines. The third bright area, though not isolated at picture time, was a manifestation of a decaying group of thunderstorms which had moved eastward for several hours, away from the jet convective mechanism to the west.

Then, with regard to cloud interpretation, it is not surprising that the bright masses were concentrations of cumulus congestus and cumulonimbus clouds observed from the surface. In general, the brightest areas were both overcast and cumuliform in nature, the smaller-scale areas representing cumulus of vertical development and the large-scale area, stratocumulus. Scattered to broken cumulus or cumulus congestus clouds appear in the pictures as darker areas comprised of small cells or irregular bright patches, some organized and some not. Cirriform clouds, overall, gave the poorest reflectivity or none at all, particularly where thin.

The cloud streets appear related to the theory suggesting a perpendicular orientation between wind shear through an inversion and cloud streets which form there.

We have seen that TIROS I has at least on two occasions, May 16 and 19, 1960, clearly demonstrated the capability of television-equipped meteorological satellites to detect severe-weather-producing cloud masses, both prior to storm development and during storm occurrence. In the future, vastly improved television coverage is anticipated in both time and space so that satellites are likely to be effective tools for both detection and tracking of mesoscale severe weather systems.

REFERENCES

1. R. G. Beebe and F. C. Bates, "A Mechanism for Assisting in the Release of Convective Instability," *Monthly Weather Review*, vol. 83, No. 1, Jan. 1955, pp. 1–9.
2. H. R. Byers and R. R. Braham, Jr., "Thunderstorm Structure and Circulation," *Journal of Meteorology*, vol. 5, No. 3, June 1948, pp. 71–86.
3. J. H. Conover, "Cloud Patterns and Related Air Motions Derived by Photography," *Final Report* on Contract No. AF 19(604)–1589, Harvard University, Blue Hill Meteorological Observatory, 1959, 268 pp. (see pp. 246–252).
4. Department of the Air Force, Air Weather Service, "Uses of Sferics in Analysis and Forecasting," *Air Weather Service Manual* 105–38, 1953, 32 pp.
5. T. Fujita, H. Newstein, and M. Tepper, "Mesoanalysis: An Important Scale in the Analysis of Weather Data," U.S. Weather Bureau, *Research Paper* No. 39, 1956, 83 pp.
6. B. Haurwitz, "Internal Waves in the Atmosphere and Convective Patterns," *Annals of the New York Academy of Sciences*, vol. 48, 1949, pp. 722–748.
7. J. Kuettner, "The Banded Structure of the Atmosphere," *Tellus*, vol. 11, No. 3, Aug. 1959, pp. 267–294.
8. H. Riehl, W. S. Gray, J. S. Malkus, and C. Ronne, "Cloud Structure and Distributions over the Tropical Pacific, Part I," Woods Hole Oceanographic Institution, *Technical Report* No. 5, 1959, 61 pp. (Unpublished manuscript).
9. C. E. Palmer, C. W. Wise, L. J. Stempson, and G. H. Duncan, "The Practical Aspect of Tropical Meteorology," *Air Force Surveys in Geophysics*, No. 76, U.S. Air Force, Geophysics Research Directorate, 1955, 195 pp., (see pp. 65–100).
10. Staff Members, Meteorological Satellite Laboratory, U.S. Weather Bureau, "Some Meteorological Results from TIROS I," 1961, to be published in Report on TIROS I by the National Aeronautics and Space Administration, (in press).
11. L. F. Whitney and S. Fritz, "A Tornado-Producing Cloud Pattern Seen from TIROS I," *Bulletin of the American Meteorological Society*, vol. 42, No. 9, Sept. 1961, pp. 603–614.

ON SHORT- AND LONG-TERM VARIATIONS IN QUASI-BAROTROPIC FLOW

A. WIIN-NIELSEN*

Joint Numerical Weather Prediction Unit, Air Weather Service Suitland, Md.

[Manuscript received July 3, 1961; revised August 17, 1961]

ABSTRACT

A comparison is made between the stability properties of the non-divergent and divergent one-parameter models. It is shown that the introduction of divergence in the one-parameter model reduces the rate of growth of unstable disturbances and confines the instability to a more narrow band of wavelengths.

Changes in zonal momentum, momentum transports, and energy conversions between mean flow kinetic energy and eddy kinetic energy are investigated in the linear case, as well as by extended integrations of the spectral form of the prognostic equations allowing only a few wave numbers.

Long-term variations in barotropic flow, where the flow is initially stable, are investigated using the spectral formulation, but allowing only as many wave numbers as are needed to investigate variations in the profile of the zonal wind.

1. INTRODUCTION

The stability of barotropic flow has been investigated in some detail in earlier studies, notably by Kuo [8] and Eliasen [7]. The extensive use of the barotropic model in operational forecasting has caused a continuing interest in the performance of this model. Certain modifications have been introduced in the forecast equations to alter the forecasts of planetary waves. These semi-empirical corrections are described by Cressman [5] and Wiin-Nielsen [17]. The so-called divergent baratropic model is probably going to be used in operational forecasting for some time to come. It is therefore of interest to study the stability of disturbances in this model and to compare the results with the corresponding results for the non-divergent, one-parameter model. The first part of this paper is concerned with such a study.

There has been recently an increasing interest in the performance of the numerical prediction models when they are integrated over extended periods of time up to several days, weeks, or even months. Thompson [15] has developed a heuristic theory of long-period velocity variations in barotropic flow. It was especially shown from this theory that intense jet stream maxima have a tendency to split into two maxima traveling toward the north and the south, a situation which seems to be characteristic of certain types of atmospheric flow connected with blocking. Lorenz [9] has shown how the barotropic vorticity equation can be reduced to a maximum simplification and has investigated the extended time-integration of such a model. The same approach was used by Bryan [3] to perform experiments with a simple baroclinic model dealing with the different regimes caused by changes of the rotation of the earth and the rate of heating

Saltzman [14] has investigated the non-linear interaction between the zonal flow, large-scale, and small-scale disturbances by an extended integration of the barotropic vorticity equation using a limited number of Fourier components.

The general circulation experiments performed by Phillips [12] deal with an integration of the two-parameter, quasi-geostrophic models over extended periods including adiabatic effects and friction. Extensions of Phillips' work to more realistic models based on the primitive equations and having a greater vertical resolution in addition to more realistic heating and frictional effects are underway in different research groups.

The second part of this paper will describe the variations in the flow of a barotropic fluid on a large time scale. We shall be concerned partly with a flow which is initially unstable, and partly with a flow which is initially stable. Integral quantities and their variation in time will be given because we are not interested in the details of the individual disturbances. The changes in the profile of the zonal wind, the momentum transports, and the energy conversions between the kinetic energies of the mean zonal flow and the disturbances will be reproduced in detail. We shall use a simplification of the barotropic vorticity equation for these purposes of a type similar to Lorenz's minimum form, but shall allow only as many wave components as are needed to describe a zonal wind profile which has at least two maxima.

2. STABILITY STUDY OF THE DIVERGENT, ONE-PARAMETER MODEL

The prognostic equation for the divergent, one-param-

*Present affiliation: National Center for Atmospheric Research, Boulder, Colo.

eter model will be given in the form:

$$\partial\nabla^2\psi/\partial t+\mathbf{V}\cdot\nabla(\nabla^2\psi+f)=q^2\partial\psi/\partial t \tag{2.1}$$

where q^2 is determined by the expression:

$$q^2=\frac{f_0^2}{\sigma^2}\frac{d\sigma}{dp}\frac{dA}{dp}. \tag{2.2}$$

The notations have the following meaning: ψ is the stream function, $\mathbf{V}=\mathbf{k}\times\nabla\psi$ the horizontal non-divergent wind, $\mathbf{k}$ a vertical unit vector $\nabla^2=\partial^2/\partial x^2+\partial^2/\partial y^2$ the two-dimensional Laplacian, and f the Coriolis parameter. In equation (2.2) $\sigma=-(\alpha/\theta)\ \partial\theta/\partial p$ is a measure of static stability, f_0 a standard value of the Coriolis parameter, and $A\ (p)$ is the empirical function describing the vertical variation of the horizontal wind around the level where the vorticity equation is applied (500 mb.), according to the assumption

$$\mathbf{V}(x,y,p,t)=A(p)\mathbf{V}_5(x,y,t). \tag{2.3}$$

The subscript 5 has been dropped from the start in equation (2.1). A derivation leading to this particular form of the prognostic equation has been given by Wiin-Nielsen [17].

In the first part of this section we shall consider disturbances on a zonal flow in a region bounded to the north and south by rigid walls. We shall divide any quantity into its zonal mean and deviations from the zonal means. For an arbitrary quantity we write:

$$a=\bar{a}+a' \tag{2.4}$$

where

$$\bar{a}=\frac{1}{L}\int_0^L a\,dx. \tag{2.5}$$

L is the largest possible wavelength.

When we substitute in (2.1) and neglect second order terms we may derive the following equation:

$$\nabla^2\frac{\partial\psi'}{\partial t}+\bar{U}\frac{\partial\zeta'}{\partial x}+\left(\beta-\frac{\partial^2\bar{u}}{\partial y^2}\right)v'=q^2\frac{\partial\psi'}{\partial t}. \tag{2.6}$$

We shall consider perturbations in the eddy stream function of the type:

$$\psi'(x,y,t)=\alpha(y)e^{i\mu(x-ct)}. \tag{2.7}$$

When we substitute (2.7) into (2.6) we can write the latter equation in the form:

$$(\bar{u}-c)\left[\frac{d^2\alpha}{dy^2}-\mu^2\alpha\right]+\left[\beta-\frac{d^2\bar{u}}{dy^2}+q^2c\right]\alpha=0. \tag{2.8}$$

The general eigenvalue problem to find for which connected values of u and c there exist solutions to equation (2.8), will not be treated in this paper, but we shall restrict ourselves in this first analytical treatment to an initial zonal wind profile of the type

$$\bar{u}=B\left(1-\cos\frac{2\pi}{D}y\right). \tag{2.9}$$

Interpreting D as the distance between the walls we consider a profile where $u=0$ at both walls and has a value $u=2B$ for $y=D/2$, i.e., in the center of the channel.

We shall in the following use an expansion of the function $\alpha=\alpha\ (y)$ in the form:

$$\alpha(y)=\sum_{n=1}^{N}\alpha_n\sin\ (n\lambda y) \tag{2.10}$$

where $\lambda=\pi/D$. The expression (2.10) for the meridional dependence of the perturbation stream function is chosen in such a way that ψ' always disappears at the northern and southern boundaries of the region. The meridional velocity component $v=v'$ will therefore also vanish at the boundaries, and the boundary condition corresponding to rigid walls is therefore automatically satisfied.

The expression for $\alpha\ (y)$ is inserted in equation (2.8) and we obtain after reduction a set of linear homogeneous equations which can be used to determine the possible values of c and the ratios between the values of α_n. The resulting set of equations may be written in the form:

$$\frac{1}{2}\left(\mu^2+(n^2-4n)\lambda^2\right)B\alpha_{n-2}+\left((\mu^2+n^2\lambda^2)(c-B)+\beta+q^2c\right)\alpha_n+\frac{1}{2}\left(\mu^2+(n^2+4n)\lambda^2\right)B\alpha_{n+2}=0. \tag{2.11}$$

We notice in the set (2.11) that it divides naturally into two sets corresponding to even and odd values of n. It should further be mentioned that we must put a finite value on the maximum number N which n may obtain in order to determine the values of c. We shall in this study only be concerned with small and odd values of n and N. Larger values of N have been considered by Eliasen [7] but mostly in cases where the β-effect, and naturally also the effect of divergence, was excluded by assumption.

Restricting ourselves to the most simple case $N=3$ we obtain the following set of equations from (2.11)

$$\left.\begin{aligned}\left\{(\lambda^2+\mu^2+q^2)c+\beta-\frac{1}{2}B(3\mu^2-\lambda^2)\right\}\alpha_1+\frac{1}{2}(\mu^2+5\lambda^2)B\alpha_3=0\\ \frac{1}{2}(\mu^2-3\lambda^2)B\alpha_1+\left\{(9\lambda^2+\mu^2+q^2)c+\beta-B(9\lambda^2+\mu^2)\right\}\alpha_3=0\end{aligned}\right\} \tag{2.12}$$

A set of equations very similar, but not identical to (2.12) may naturally also be obtained by applying the same technique as Charney [4] in deriving the stability criterion for a two-parameter model with horizontal as well as vertical shear. Instead of the series (2.10) one obtains the equations corresponding to (2.12) by applying

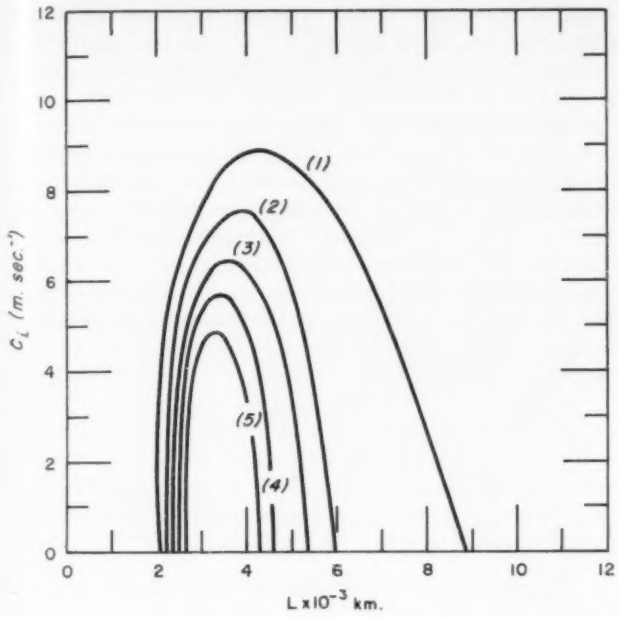

FIGURE 1.—The imaginary part, c_i, of the solution to equation (2.13) as a function of the zonal wavelength for a maximum meridional wavelength of 4000 km., B=30 m. sec.$^{-1}$ Curve (1): $\beta=0$, $q^2=0$; (2): $\beta=\beta_{45}$, $q^2=0$; (3): $\beta=\beta_{45}$, $q^2=0.5\times10^{-12}$ m.$^{-2}$; (4): $\beta=\beta_{45}$, $q^2=1.0\times10^{-12}$ m.$^{-2}$; (5): $\beta=\beta_{45}$, $q^2=1.5\times10^{-12}$ m.$^{-2}$

the linearized equation (2.8) in the center of the channel and midway between the center and the wall. Meridional derivatives are replaced by finite differences. It is a matter of convenience whether one or the other procedure is used.

The possible values of c are now determined from the condition that the determinant of the system (2.12) has to vanish in order to have non-trivial solutions. This condition leads to the equation:

$$(\lambda^2+\mu^2+q^2)(9\lambda^2+\mu^2+q^2)c^2+[2\beta(5\lambda^2+\mu^2+q^2) -1/2B(5\mu^4+9\lambda^4+46\mu^2\lambda^2+5\mu^2q^2 +17\lambda^2q^2)]c+[\beta^2-1/2\beta B(5\mu^2+17\lambda^2) +1/4B^2(5\mu^4-3\lambda^4+50\mu^2\lambda^2)]=0 \quad (2.13)$$

The frequency equation (2.13) has been solved numerically for a number of cases. These cases fall into different series. For each value of the maximum, meridional wavelength ($2\pi/\lambda$) it was decided to vary the zonal wavelength ($L=2\pi/\mu$) in each series keeping q constant. The effect of β and of divergence was tested by keeping $\beta=0$ and $q=0$ in one series of computations. The results of these computations are given in figures 1, 2, and 3.

The maximum, meridional wavelength in the computations illustrated in figure 1 was 4,000 km. and the maximum zonal speed in the initial profile 60 m. sec.$^{-1}$ (B= 30 m. sec.$^{-1}$). This case corresponds to a rather narrow intense jet stream. The abscissa in the figure is the zonal

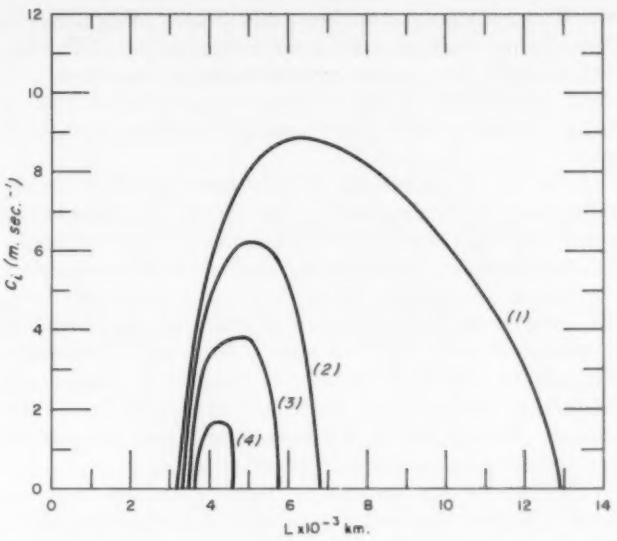

FIGURE 2.—The imaginary part, c_i, of the solution to equation (2.13) as a function of the zonal wavelength for a maximum meridional wave length of 6,000 km., B=30 m. sec.$^{-1}$ The curves (1), (2), (3), and (4) as in figure 1.

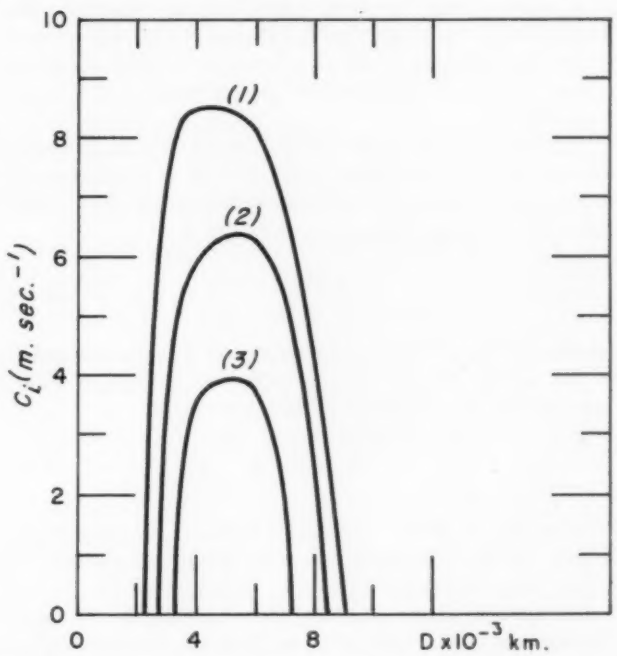

FIGURE 3.—The imaginary part, c_i, of the solution to equation (2.13) as a function of the meridional wavelength for a fixed zonal wavelength of 5,000 km., B=30 m. sec.$^{-1}$ The curves (1), (2), and (3) as in figure 1.

wavelength in the unit of thousands of km., while the ordinate is the imaginary part of the wave speed: c_i. The figure contains five curves corresponding to the cases: (1) $\beta=0$, $q=0$; (2) $\beta=\beta_{45}$, $q=0$; (3) $\beta=\beta_{45}$, $q=0.5\times10^{-12}$ m.$^{-2}$; (4) $\beta=\beta_{45}$, $q=1.0\times10^{-12}$ m.$^{-2}$; and (5) $\beta=\beta_{45}$, $q=1.5\times10^{-12}$ m.$^{-2}$

It is seen by comparing the two first cases that the β-effect has a stabilizing influence on the perturbations in the sense that the magnitude of c_i is smaller for $\beta\neq0$ than in the case $\beta=0$ and also that the band of zonal wavelengths for which instability occurs is more narrow for $\beta\neq0$. By comparing the first two cases with the last three it is furthermore seen that the effects of q, which measures the intensity of the divergence implied by the model, are to further decrease the instability of the waves in the model. The divergent, one-parameter model is therefore more stable than the non-divergent model.

The results are verified by figure 2, which contains similar calculations with the maximum, meridional wavelength at 6,000 km. The important new information contained in this figure is that the waves are more stable when the meridional wavelength is increased. For D= 6,000 km. it is seen that all wavelengths are stable in the case of $\beta=\beta_{45}$ and $q=1.5\times10^{-12}$m.$^{-2}$ and only the waves in a narrow band around 4,000 km. are unstable for $\beta=\beta_{45}$ and $q=1.0\times10^{-12}$m.$^{-2}$. Figure 3 contains curves giving the imaginary root as a function of the meridional wavelength for a fixed value of the zonal wavelength, $L=5{,}000$ km.

The information contained in figures 1, 2 and 3 may also be expressed in terms of the time, T, it would take to double the amplitude of the unstable perturbation. This time can be determined from the formula

$$T=\frac{\ln 2}{\mu c_i} \tag{2.14}$$

where c_i is the positive, imaginary part of the wave speed. If the wavelength $L=2\pi/\mu$ is expressed in the unit 1,000 km., c_i in m. sec.$^{-1}$, and T in days we obtain

$$T=1.28\frac{L}{c_i}. \tag{2.15}$$

The curves in figures 1, 2 and 3 indicate doubling times which may be as short as 0.5 day, but more typically are of the order 1–2 days.

The general conclusion from these calculations is therefore that unstable waves are possible even when the β-effect and the divergence effects are included in the analysis. Both of these effects have a stabilizing influence on the waves in the sense that the waves become more stable for larger values of β and q as they do for larger values of the maximum, meridional wavelength.

The general validity of the conclusions which have been reached in this section may be questioned because only the terms corresponding to $n=1$ and $n=3$ in (2.10) have been included in the frequency equation (2.13). If we also included the next odd value, $n=5$, the result would be that (2.13) would be replaced by a cubic equation, while the corresponding equation would be of the fourth degree if also $n=7$ were included. A priori the possibility exists that several amplifying modes will be present in the solution, and that the growth rate of these modes is different from the one found in this section. Such conditions are found in the theory of baroclinic stability (Charney [4], Murray [11]). In the case of barotropic stability, under investigation here, there exists a limited amount of information regarding the higher modes in the paper by Eliasen [7], who has found the roots in the frequency equation up to and including $n=8$. In the case of a symmetric, harmonic velocity profile in the zonal current he finds for $n\leq8$ that only one unstable mode exists, and that the growth rate is the same for $3\leq n\leq6$, but somewhat smaller for $n=7$ and $n=8$. It is therefore likely that the diagrams in figures 1, 2, and 3 contain the essential features of the stability of the quasi-barotropic flow, although the problem needs further investigation.

3. SECOND-ORDER MOMENTUM CHANGES

It is of interest to see what we can say from the solution of this particular perturbation problem about the second-order effects of the perturbations on the mean flow. Such second-order effects on the mean flow will give the initial changes, but after a while the mean flow will have changed so much that the solution of the perturbation problem no longer applies, which means that the mean flow now starts to alter the structure of the perturbations in a way radically different from our solution. This particular problem will be treated by numerical calculations in the later section.

The second-order changes in the mean flow can be found from the first equation of motion in a form applicable to the model:

$$\frac{\partial u}{\partial t}+\frac{\partial uu}{\partial x}+\frac{\partial uv}{\partial y}=-\frac{\partial\phi}{\partial x}+fv. \tag{3.1}$$

Defining now

$$\overline{u}=\frac{1}{L}\int_0^L u\,dx \tag{3.2}$$

and writing

$$u=\overline{u}+u',\ v=v',\ \text{since}\ \overline{v}=\frac{\overline{\partial\psi}}{\partial x}=0 \tag{3.3}$$

we obtain from (2.14)

$$\frac{\partial\overline{u}}{\partial t}=-\frac{\partial\overline{u'v'}}{\partial y}. \tag{3.4}$$

The initial changes in the zonal wind can, therefore, be computed from the convergence of the momentum transport of the perturbations. We must next evaluate this quantity from the solution of the perturbation problem. The general solution for the perturbation

stream function can be written (see equations (2.7) and (2.10)):

$$\psi'(x,y,t)=\{\alpha_1^{(1)}\sin\lambda y+\alpha_3^{(1)}\sin 3\lambda y\}e^{i\mu(x-c_1t)}+\{\alpha_1^{(2)}\sin\lambda y+\alpha_3^{(2)}\sin 3\lambda y\}e^{i\mu(x-c_2t)} \quad (3.5)$$

where c_1 and c_2 are the two solutions of the frequency equation (2.13) and $\alpha_1^{(1)}$, $\alpha_3^{(1)}$, $\alpha_1^{(2)}$, and $\alpha_3^{(2)}$ are the four (unknown) amplitudes of the wave components in the solution. The amplitudes (α) will, in general, be complex numbers if the wave speed c is complex. Next let the initial perturbation stream function be given by

$$\psi_0'(x,y)=(A_1\sin\lambda y+A_3\sin 3\lambda y)e^{i\mu x}. \quad (3.6)$$

We have then the following four equations to determine the amplitudes. Two equations are determined by the condition that the expression (3.5) has to agree with (3.6) for $t=0$, giving:

$$\left.\begin{aligned}\alpha_1^{(1)}+\alpha_1^{(2)}&=A_1\\ \alpha_3^{(1)}+\alpha_3^{(2)}&=A_3.\end{aligned}\right\} \quad (3.7)$$

The remaining two equations are determined by one of the two equations (2.12), which has to be satisfied for $c=c_1$ and $c=c_2$. Using the first of the equations (2.12) we obtain

$$\left.\begin{aligned}F(c_1)\alpha_1^{(1)}+G\alpha_3^{(1)}&=0\\ F(c_2)\alpha_1^{(2)}+G\alpha_3^{(2)}&=0\end{aligned}\right\} \quad (3.8)$$

where $F(c)$ and G are defined by the expressions

$$F(c)=\left(1+\frac{\lambda^2}{\mu^2}+\frac{\mathcal{Q}^2}{\mu^2}\right)c+\frac{\beta}{\mu^2}-\frac{1}{2}B\left(3-\frac{\lambda^2}{\mu^2}\right) \quad (3.9)$$

and

$$G=\frac{1}{2}\left(1+5\frac{\lambda^2}{\mu^2}\right)B. \quad (3.10)$$

The system (3.7), (3.8) becomes eight linear, inhomogeneous equations when the amplitudes (α) and wave velocity (c) are written as complex numbers and the equations are separated into real and imaginary parts. Let the wave speeds be written:

$$c_1=R+iS, \quad c_2=R-iS \quad (3.11)$$

and the amplitudes:

$$\left.\begin{aligned}\alpha_1^{(1)}&=X_1+iX_2\\ \alpha_1^{(2)}&=Y_1+iY_2\\ \alpha_3^{(1)}&=Z_1+iZ_2\\ \alpha_3^{(2)}&=V_1+iV_2\end{aligned}\right\} \quad (3.12)$$

It is obvious that the eight quantities: X_1, X_2, Y_1, Y_2, Z_1, Z_2, V_1, and V_2 can be determined from (3.7) and (3.8) when R and S have been determined from the solution of (2.13). We may therefore consider the real and imaginary parts of the amplitudes of the wave components as known. The final expression for the perturbation stream function may then be written:

$$\begin{aligned}\psi'(x,y,t)=e^{\mu St}\{&(X_1\sin\lambda y+Z_1\sin 3\lambda y)\cos\mu(x-Rt)\\ &-(X_2\sin\lambda y+Z_2\sin 3\lambda y)\sin\mu(x-Rt)\}\\ +e^{-\mu St}\{&(Y_1\sin\lambda y+V_1\sin 3\lambda y)\cos\mu(x-Rt)\\ &-(Y_2\sin\lambda y+V_2\sin 3\lambda y)\sin\mu(x-Rt)\}\end{aligned} \quad (3.13)$$

From the knowledge of the expression for the perturbation stream function it is now a straightforward (although tedious) computation to evaluate the convergence of the meridional transport of momentum to be used in (3.4). We find:

$$\frac{\partial\bar{u}}{\partial t}=2\mu\lambda^2[e^{2\mu St}(X_1Z_2-X_2Z_1)+e^{-2\mu St}(Y_1V_2-Y_2V_1)+(V_1X_2-V_2X_1+Z_1Y_2-Z_2Y_1)]\cdot M(y) \quad (3.14)$$

where

$$M(y)=\cos 4\lambda y-\cos 2\lambda y. \quad (3.15)$$

It can be shown that for our case we will always have

$$-(X_1Z_2-X_2Z_1)=(Y_1V_2-Y_2V_1)=N^* \quad (3.16)$$

and

$$V_1X_2-V_2X_1+Z_1Y_2-Z_2Y_1=0. \quad (3.17)$$

Using this information we may write (3.14) in the form:

$$\frac{\partial\bar{u}}{\partial t}=-4\mu\lambda^2N^*\sinh(2\mu St)\cdot M(y) \quad (3.18)$$

or by integration

$$\bar{u}(y,t)=\bar{u}(y,0)-2\frac{\lambda^2N^*}{S}[\cosh(2\mu St)-1]\cdot M(y). \quad (3.19)$$

In the cases which have been treated numerically it has invariably shown up that N^* is a positive quantity. This result is in agreement with remarks made by Kuo [8], on the basis of results obtained by Tollmien [16], and we shall show later that we can obtain this result ($N^*>0$) from physical considerations of the energy conversions between eddy kinetic and mean kinetic energy.

Taking this result for granted at the moment we can then find qualitatively what will happen to the profile of the zonal wind. The function $M(y)$ is plotted in figure 4 as a function of y/D. It has a positive maximum in the center of the channel and negative minima on both sides. Since furthermore $[\cosh(2\mu St)-1]$ is positive for $t>0$ it follows that the last term on the right side in (3.19) has the opposite sign of $M(y)$. We can therefore expect

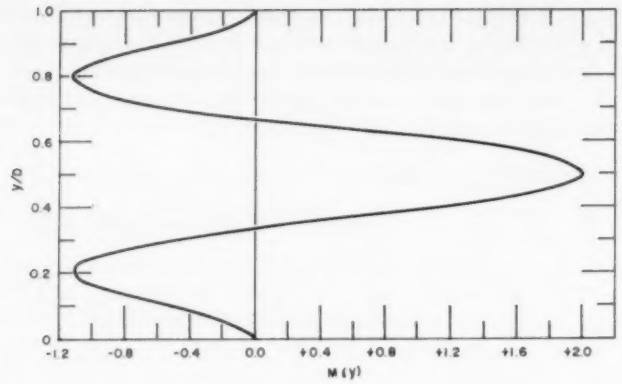

FIGURE 4.—The function $M(y)$ as defined by equation (3.15).

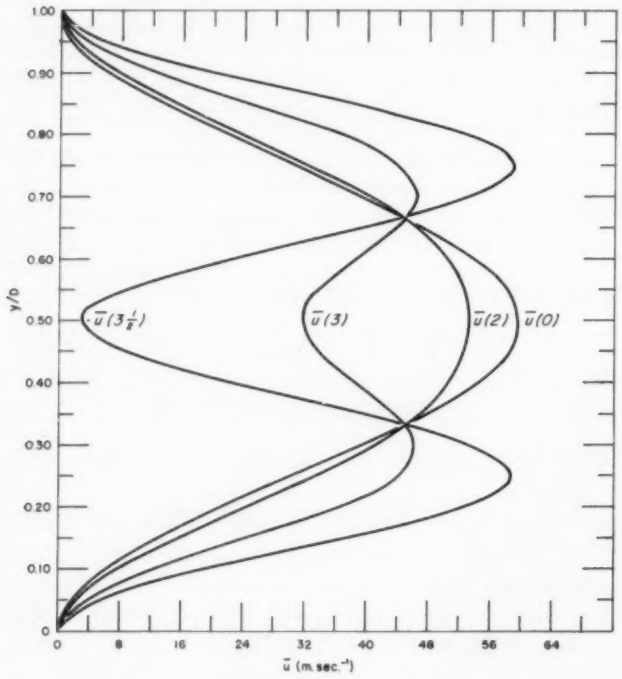

FIGURE 5.—The profile of the zonal wind initially and at 2, 3, and 3.5 days computed from equation (3.19) with $\beta=\beta_{45}$, $q^2=0$, zonal wavelength 5,000 km., width of the channel 3,000 km., $B=30$ m. sec.$^{-1}$, A_1 corresponds to 5 m. sec.$^{-1}$, and $A_3=0$.

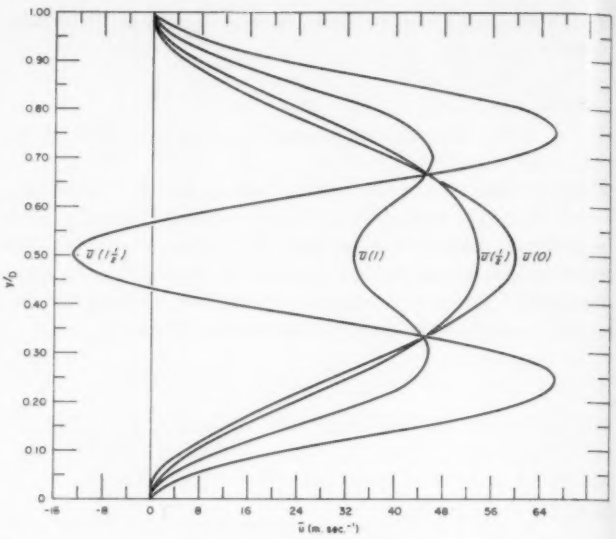

FIGURE 6.—The profile of the zonal wind initially and at 0.5, 1.0, and 1.5 days computed from equation (3.19) with parameters as in figure 5 except A_3 corresponding to 5 m. sec.$^{-1}$

that the initial maximum in $\overline{u}(y,0)$ will be reduced during the first time period after an integration has started while maxima will tend to appear to the north and south of the middle of the channel as time goes on. These results are illustrated in figures 5 and 6, where we, in figure 5, have computed the distribution of $u(y,t)$ for $t=0$, 2, 3, and 3.5 days from equation (3.19). Figure 5 was computed for non-divergent flow ($q=0$), $\beta=\beta_{45}$, a width of the channel equal to 6,000 km., and a zonal wavelength of 5,000 km. The initial maximum wind speed was 60 m. sec.$^{-1}$ and A_1 was chosen corresponding to an initial meridional wind of 5 m. sec.$^{-1}$, while $A_3=0$. Figure 5 should be compared with figure 6 where the parameters have the same values except that A_3 also corresponded to 5 m. sec.$^{-1}$ in the meridional wind component. The distribution of $\overline{u}(y,t)$ is only given for $t=0$, 0.5, 1, and 1.5 day in figure 6. It is seen that the presence of the waves on the smaller meridional scale, initially, causes the splitting of the jet stream into the two jet maxima to take place at a faster rate.

Figures 5 and 6 are very similar to those constructed by Thompson [15] from his theory of large-scale turbulence in barotropic flow as they, indeed, should be because the physical model is the same. The changes predicted in the zonal profile in our computation are however, due to the presence of unstable barotropic waves, while Thompson's theory is based upon the interaction between eddies and the mean flow expressed partly in quantities which can be derived from the mean flow and partly in certain statistical properties of the eddies. It will be noted also that the time scale of the changes in the mean zonal flow is the same in the two computations. It takes 2 to 3 days to develop two distinct maxima in the profile of the zonal wind from the single maximum present initially in the center of the channel.

From our calculation we may therefore conclude that if we have barotropic instability in a flow characterized by a single maximum in the zonal wind, it is a dynamical consequence caused by the convergence of the meridional transport of momentum by the eddies that the zonal profile will change to a profile with double maximum. This is done by momentum being transported away from the center of the channel in both directions by the eddies,

which in turn means that the unstable barotropic disturbances have a tilt of the trough and ridge lines, which goes from southeast toward northwest south of the center and from southwest toward northeast north of the center of the channel. This tilt is opposite to the one generally observed in the atmosphere. This fact points to the importance of barolinic processes in the real atmosphere, but the experiences in barotropic prediction show that processes similar to those described in the present paper definitely occur.

4. AN EXAMPLE OF BAROTROPIC DEVELOPMENT

Figure 7 shows a section of the 500-mb. analysis from May 15, 1961 at 1200 GMT. The interesting feature on this section of the hemispheric analysis is the fairly straight jet stream from the eastern part of Canada over Newfoundland toward the southeast over the Atlantic Ocean. Notice in particular that the isotherms are almost parallel to the contours over a large section of the jet stream. The isotachs for the map (not reproduced) show a maximum of about 30 m. sec.$^{-1}$ over Newfoundland with a drop to less than 10 m. sec.$^{-1}$ on both sides in a distance of about 1,000 km.

Figures 8, 9, and 10 show analyses for May 16, 17, and 18 also for 1200 GMT. Between May 15 and 16 a development took place along the jet stream over Newfoundland. The center of the circulation was located approximately at 45° N., 35° W. on May 16, 1200 GMT. Notice again on figure 8 that we find no regions of strong temperature advection. During the following day the number of closed contours around the center increased, while the Low drifted slowly toward the southeast with a position at 43° N., 30° W. on May 17, 1200 GMT. The Low remained almost stationary during the next 24-hour period with a slight tendency toward filling.

The forecasts made with the 500-mb. operational model from the initial data at May 15, 1961 at 1200 GMT are shown in figures 11, 12, and 13. The 24-hour forecast (fig. 11) shows that the barotropic model forecasted the development of a closed circulation. The center located at approximately 50° N., 35° W., is too far to the north. However, the barotropic development continued in the forecast between 24 and 48 hours and the circulation is centered at 45° N., 29° W. in the 48-hour forecast. The 72-hour forecast shows a further increase in the number of closed contours, but the center has now moved too far toward the east.

The initial jet stream has been divided into two branches on the observed maps and on the forecasts. Toward the end of the period we find a rather broad current over the eastern part of North America. This current divides into two branches, one going toward the northeast over the southern part of Greenland, the other bending toward the southeast and continuing on the southern side of the Low, which was developed in the Atlantic.

The development of the flow pattern in the example shows therefore a great similarity to those predicted by the linear theory. This type of barotropic development is observed frequently in barotropic forecasting and results usually in cold, cut-off cyclones. However, it is not the

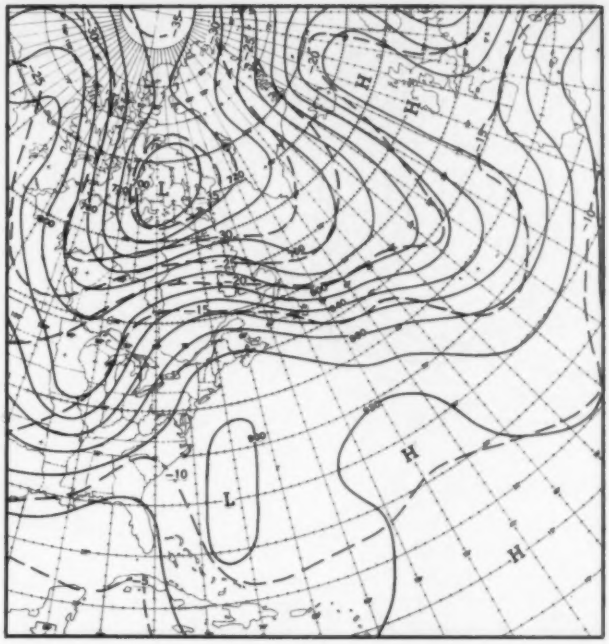

FIGURE 7.—500-mb. analysis for May 15, 1961, 1200 GMT. Solid lines are contours and dashed lines isotherms.

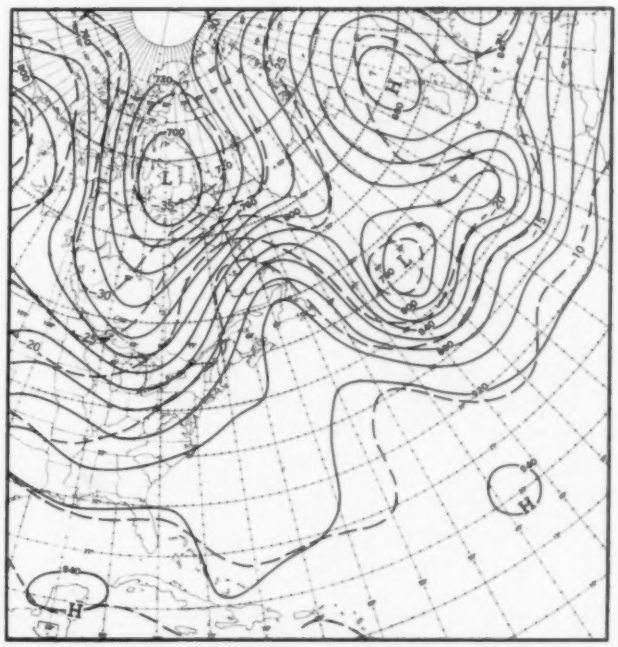

FIGURE 8.—500-mb. analysis for May 16, 1961, 1200 GMT.

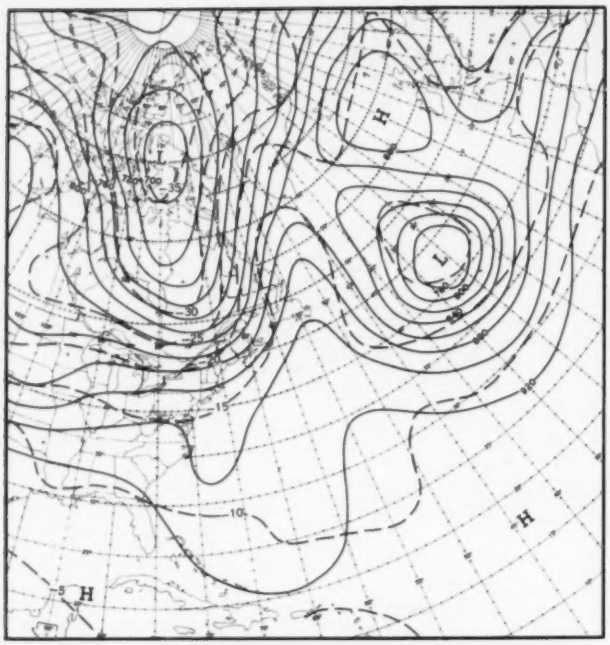

FIGURE 9.—500-mb. analysis for May 17, 1961, 1200 GMT.

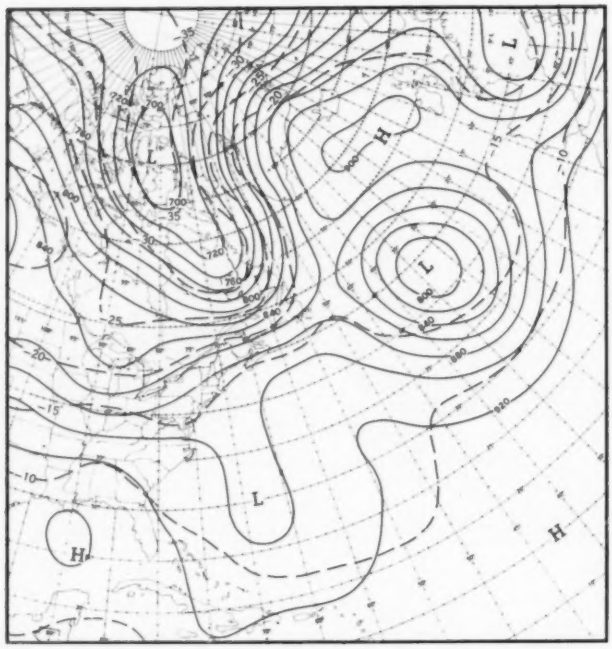

FIGURE 10.—500-mb. analysis for May 18, 1961, 1200 GMT.

most frequent type of development in the troposphere. The baroclinic developments associated with well developed divergence fields are the more common.

It is interesting to note that Murray [11] in a recent investigation of baroclinic stability of stratospheric flow,

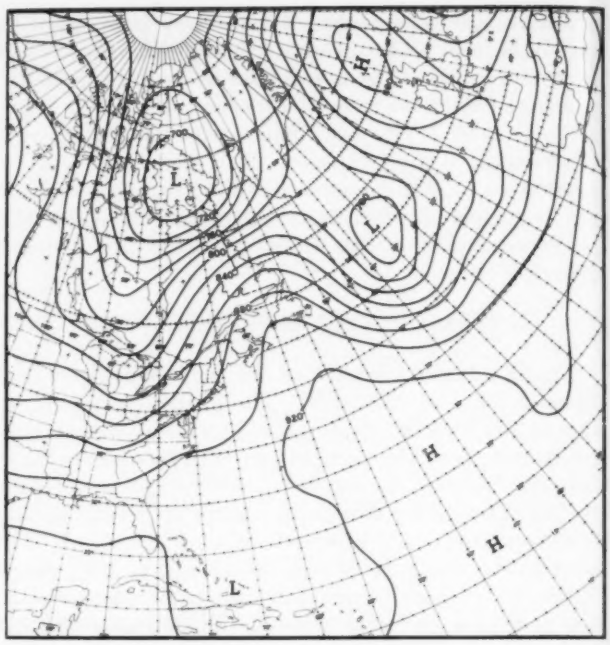

FIGURE 11.—24-hour one-parameter forecast starting from May 15, 1961, 1200 GMT.

especially the breakdown of the polar night jet located close to the 25-mb. surface, indicates that the polar night jet is baroclinically and inertially stable. He suggests, therefore, that barotropic instability of the type discussed here is responsible for the breakdown of the polar night jet. This result is contradicted by the conclusions reached by Boville [2] who states that "baroclinic wave development, fulfilling instability criteria and energy conversions of the Fleagle type appear to have been identified down to wave number four." The difference in the results of the two (independent) studies can probably be ascribed to the different models which were adopted, but it is beyond the scope of this paper to resolve the question of the stability of the polar night jet.

5. ENERGY CONVERSIONS

We shall next turn our attention to the energy conversion between mean zonal kinetic energy and eddy kinetic energy, the only energy conversion which is possible in the model, if $q=0$; i.e., no divergence. The prediction equation is in this case

$$\partial\zeta/\partial t+\mathbf{V}\cdot\nabla\zeta+\beta v=0. \tag{5.1}$$

When we divide each quantity into its zonal mean value and deviation from the zonal mean value and introduce these expressions into (5.1) we obtain the following equation for the average flow:

$$\partial\bar{\zeta}/\partial t+\overline{\mathbf{V}'\cdot\nabla\zeta'}=0 \tag{5.2}$$

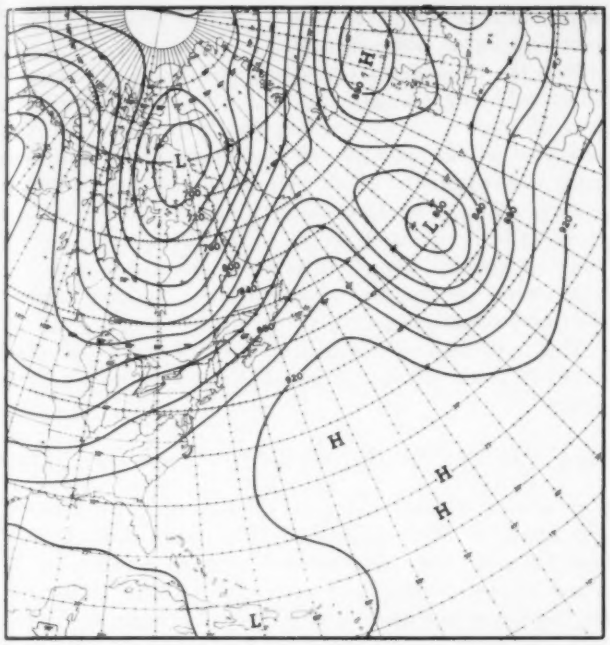

FIGURE 12.—48-hour one-parameter forecast starting from May 15, 1961, 1200 GMT.

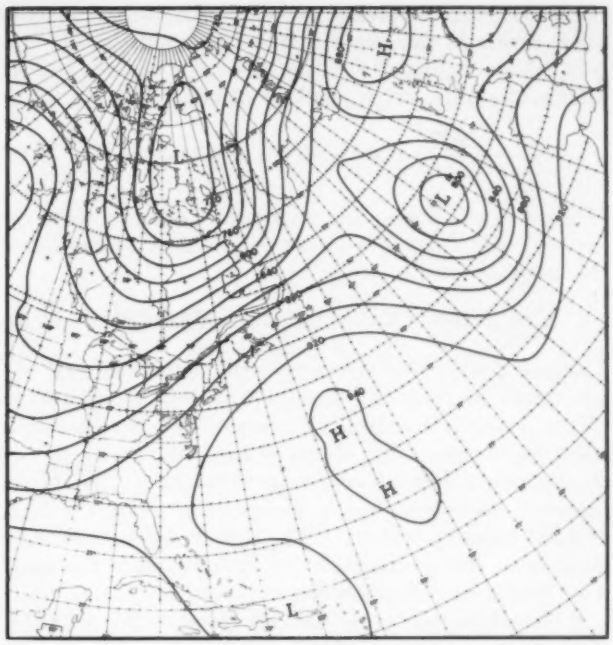

FIGURE 13.—72-hour one-parameter forecast starting from May 15, 1961, 1200 GMT.

This equation may also be written in the form:

$$\partial\bar{\zeta}/\partial t=\partial^2(\overline{u'v'})/\partial y^2 \tag{5.3}$$

because

$$\overline{\mathbf{V}'\cdot\nabla\zeta'}=\nabla\cdot(\overline{\zeta'\mathbf{V}'})=\frac{\partial}{\partial y}(\overline{\zeta'v'})=-\frac{\partial}{\partial y}\left(\overline{v'\frac{\partial u'}{\partial y}}\right) \tag{5.4}$$

but due to the non-divergence of the eddy-flow; i.e.,

$$\frac{\partial u'}{\partial x}+\frac{\partial v'}{\partial y}=0 \tag{5.5}$$

we obtain

$$-\frac{\partial}{\partial y}\left(\overline{v'\frac{\partial u'}{\partial y}}\right)=-\frac{\partial^2\overline{u'v'}}{\partial y^2}+\frac{\partial}{\partial y}\left(\overline{u'\frac{\partial v'}{\partial y}}\right). \tag{5.6}$$

The last term is, however, zero, because

$$\frac{\partial}{\partial y}\left(\overline{u'\frac{\partial v'}{\partial y}}\right)=-\frac{\partial}{\partial y}\left(\overline{u'\frac{\partial u'}{\partial x}}\right)=0. \tag{5.7}$$

The mean kinetic energy per unit mass and unit area may in this model be written in the form:

$$\bar{K}=\frac{1}{S}\int_s\frac{1}{2}\bar{u}^2dS=\frac{1}{2D}\int_0^D\left(\frac{\partial\bar{\psi}}{\partial y}\right)^2dy \tag{5.8}$$

from which it follows that

$$\frac{d\bar{K}}{dt}=\frac{1}{D}\int_0^D\frac{\partial\bar{\psi}}{\partial y}\frac{\partial}{\partial y}\left(\frac{\partial\bar{\psi}}{\partial t}\right)dy=-\frac{1}{D}\int_0^D\bar{\psi}\frac{\partial\bar{\zeta}}{\partial t}dy, \tag{5.9}$$

because $\partial^2\bar{\psi}/\partial y\partial t=-\partial\bar{u}/\partial t=0$ at both boundaries at all times. It is seen from (5.9) that we obtain the change in kinetic energy by multiplying (5.3) by $\bar{\psi}$ and then integrating over the width of the channel. This procedure leads to

$$\frac{d\bar{K}}{dt}=-\frac{1}{D}\int_0^D\bar{\psi}\frac{\partial^2\overline{u'v'}}{\partial y^2}dy=-\frac{1}{D}\int_0^D\bar{u}\frac{\partial\overline{u'v'}}{\partial y}dy. \tag{5.10}$$

The change in time of the eddy kinetic energy may be found from a similar method which results in

$$\frac{dK'}{dt}=\frac{1}{D}\int_0^D\bar{u}\frac{\partial\overline{u'v'}}{\partial y}dy. \tag{5.11}$$

It is then natural to define the following expression as the energy conversion between eddy kinetic energy and mean kinetic energy:

$$\{K'\cdot\bar{K}\}=-\frac{1}{D}\int_0^D\bar{u}\frac{\partial\overline{u'v'}}{\partial y}dy. \tag{5.12}$$

The general expression for energy conversion in isobaric, non-divergent flow shows that if the zonal wind is positively correlated with the convergence of momentum transport there is a conversion from eddy kinetic energy to the mean flow kinetic energy, while negative correlations between the two quantities give the opposite conversion.

The energy conversion (5.12) will now be evaluated for

the amplifying barotropic wave according to the analysis made earlier in this paper. Restricting ourselves to this part of the solution we find that the convergence of momentum transport is given by (3.14)

$$-\frac{\partial \overline{u'v'}}{\partial y}=2\mu\lambda^2(X_1Z_2-X_2Z_1)e^{2\mu St}\cdot M(y). \qquad (5.13)$$

When we substitute this expression together with the expression (2.9) for $\overline{u}$ in (5.12) we find after evaluation of the integral

$$\{K'\cdot\overline{K}\}=\mu\lambda^2Be^{2\mu St}(X_1Z_2-X_2Z_1)=-\mu\lambda^2Be^{2\mu St}N^*. \qquad (5.14)$$

The last expression gives us the sign of the quantity N^* which was introduced in (3.16). The eddy kinetic energy of the unstable barotropic wave can only increase as a result of the conversion of energy from the kinetic energy of the mean flow. The energy conversion $\{K'\cdot\overline{K}\}$ is therefore negative, which means that $N^*=-(X_1Z_2-X_2Z_1)$ must be positive. The sign of N^* was of vital importance for the discussion of the changes in the zonal wind profile carried out earlier in the paper.

It should be noted that the expression (5.14), on which we have based the conclusion that N^* is positive, is evaluated without regard to the second-order changes in the zonal momentum. The expression (5.14), applies therefore only for a short interval of time initially, a fact which does not destroy the argument. The importance of the higher-order changes in the energy conversion and the question of when the non-linear effects become significant will be investigated at the end of section 6.

It is obvious that the linearized treatment of the barotropic problem can describe the development of the profile of the zonal wind and perturbations only up to the time when there is considerable interaction between the two parts of the motion. This is seen directly in the expressions which we have derived for the change in the zonal wind (3.18) and the energy conversion (5.14) which will predict changes which tend toward infinity with increasing time.

From energy considerations it is equally obvious that the source of energy for the perturbation, i.e., the zonal available kinetic energy, is finite, and that the growth of the pertubation therefore must stop after a while, and the energy conversion must change sign. The non-linear interactions which are necessary for such processes can only be incorporated by integrating a more complete form of the prediction equation. Lorenz [9] has recently shown a simplification of the non-linear vorticity which enables us to retain the non-linear interaction by restricting the fields to a few wave components. An integration of this type will be described in the next section.

6. EXTENDED TIME INTEGRATIONS OF BAROTROPIC FLOW

The extended time integration of the barotropic equation was carried out for two reasons. It was desirable to investigate the validity of the results obtained from the linear analysis, and the changes in the zonal profile, the momentum transport, and the energy conversions could be investigated as a function of time in a more general case. The integration can be considered as an extension of Lorenz's [9] original integration, which was made with equations which were simplified to a maximum extent. Guided by the results which we have obtained during the linear analysis we shall formulate a system which is general enough to allow double maxima in the zonal wind profile, but simple enough to give a very efficient computation.

The form of the expression for the mean zonal wind (3.19) in the linear case suggests that an expression of the form:

$$\overline{u}(y,t)=B(t)+C(t)-B(t)\cos(2\lambda y)-C(t)\cos 4\lambda y \qquad (6.1)$$

may be used with advantage in the numerical experiment. The family of curves described by (6.1) for different values of B and C can vary between strong westerlies in the center of the channel with easterlies near the walls and, on the other extreme, strong westerlies near the walls with easterlies in the center of the channel. The predicted values of B and C from given initial values will therefore show the changes in certain types of zonal wind profiles predicted from the barotropic equations. The stream function corresponding to the mean zonal wind (6.1) is:

$$\overline{\psi}(y,t)=D(B+C)\left[1-\frac{y}{D}\right]+\frac{B}{2\lambda}\sin(2\lambda y)+\frac{C}{4\lambda}\sin(4\lambda y) \qquad (6.2)$$

where D is the width of the channel and the constant of integration has been determined in such a way that $\overline{\psi}(D,t)=0$.

The solution (3.13) for the perturbation stream function suggests, on the other hand, a prescribed expression for this quantity of the following form:

$$\psi'(x,y,t)=\frac{E_1(t)}{k}\sin\lambda y\sin kx+\frac{E_3(t)}{k}\sin 3\lambda y\sin kx+\frac{F_1(t)}{k}\sin\lambda y\cos kx+\frac{F_3(t)}{k}\sin 3\lambda y\cos kx \qquad (6.3)$$

which allows one wave number (k) in the zonal direction and two wave numbers (λ and 3λ) in the meridional direction. The complete stream function is then given by the expression

$$\psi(x,y,t)=\overline{\psi}(y,t)+\psi'(x,y,t) \qquad (6.4)$$

Now (6.4) can be substituted in the vorticity equation

$$\frac{\partial\nabla^2\psi}{\partial t}=J(\nabla^2\psi,\psi)-\beta\frac{\partial\psi}{\partial x} \qquad (6.5)$$

in which $\beta=df/dy$ is considered to be a constant, and we

can by the technique developed by Lorenz [9] transform (6.5) into six forecast equations for the six amplitudes: B, C, E_1, E_3, F_1, and F_3, which are functions of time only. With the notations:

$$Q=\frac{\lambda^2}{k^2},\quad R=\frac{\beta}{k^2} \tag{6.6}$$

the six forecast equations for the amplitudes are:

$$\left.\begin{aligned}
\frac{dB}{dt}&=2kQ[E_1F_3-E_3F_1]\\
\frac{dC}{dt}&=-2kQ[E_1F_3-E_3F_1]\\
\frac{dE_1}{dt}&=k\left[CF_1-\frac{Q-3}{2(Q+1)}BF_1-\frac{5Q+1}{2(Q+1)}BF_3-\frac{7Q-1}{2(Q+1)}CF_3-\frac{R}{Q+1}F_1\right]\\
\frac{dE_3}{dt}&=k\left[(B+C)F_3+\frac{3Q-1}{2(9Q+1)}BF_1-\frac{15Q-1}{2(9Q+1)}CF_1-\frac{R}{9Q+1}F_3\right]\\
\frac{dF_1}{dt}&=-k\left[CE_1-\frac{Q-3}{2(Q+1)}BE_1-\frac{5Q+1}{2(Q+1)}BE_3-\frac{7Q-1}{2(Q+1)}CE_3-\frac{R}{Q+1}E_1\right]\\
\frac{dF_3}{dt}&=-k\left[(B+C)E_3+\frac{3Q-1}{2(9Q+1)}BE_1-\frac{15Q-1}{2(9Q+1)}CE_1-\frac{R}{9Q+1}E_3\right].
\end{aligned}\right\} \tag{6.7}$$

We notice from the first two expressions in (6.7) that

$$B+C=M_0=\text{const.} \tag{6.8}$$

This result could have been derived a priori because it simply expresses the fact that total zonal momentum of the system is conserved.

It has been shown by Lorenz [9] that the simplified barotropic equations (6.7) conserve the kinetic energy and the square of the vorticity when these quantities are integrated over the region. It should be noted that the kinetic energy and the square of the vorticity are evaluated as the sum of the contributions from the components which are included in the forecasts.

The kinetic energy per unit area is in our case evaluated from the expression.

$$K=\frac{1}{LD}\int_0^L\int_0^D\frac{1}{2}\nabla\psi\cdot\nabla\psi\,dx\,dy=-\frac{1}{2}\cdot\frac{1}{LD}\int_0^L\int_0^D\psi\nabla^2\psi\,dx\,dy. \tag{6.9}$$

We introduce the expressions (6.4), (6.3), and (6.2) in (6.9) and obtain after evaluation of the integrals

$$K=\frac{1}{2}(B+C)^2+\frac{1}{4}(B^2+C^2)+\frac{1}{8}\frac{\lambda^2+K^2}{K^2}(E_1^2+F_1^2)+\frac{1}{8}\frac{9\lambda^2+K^2}{K^2}(E_3^2+F_3^2). \tag{6.10}$$

A direct proof that the kinetic energy is conserved can be obtained by differentiating (6.10) with respect to time and substituting from the system (6.7). This computation was carried out as a check on the derivation of the system (6.7)

Let us further define the mean square of the vorticity by the formula

$$V=\frac{1}{LD}\int_0^L\int_0^D(\nabla^2\psi)^2dx\,dy. \tag{6.11}$$

Substituting again from (6.4) in (6.11) we obtain the following expression for V:

$$V=2\lambda^2B^2+8\lambda^2C^2+\frac{1}{4}\frac{(\lambda^2+k^2)^2}{k^2}(E_1^2+F_1^2)+\frac{1}{4}\frac{(9\lambda^2+k^2)^2}{k^2}(E_3^2+F_3^2). \tag{6.12}$$

Again we can of course obtain a direct proof that V as expressed in (6.12) is indeed conserved. The two conserved quantities, K and V, can be computed in each time step during a numerical integration of the system (6.7). If they are conserved during the integration, or at least show no trend for systematic increase, decrease, or violent fluctuations, we have a good check on the behavior of the numerical integration especially with respect to truncation errors. Such a check was introduced in the numerical integration to be described later in this section.

It is one of the purposes of the numerical integration to investigate the energy conversion between mean kinetic energy and eddy kinetic energy during an extended period of integration. We need therefore to evaluate the formula for this energy conversion in our simplified model. This is

accomplished by a substitution of (6.4) in (5.12) from which we obtain

$$\{K' \cdot \overline{K}\} = \frac{\lambda^2}{k} (B-C) \cdot (E_1 F_3 - E_3 F_1). \tag{6.13}$$

The energy conversion (6.13) was computed in each time step during the numerical integration.

We shall next return to the fact that the total momentum of the fluid is conserved as shown in (6.8). This conservative property puts a constraint on the amount of zonal kinetic energy which can be released to the perturbations, as shown by Platzman and Baer [13]. We may, in other words, consider the total zonal kinetic energy as composed of two parts: the available zonal kinetic energy and the unavailable energy. It is easy to evaluate the two quantities in the simple model used in our experiments. The zonal part of the kinetic energy is, as can be seen from (6.10),

$$E_z = \frac{1}{2} (B+C)^2 + \frac{1}{4} (B^2+C^2). \tag{6.14}$$

We can combine (6.14) with (6.8) and rewrite (6.14) in the form:

$$E_z = \frac{3}{4} M_0^2 + \frac{1}{2} B(B-M_0) \tag{6.15}$$

from which it is seen that

$$\delta E_z = \left(B - \frac{1}{2} M_0\right) \delta B. \tag{6.16}$$

E_z is therefore at a minimum if $B = \frac{1}{2} M_0$ in which case we also have $C = \frac{1}{2} M_0$. In our case there exists therefore a particular profile of the zonal wind, described by (6.1), for which the zonal kinetic energy is at a minimum, namely the one for which $B=C$. The minimum value of the zonal kinetic energy is evaluated from (6.14) with $B=C=\frac{1}{2} M_0$ and is

$$E_{z,\,min.} = \frac{5}{8} M_0^2. \tag{6.17}$$

This is the unavailable part of the zonal kinetic energy. Only 3/8 of the initial momentum squared is therefore available for conversion to eddy kinetic energy. Subtracting (6.17) from (6.15) we can evaluate the available zonal kinetic energy. It becomes

$$E_{z,\,av.} = \frac{1}{8} M_0^2 - \frac{1}{2} BC = \frac{1}{8} (B-C)^2. \tag{6.18}$$

We notice here that if $B=C=\frac{1}{2} M_0$ we get no available, zonal, kinetic energy. It should further be mentioned that very large values of zonal, available energy are obtained in the case that $M_0=0$, which means that $B=-C$, in which case $E_{z,\,av.} = \frac{1}{2} B^2$. We shall illustrate later by the results of the actual calculations that very large changes in the zonal flow take place in this case.

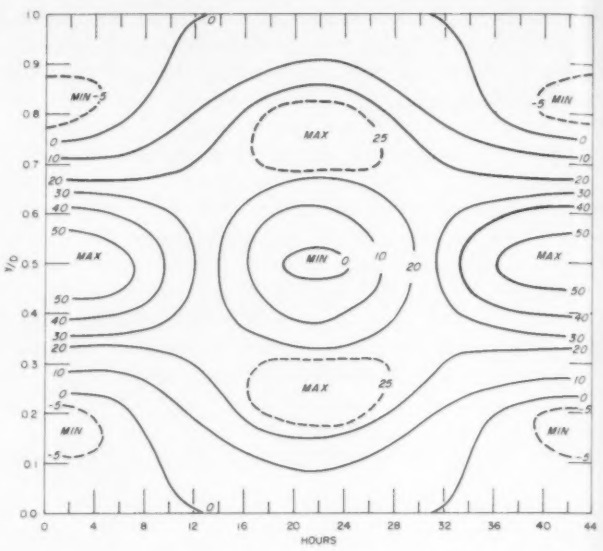

FIGURE 14.—Case 1. The zonal velocity as a function of time and meridional distance over one period. Initial parameters: $B_0=30$ m. sec.$^{-1}$, $C_0=-15$ m. sec.$^{-1}$, $E_{10}=25$ m. sec.$^{-1}$, $E_{40}=F_{10}=F_{20}=0$, $\beta=\beta_{45}$, width 3,000 km., zonal wavelength 5,000 km.

Numerical integrations of the system (6.7) have been carried out in a number of cases. In the following we shall describe some of the more interesting results. The integration was performed using central finite differences in time except initially, where one uncentered step was taken. The time step has been 1 hour in all the calculations. We shall treat four different cases. The calculations were in all cases carried out to 24 days (576 time steps), but since all the computations turned out to be periodical we shall usually illustrate only a shorter time period. The finite difference system in time was tested by computing the kinetic energy per unit area and the square of the vorticity per unit area. These quantities showed only small fluctuations during the complete integration, indicating that the finite difference system used in these calculations is good enough even for extended integrations with the present system. A short description of the results of four integrations follows.

Case 1: As the first example we have selected a case where the initial flow pattern is barotropically unstable. The zonal wavelength was taken to be 5,000 km. and the width of the channel 3,000 km., corresponding to a maximum meridional wavelength of 6,000 km. The quantities B and C were selected initially at 30 m. sec.$^{-1}$ and -15 m. sec.$^{-1}$, respectively, giving a zonal wind profile with a single maximum in the center of the channel of 60 m. sec.$^{-1}$ The profile has also weak easterlies close to the walls with a maximum easterly wind of about 7 m. sec.$^{-1}$ The initial disturbance was defined by putting $E_1=25$ m. sec.$^{-1}$,

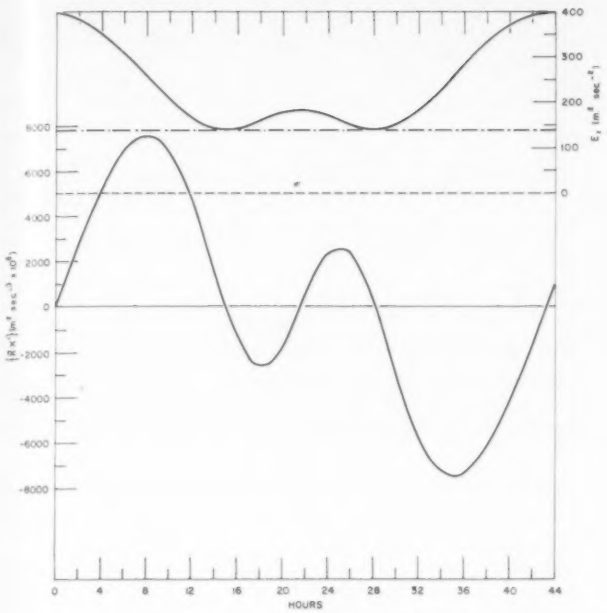

FIGURE 15.—Case 1. The zonal kinetic energy as a function of time over one period (upper curve, right scale). The energy conversion between zonal and eddy kinetic energy as a function of time over one period (lower curve, left scale).

while $E_3=F_1=F_3=0$ initially. The disturbance defined by these values has a south-north direction of the trough and ridge lines and has, therefore, initially no transport of momentum.

The changes which take place in the zonal winds during the forecast are illustrated in figure 14, where the zonal wind profile is shown as a function of time in hours. The forecast turns out to be periodic with a period close to 44 hours. We have therefore only shown one period. The initial maximum in the zonal wind in the center of the channel breaks down and is after about 22 hours replaced by weak easterlies of 2–3 m. sec.$^{-1}$ At the same time two maxima of westerly zonal winds form to the north and the south of the center of the channel with speeds of 28–29 m. sec.$^{-1}$ After 44 hours we are back to the initial zonal wind profile. The forecast predicts therefore an oscillation in the zonal wind profile varying between a single and a double maximum in the jet stream.

The processes which determine this oscillation are described in figure 15, in which the lower curve shows the energy conversion between zonal kinetic energy and eddy kinetic energy. During the first hours of the forecast the energy is converted from the zonal flow to the eddies. This conversion reaches a maximum after about 8 hours, but remains positive up to about 15 hours, when the sign of the conversion changes for a few hours and becomes zero shortly before 22 hours. The upper curve shows the variation with respect to time of the kinetic energy contained in the zonal flow. In agreement with the energy conversion curve we find a decrease in the zonal kinetic energy up to 15 hours, when it increases slightly, and then a decrease again before it finally starts to increase to complete the cycle after 44 hours.

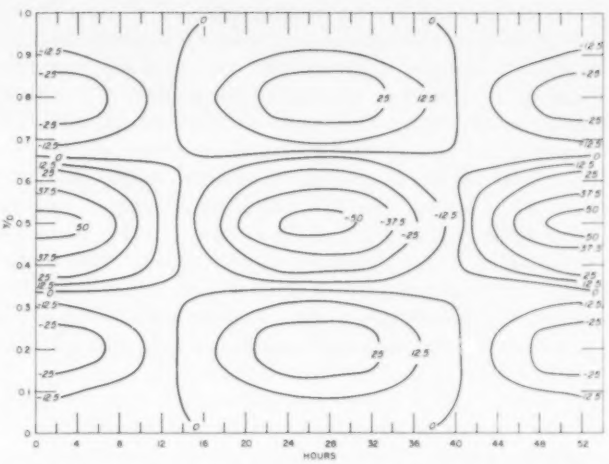

FIGURE 16.—Case 2. Zonal velocity as a function of time and meridional distance over one period. Parameters as in case 1 (fig. 14) except $C_0=30$ m. sec.$^{-1}$.

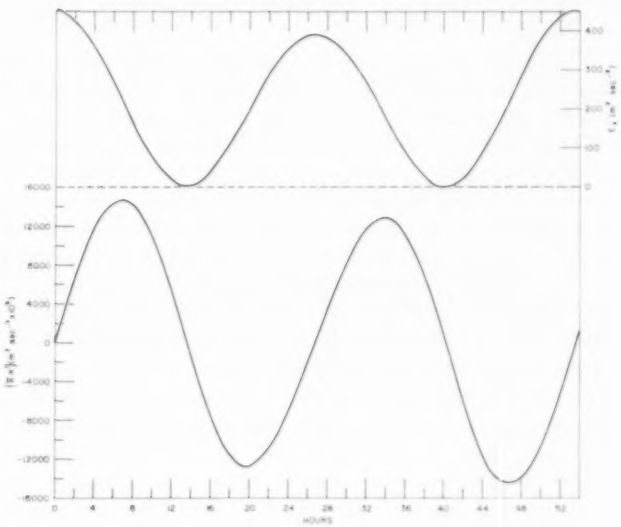

FIGURE 17.—Case 2. Zonal kinetic energy as a function of time over one period (upper curve, right scale). The energy conversion between zonal and eddy kinetic energy as a function of time over one period (lower curve, left scale).

We can compute the amount of unavailable zonal kinetic energy from the formula (6.17). With $B_0=30$ m.sec.$^{-1}$ and $C_0=-15$ m.sec.$^{-1}$ we find $M_0=15$ m. sec.$^{-1}$ The minimum zonal kinetic energy is therefore $E_{z,min}=140.6$ m.^{2} sec.$^{-2}$ It is interesting to note that this is equal to the actual minimum on the curve for E_z, indicating that all the available kinetic energy in the zonal flow actually is being released to the perturbations. It also indicates that very large amounts of kinetic energy

may be released to the perturbations if we specify the initial zonal wind profile in such a way that the momentum is small. In order to test this we computed a second case. *Case 2:* In this case we have chosen $B=-C=30$ m. sec.$^{-1}$, which makes the zonal momentum $M_0=0$. The unavailable kinetic energy vanishes therefore in this case, and the total amount of kinetic energy is at the same time larger. In this admittedly extreme case we have again a maximum of 60 m. sec.$^{-1}$ in the center of the channel in the initial, zonal wind profile with easterlies to the north and south of 33 m. sec.$^{-1}$ (fig. 16). The period in the forecasts turns out to be about 54 hours in this case. Very violent fluctuations take place in the zonal winds at the different latitudes in this case. In the middle of the period we find easterlies in the center of the channel of 55 m.sec.$^{-1}$, while the westerlies in the northern and southern portions, at the same time, have increased in strength to more than 30 m.sec.$^{-1}$ It can be seen on figure 16 that the forecast passes through a state between 13 and 14 hours in which there is no zonal wind, a situation which is found again between 40 and 41 hours.

Figure 17 (corresponding to fig. 15 in case 1) shows the time variation of the zonal kinetic energy and the energy conversion between zonal and eddy kinetic energy. We find as expected that the zonal kinetic energy decreases to zero between 13 and 14 hours and again between 40 and 41 hours. The energy conversion is naturally zero at the same time after having been positive, since all the kinetic energy has been converted to eddy kinetic energy. The secondary maximum in the zonal kinetic energy in the middle of the period where the energy conversion again is zero corresponds to the maximum intensity of the double jet stream seen in figure 16 at 27 hours.

Case 3: The initial zonal wind profile for this case was similar to case 1 in the sense that B and C initially had the same values ($B_0=30$ m.sec.$^{-1}$, $C_0=-15$ m.sec.$^{-1}$), but the dimensions of the region were increased. The width of the channel was taken to be 10,000 km., equal to the distance between pole and equator on the earth. The wavelength in the zonal direction was also taken to be 10,000 km., making the initial flow stable according to the linear theory (see figs. 2 and 3). The initial perturbation was again prescribed by setting $E_1=25$ m.sec.$^{-1}$ initially, while all the other amplitudes were zero initially.

Some results from this forecast are shown in figures 18 and 19. The first (fig. 18) shows a record of the strength of the zonal wind in the center of the channel and at a distance $0.2D$ from the wall. The zonal wind in the center shows a regular variation between 60 m.sec.$^{-1}$ and 32.5 m.sec.$^{-1}$ with a period of slightly more than 6 days, while the variation closer to the wall is between -6 m.sec.$^{-1}$ and $+9$ m.sec.$^{-1}$ with the same period. We find again a tendency to divide the initial single jet maximum into two maxima, because the westerly wind close to the wall is at a maximum at the same time as the zonal wind

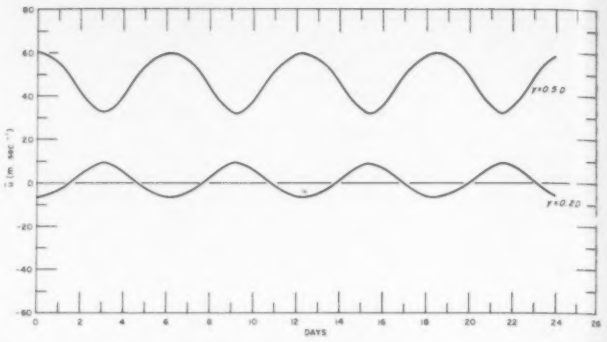

FIGURE 18.—Case 3. The zonal velocity in the center of the channel and at a distance of 0.2 D from the wall as a function of time. Parameters $B_0=30$ m. sec.$^{-1}$, $C_0=15$ m. sec.$^{-1}$, $E_{10}=F_{10}=F_{20}=0$, $\beta=\beta_{45}$, width 10,000 km., zonal wavelength 10,000 km.

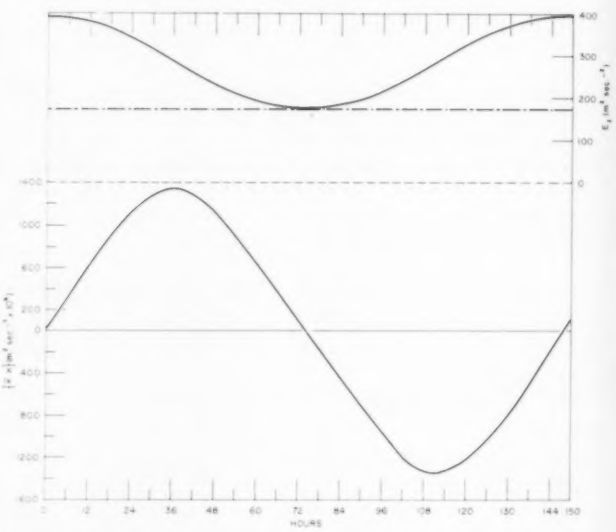

FIGURE 19.—Case 3. The zonal kinetic energy as a function of time over one period (upper curve, right scale). The energy conversion between zonal and eddy kinetic energy as a function of time over one period (lower curve, left scale).

is at a minimum in the center of the channel. The energy conversion between zonal and eddy kinetic energy is plotted in figure 19 as a function of time together with the time variation of the zonal kinetic energy itself over one period (about 148 hours). The two curves have this time a very regular variation, where the zonal kinetic energy goes to a minimum equal to the value estimated from equation (6.17) in the middle of the period.

Case 4: The initial specifications for this case were $B_0=30$ m.sec.$^{-1}$, $C_0=-30$ m.sec.$^{-1}$, the width of the channel 10,000 km., and the zonal wavelength 10,000 km. We have therefore again chosen a situation where the total zonal momentum vanishes. The variation of the zonal wind in the center of the channel and at a distance of $0.2D$ from the wall is shown in figure 20 as a function of time over a 24-day period. The zonal wind in the center

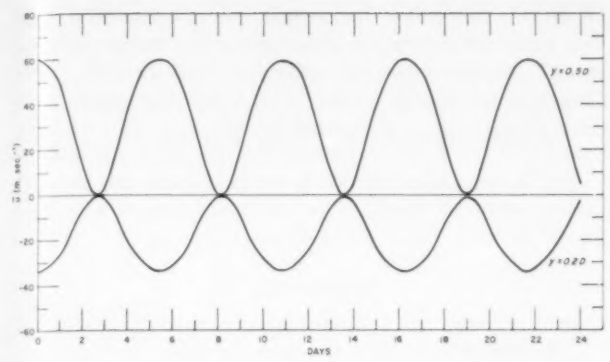

FIGURE 20.—Case 4. The zonal velocity in the center of the channel and at a distance of 0.2 D from the wall as a function of time. Parameters as in case 3 (fig. 18) except $C_s = -30$ m. sec.$^{-1}$.

varies between 60 m.sec.$^{-1}$ and 0 m.sec.$^{-1}$ with a period of 5½ days, while the zonal wind at 0.2D varies between −33 m.sec.$^{-1}$ and 0 m.sec.$^{-1}$. Notice, that no zonal wind exists at 2¾ days and at intervals of 5½ days thereafter. This picture is consistent with the curves in figure 21 where we notice that the kinetic energy of the zonal flow goes to zero in the middle of the period.

The characteristic period of 5–6 days which has been found in these integrations agrees with the typical time scale found by Thompson [15] in his theory of long-period variations in barotropic flow. A further agreement is found between the results obtained here and those reported by Charney [4] from a single extended integration of the barotropic vorticity equation and by Baer [1].

Some support is also found in analysis of atmospheric data for periodicities of this order of magnitude. Reference is made to the observational studies by Mintz and Kao [10] who found a period of 3–5 days in the convergence of the meridional transport of momentum at certain latitudes during January 1949. The study by Duggan [6] of the meridional convergence of momentum also shows periodicities of this order of magnitude.

The results of the non-linear integrations can be used to obtain information about how soon the higher-order effects become important. One may, for example, obtain this information from curves giving the energy conversion from zonal kinetic energy to eddy kinetic energy as a function of time in the non-linear computation and estimated from the linear theory including terms of different orders.

Substituting the expression (3.19) for $\overline{u}\,(y,t)$ and (3.18) for $-\partial\,(\overline{u'v'})/\partial y$ in the formula (5.12) for the energy conversion we find first that

$$\{\overline{K}\cdot K'\} = 4\mu\lambda^2 N^* \sinh(2\mu St)\cdot\left[\frac{1}{D}\int_0^D \overline{u}(y,0)M(y)dy\right] - \frac{8\mu\lambda^4 N^{*2}}{S}(\cosh(2\mu St)-1)\sinh(2\mu St)\cdot\left[\frac{1}{D}\int_0^D M^2(y)dy\right]. \quad (6.19)$$

The first term on the right hand side of (6.19) gives the

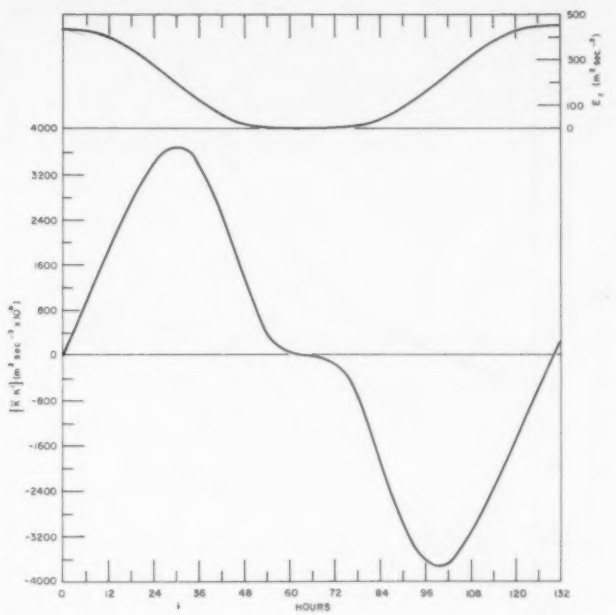

FIGURE 21.—Case 4. The zonal kinetic energy as a function of time over one period (upper curve, right scale). The energy conversion between zonal and eddy kinetic energy as a function of time over one period (lower curve, left scale).

contribution which depends upon the initial profile $u\,(y, 0)$, while the second term is independent of the initial profile. Since the meridional distribution of the convergence of momentum transport, expressed by the function $M(y)$, is a second-order effect, we may say that the first term in $\{\overline{K}\cdot K'\}$ is of second order, while the last term is a fourth-order effect.

When the expressions (2.9) for $\overline{u}\,(y, 0)$ and (3.15) for $M(y)$ are introduced in (6.19) we obtain after evaluation of the integrals

$$\{\overline{K}\cdot K'\} = 2\mu\lambda^2 N^* B \sinh(2\mu St) - \frac{8\mu\lambda^4 N^{*2}}{S}\sinh(2\mu St)\cdot(\cosh(2\mu St)-1). \quad (6.20)$$

The following case was selected for comparison. The zonal wavelength was chosen to be 5,000 km., the maximum meridional wavelength to be 6,000 km., $\beta = 16\times 10^{-12}$m.$^{-1}$sec.$^{-1}$, $B = 30$ m. sec.$^{-1}$, and $q^2 = 0$. The curve without marks in figure 22 gives the energy conversion in the non-linear computation as a function of time. The energy conversion increases to a maximum, which is reached after approximately 44 hours. The curve in figure 22 marked with circles is the energy conversion computed from (6.20) including, however, only the first term. By a comparison of the two curves we find that the curve including the second-order effects gives a good estimate of the energy conversion up to approximately 24 hours, although the estimate is slightly too high. When the fourth-order effects are included in the evaluation of (6.20),

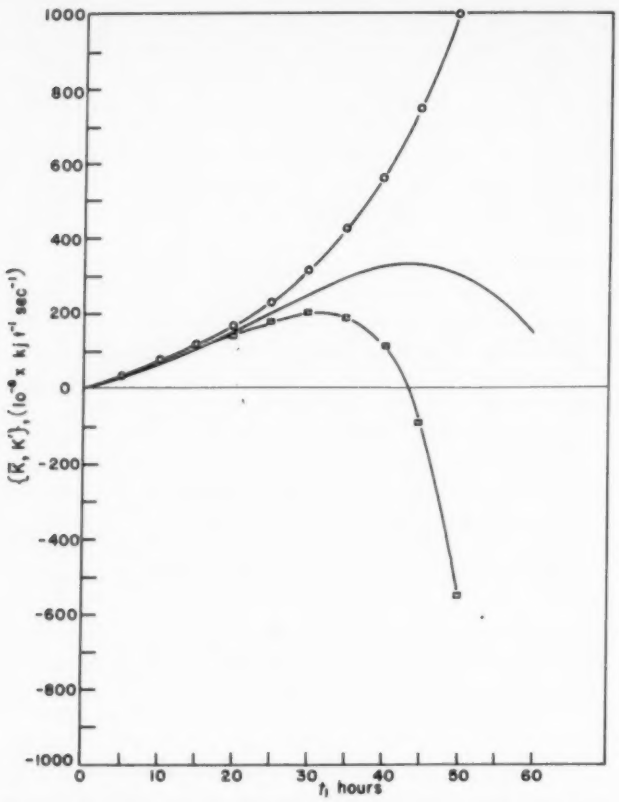

FIGURE 22.—The curve without marks gives the energy conversion as a function of time in a non-linear calculation with the following parameters: zonal wavelength 5,000 km., maximum meridional wavelength 6,000 km., $\beta = 16 \times 10^{-12}$ m.$^{-1}$ sec.$^{-1}$, $B = 30$ m. sec.$^{-1}$, and $q^2 = 0$. The curve marked with circles gives the energy conversion computed from the linear solution using the same parameters and including second-order effects, while the curve marked with squares also includes fourth-order effects.

we obtain the curve in figure 22 marked with squares. This curve gives a very good estimate for a little longer period than the second-order curve, but then rapidly shows an underestimate. The main result of the inclusion of the fourth-order term in (6.20) is, however, that this term actually predicts that the energy conversion will reach a maximum. The main conclusion from figure 22 is that the higher-order effects become important after about 1 day.

7. SUMMARY

The first sections of this paper contain a stability investigation of the divergent, one-parameter model. The main conclusion is that the introduction of a divergence term into the model tends to reduce the instabilities present in the non-divergent model. The second-order effects of the disturbances on the profile of the zonal wind are investigated. It is found that the unstable barotropic disturbances tend to cause a decrease of the zonal winds in the center of the channel and an increase of the mean zonal winds to the north and south.

A simple non-linear barotropic model containing only a few wave components is investigated in the next sections through integrations over extended time periods. The changes in the profile of the zonal wind, the energy conversion between kinetic energy of the mean flow and the eddies, and the time periodicities of the flow are investigated. Fluctuations of the order of 2 days are found in initially unstable flow, while the large-scale stable flow pattern shows periods of the order of 6 days.

REFERENCES

1. F. Baer, "The Extended Numerical Integration of a Simple Barotropic Model, Part II," *Technical Report* No. 3, National Science Foundation (NSF-G 2159), 1958.
2. B. W. Boville, "A Dynamical Study of the 1958–59 Stratospheric Polar Vortex," *Scientific Report* No. 9, McGill University, Contract No. AF19(604)-3865, 1961, 134 pp.
3. K. Bryan, "A Numerical Investigation of Certain Features of the General Circulation," *Tellus*, vol. 11, No. 2, May 1959, pp. 163–174.
4. J. Charney, "On the Theory of the General Circulation of the Atmosphere," pp. 178–193 of *The Atmosphere and the Sea in Motion*, Rossby Memorial Volume, Rockefeller Institute Press, New York, 1959.
5. G. P. Cressman, "Barotropic Divergence and Very Long Atmospheric Waves," *Monthly Weather Review*, vol. 86, No. 8, Aug. 1958, pp. 293–297.
6. F. F. Duggan, "A Study of the Meridional Convergence of Angular Momentum at 500 mbs. in Selected Latitude Belts," Thesis, U.S. Naval Postgraduate School, 1960. 16 pp.
7. E. Eliasen, "Numerical Solutions of the Perturbation Equation for Linear Flow," *Tellus*, vol. 6, No. 2, May 1954, pp. 183–192.
8. H. Kuo, "Dynamic Instability of Two-Dimensional Non-Divergent Flow in a Barotropic Atmosphere," *Journal of Meteorology*, vol. 6, No. 2, Apr. 1949, pp. 105–122.
9. E. N. Lorenz, "Maximum Simplification of the Dynamic Equations," *Tellus*, vol. 12, No. 3, Aug. 1960, pp. 243–254.
10. Y. Mintz and S-K. Kao, "A Zonal-Index Tendency Equation and Its Application to Forecasts of the Zonal Index," *Journal of Meteorology*, vol. 9, No. 2, Apr. 1952, pp. 87–92.
11. F. W. Murray, "Dynamic Stability in the Stratosphere," *Journal of Geophysical Research*, vol. 65, No. 10, Oct. 1960, pp. 3273–3305.
12. N. A. Phillips, "General Circulation of the Atmosphere: A Numerical Experiment," *Quarterly Journal of the Royal Meteorological Society*, vol. 82, No. 352, Apr. 1956, pp. 123–164.
13. G. W. Platzman and F. Baer, "The Extended Numerical Integration of a Simple Barotropic Model, Part I," *Technical Report*, No. 1, National Science Foundation (NSF-G 2159), 1958.
14. B. Saltzman, "Numerical Solution for an Idealized Barotropic Flow, Studies of the Atmospheric General Circulation III," *Final Report*, Massachusetts Institute of Technology, Contract No. AF19(604)-2242, 1959, pp. 132–147.
15. P. D. Thompson, "A Heuristic Theory of Large-Scale Turbulence and Long-Period Velocity Variations in Barotropic Flow," *Tellus*, vol. 9, No. 1, Feb. 1957, pp. 69–91.
16. W. Tollmien, "Über die Entstehung der Turbulenz, I," *Mitteilung, Nachrichten Gesellschaft Wissenschaften*, Göttingen (Neue Folge), vol. 1, 1929, pp. 20–44.
17. A. Wiin-Nielsen, "On Barotropic and Baroclinic Models, with Special Emphasis on Ultra-Long Waves," *Monthly Weather Review*, vol. 87, No. 5, May 1959, pp. 171–183.

THE NASHVILLE DAILY AIR POLLUTION FORECAST

CARL M. BOETTGER

U.S. Weather Bureau Research Station, R. A. Taft Sanitary Engineering Center, Cincinnati, Ohio

and

HAROLD J. SMITH

U.S. Weather Bureau Airport Station, Nashville, Tenn.

[Manuscript received February 9, 1961; revised July 3, 1961]

ABSTRACT

During the period of the Nashville Community Air Pollution Study, the Weather Bureau at Nashville, Tenn., forecasted air pollution to be one of three levels for the following day. The forecast method was most reliable during the winter season when pollution ranges were high. Discrimination of air pollution levels can undoubtedly be improved through experience and further studies, and the method is general enough to be used at other locales.

1. INTRODUCTION

An air pollution forecast was provided daily for the City of Nashville, Tenn., from January 23, 1959 to August 1, 1959. The forecasts, which were issued by the U.S. Weather Bureau at Nashville, were for high, low, and little or practically no pollution for the following day. The forecast method was intentionally made simple so that specialized experience would not be required by the forecasters and also took into account the type of routine forecasts which could be made. The criteria selected were to some extent based on past studies and experience of meteorologists at the Weather Bureau Research Station, Cincinnati, Ohio. This was probably the first time that a Weather Bureau Office made daily quantitative forecasts of air pollution levels.

2. METHOD

The forecast pollution level (i.e., high, low, little or none) was objectively determined from forecast values of a stability index and surface wind speed. Meteorologists at Berry Field, approximately 8 miles southeast of Nashville proper, could make these forecasts without prior knowledge or experience of air pollution meteorology. The low-level stability index was obtained by algebraically subtracting the forecast surface temperature for 0600 CST tomorrow from the forecast 900-mb. temperature for the same time. This index value, together with the forecast of weather the 0600 CST surface wind speed would be greater or less than 7 kt., was used to forecast the intensity of the air pollution as follows:

Forecast stability index (SI) and surface wind speed (WS) for 0600 CST	*Forecast air pollution level*
SI>0 and WS<7 kt	High pollution
SI<0 and WS<7 kt. or SI>0 and WS>7 kt.	Low pollution
SI<0 and WS>7 kt	Little or no pollution

The forecast was made at approximately 1500 CST and was valid for the next morning. Wind speeds were forecast using prognostic positions of pressure systems and prognostic pressure gradient. The 900-mb. temperature forecast was based on 850-mb. up-wind radiosonde observation information, and wind patterns and temperature advection as indicated on the 850-mb. chart. The latter was adjusted to the 900-mb. level, keeping in mind lifting or subsidence, as indicated. Surface temperatures were forecast using the 850-mb. temperature forecast and adjusting it to the surface with due allowance for forecast cloud cover or the lack of it, as an indication of radiational cooling and with allowance for wind speed as an indication of vertical mixing at low levels.

3. RESULTS

For each day, the air pollution at Nashville is described by each of the following:

A. Forecast Pollution Level, FPL:—The level of pollution forecast by the Weather Bureau at Nashville using the previously described method.

B. Pollution Level From the Observed Meteorological Criteria, PL(OC):—The stability index and wind speed which actually occurred determined this level in the same way that the forecast elements determined the FPL. In other words, the PL(OC) and the FPL would be identical if the meteorological elements were correctly forecast.

C. Measured Pollution Level, MPL:—In conjunction with the Nashville Community Air Pollution Study, there were 32 sampling stations uniformly spaced over the city from which continuous measurements of sulfur dioxide (pphm) and soiling index (Coh/1000 linear ft.) were available. Coh values determine by filter paper method, are an approximation of the soiling properties of the atmosphere. At seven of these stations, which were also uniformly spaced, more extensive sampling was done, and continuous 24-hour total particulate concentrations

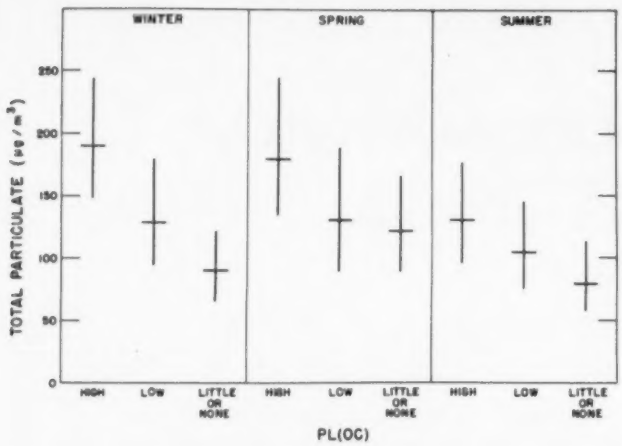

FIGURE 1.—Total particulate compared to pollution level indicated by observed meteorological criteria, PL(OC), separated by seasons and air quality group. Horizontal line is geometric mean, vertical line gives limits of one standard deviation.

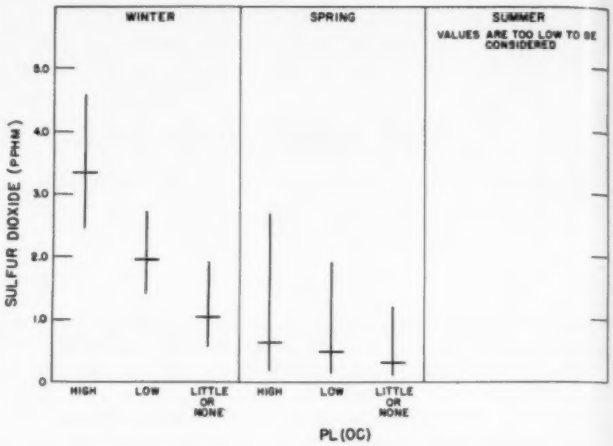

FIGURE 2.—SO_2 measurement compared to PL(OC), separated into seasons and air quality groups.

(μg./m.^{3}) were measured using high-volume air samplers. Daily means for each of the three air quality measurements were computed and used as a basis for determining the MPL's.

Comparisons of the three descriptions of "pollution level" were thus possible. A measure of ability to forecast the meteorological criteria was obtained by a comparison of the FPL and PL(OC) for each day a forecast was made. The effectiveness of the meteorological criteria for indicating pollution level was evaluated by a comparison of the PL(OC) and the MPL for each day. Finally, the FPL and the MPL were compared to determine the merit of the program. The results of the three comparisons are discussed in the following subsections.

EVALUATION OF FORECAST ABILITY: FPL VS. PL(OC)

Table 1, a contingency table of FPL vs. PL(OC), reveals that the forecasts were right more often than wrong with the exception of the "little or none" forecasts.

A statistical test (χ^2) indicates that such a distribution has less than 0.1 percent probability of occurring by chance. For the entire period 45 percent of the forecasts were meteorologically correct. If the period is divided into seasons (table 2), then 53 percent of the forecasts were correct in winter, 27 percent in the spring, and 53 percent in the summer. The low springtime figure probably reflects the erratic weather conditions during this season. For the purpose of the study, winter was presumed to be from January 23 to March 15, spring from March 16 to May 15, and summer from May 16 to August 1. These dates were primarily determined from heating degree days although an attempt was made to keep the number of days in each season somewhat equal.

TABLE 1.—*Frequency of forecast air quality level (FPL) classified according to the air quality level from the observed meteorological variables, PL(OC).*

FPL	PL(OC)			
	High	Low	Little or none	Total
High	21	14	2	37
Low	12	24	13	49
Little or none	2	21	7	30
Total	35	59	22	116

Calculated $\chi^2 = 23.3$
From tables χ^2 (.999) = 18.5

EVALUATION OF EFFECTIVENESS OF METEOROLOGICAL CRITERIA: PL(OC) VS. MPL

Because of differences in range and distribution of air quality data from one season to the next, comparisons were made season by season. Each group of air quality

TABLE 2.—*FPL vs. PL(OC) by seasons*

FPL	PL(OC)			Percent correct
	High	Low	Little or none	
	Winter			
High	10	1	1	82.4
Low	4	3	5	25.0
Little or none	0	3	3	50.0
Total				53.3
	Spring			
High	4	4	1	44.4
Low	5	3	7	20.0
Little or none	2	8	3	23.1
Total				27.0
	Summer			
High	7	9	0	43.8
Low	3	18	1	81.8
Little or none	0	10	1	9.6
Total				53.1

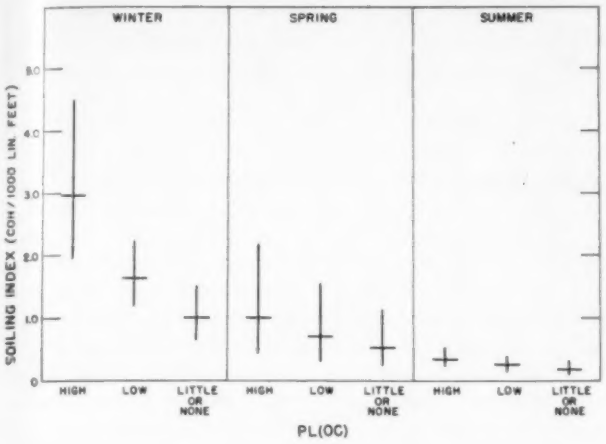

FIGURE 3.—Soiling index values compared to PL(OC), separated into seasons and air quality groups.

data was tested for normality of distribution by season, and it was found that all air quality data for all seasons were distributed in the logarithmic normal. For each season the three types of data, i.e., soiling index, sulfur dioxide, and total particulate, were separated according to the PL(OC), giving three different groups of data for each air quality parameter. The geometric means and standard geometric deviations from the groups thus obtained were plotted on linear graph paper. In figures 1, 2, and 3 the horizontal line is the geometric mean and the vertical line represents one standard geometric deviation on either side of the geometric mean (i.e., approximately 68 percent of the data are between these limits). Each parameter and season should be considered separately, but the one thing that all have in common is that the means are in the proper order. That is, the data selected on the days which were classified as high pollution according to the observed criteria had higher means than those of the low pollution days, and so on. The figures also indicate very definite seasonal differences which vary somewhat according to the type of measurement. Coh and SO_2 values are high with a wide range during the winter months, whereas the summer values are too low to be considered.

A statistical test, the analysis of variance method, was employed to determine if the means differed significantly. The test indicates very significant differences among the means during the winter season for all three air quality parameters. Apparently the method effectively divides the data into three levels during this season. The SO_2 values during the spring and summer seasons are generally too low to be considered. Total particulate as well as soiling index means during the spring season differ significantly, but an inspection of the figures reveals that good discrimination exists between only two levels. For the summer season there are significant differences among the total particulate means, but not as marked as during the winter season. Significant differences among the soiling index means are indicated, but the range of the data is low. To summarize the three figures, it appears that the criteria are valid indicators of three levels of total particulate, soiling index, and sulfur dioxide during the winter season. During the spring season the criteria significantly indicate two levels of total particulate and soiling index, while during the summer season they significantly indicate three levels of total particulate.

A different approach was also used to test the effectiveness of the meteorological criteria. The frequency distributions were divided into thirds, and each day's data were designated as being high, low, or little or none,

TABLE 3.—*PL(OC) vs. MPL by seasons*

PL(OC)	MPL											
	μg./m.^{3}				SO_2				Coh/1000 linear ft.			
	High	Low	Little or none	Percent correct	High	Low	Little or none	Percent correct	High	Low	Little or none	Percent correct
	Winter											
High	14	9	0	60.8	17	6	0	73.9	17	5	1	73.9
Low	3	5	3	45.4	1	7	3	63.6	0	8	3	72.7
Little or none	0	4	14	77.8	0	4	14	77.8	0	5	13	72.2
Total				63.5				73.1				73.1
	Spring											
High	11	6	2	57.9	8	8	3	42.1	9	6	4	47.3
Low	7	6	8	28.6	9	7	5	33.3	7	9	5	42.9
Little or none	2	9	10	47.6	4	7	10	47.6	4	6	11	52.4
Total				44.3				41.0				47.6
	Summer											
High	9	4	3	56.2	Data range too low				Data range too low			
Low	17	20	21	34.8								
Little or none	0	1	2	66.6								
Total				40.3								

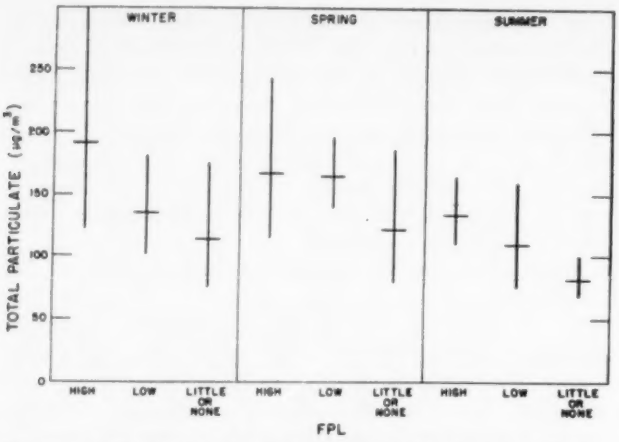

FIGURE 4.—Total particulate values compared to forecast pollution level (FPL). Horizontal line gives geometric mean and vertical line shows limits of one standard deviation.

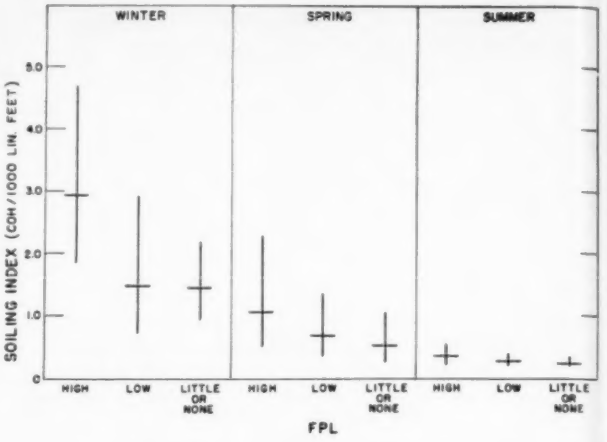

FIGURE 6.—Soiling index values compared to FPL.

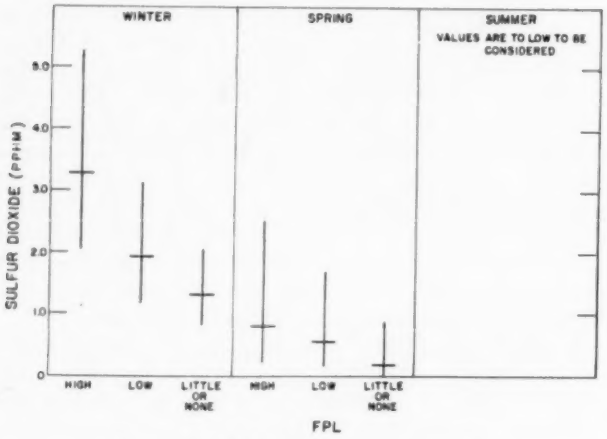

FIGURE 5.—SO_2 values compared to FPL.

depending whether they fell in the upper, middle, or lower third of the frequency distribution. Contingency tables (table 3) of these values plotted opposite the PL(OC) for each corresponding day were constructed, and percentages of agreement were computed. As expected, these figures are highest during the winter season when weather conditions are sharply defined and pollution ranges are high. With an overall winter average of 70 percent, the PL(OC)'s agree with the air quality level, as determined from the frequency distribution, approximately 7 out of 10 times. The averages during the other two seasons are significantly lower with the highest percentages of agreement for the high pollution and little or no pollution levels. The criteria effectively indicate three levels of pollution during the winter season and only two levels during the spring and summer seasons.

TABLE 4.—*FPL vs. MPL by seasons*

FPL	MPL											
	μg./m.³				SO_2				Coh/1000 linear ft.			
	High	Low	Little or none	Percent correct	High	Low	Little or none	Percent correct	High	Low	Little or none	Percent correct
	WINTER											
High	8	3	1	66.6	10	1	1	83.3	8	3	1	66.6
Low	3	6	3	50.0	3	5	4	41.7	3	3	6	25.0
Little or none	1	1	4	66.6	0	2	4	66.6	0	3	3	50.0
Total				60.0				63.3				46.7
	SPRING											
High	6	1	2	66.6	4	4	1	44.4	3	5	1	33.3
Low	6	9	0	60.0	6	5	4	33.3	6	4	5	26.7
Little or none	3	3	7	53.8	2	5	6	46.2	3	3	7	53.8
Total				59.5				40.6				37.8
	SUMMER											
High	9	6	1	56.2	Data range too low				Data range too low			
Low	8	8	6	36.3								
Little or none	0	4	7	63.6								
Total				49.0								

EVALUATION OF PROGRAM: FPL vs. MPL

Similar methods were used for the evaluation of the forecasts in terms of the measured pollution level. Here again, the data from the air quality measurements were separated first by season and then according to FPL. The geometric means and standard geometric deviations from the distributions thus obtained were plotted (figs. 4, 5, and 6) and compared. Again it is noticed that the means for all seasons are in the proper order. The forecasts divide the total particulate and sulfur dioxide data into three significantly different levels during the winter season, while the soiling index data are divided into only two distinguishable levels. During the spring season the SO_2 values are again too low to show discrimination and there is only recognizable discrimination between two levels of soiling index and total particulate. Soiling index and SO_2 data are too low to be considered during the summer season. Three significant levels of total particulate are, however, indicated, although the associated large standard deviations indicate that the discrimination is poor.

Table 4 is similar to table 3 except that the FPL is used instead of the PL(OC). The period of highest forecast verification occurred during the winter season with approximately 6 out of 10 forecast pollution levels in agreement with the air quality levels as determined from the frequency distributions. The percentages, however, do indicate that the winter forecasts are more accurate for the highest and lowest levels as compared to the middle level. During the spring and summer seasons approximately half of the forecast levels agree with the associated total particulate levels, and the percentages indicate a greater agreement for the highest and lowest levels during the summer season. SO_2 and soiling index percentages are somewhat lower during the warmer seasons because of the low range of the data. This is a consequence of the increased relative importance of ordinarily random variations of source strength, wind direction, local currents, and other meteorological variables.

4. CONCLUSIONS AND RECOMMENDATIONS

The tested meteorological criteria are shown to be good indicators of three air pollution levels during the winter season, but can discriminate between only two levels during the spring and summer. Of the three methods of measuring air quality, only total particulate maintains high enough values to be considered as a year-round air pollution indicator. Sulfur dioxide and soiling index measurements are very low during the summer season and considered alone imply the absence of community air pollution problems during that season.

While the results are not outstanding, it is believed that forecasting skill would improve with further experience. More elaborate meteorological criteria could have been used which might have given better discrimination among the levels, but such a method would lack the desired forthright manner of the one used. Other straightforward criteria could be devised and tested using the same air quality data and associated meteorological conditions. Among the various weather parameters which could be investigated are average wind speed, wind direction, and the presence or absence of an upper inversion. An additional influential parameter could be the duration of low wind speeds and/or interruption of these low speeds by periods of significant wind speed.

The primary value of this program has been to demonstrate that objective forecast methods can be used by local Weather Bureau offices to forecast daily air pollution levels during those seasons of the year when air pollution concentrations are high and troublesome. The forecast method is general enough that similar methods could be applied to other cities after due consideration of climatology, topography, industrial locations, and the individual needs of the organizations which are using the forecasts.

ACKNOWLEDGMENTS

The writers wish to express thanks and appreciation to Mr. Francis Pooler, Jr. and Mr. Earl H. Markee, Jr., for their helpful suggestions and careful review of this paper.

THE OCCURRENCE OF ANOMALOUS WINDS AND THEIR SIGNIFICANCE

M. A. ALAKA

National Hurricane Research Project, U.S. Weather Bureau, Miami, Fla.

[Manuscript received May 9, 1961; revised August 14, 1961]

ABSTRACT

Observational evidence is provided for the occurrence of anomalous winds which represent an anticyclonic rotation in space, and a mechanism for their development is suggested. The unstable nature of these winds and the role they play in the development of certain types of atmospheric disturbances is then discussed, and it is suggested that anomalous winds provide the dynamic mechanism for triggering hurricane formation and for the observed deepening of troughs downstream from intense pressure ridges. Finally it is noted that although the observational evidence presented is for the occurrence of anomalous winds over small regions of the atmosphere, their development is dependent on large-scale processes and their effect extends beyond the area where they occur.

1. INTRODUCTION

The gradient wind equation is a quadratic and thus has two solutions. One of these solutions, appropriate to anticyclonic flow, represents a clockwise rotation in space and is, therefore, in the opposite sense to the earth's rotation. Meteorologists have traditionally given little attention to this solution and some even consider it as an algebraic accident with little or no physical significance. Although there are cogent reasons to believe that winds corresponding to this solution do not occur on a large scale, the contention, *ipso facto*, that this solution is of no importance is not justified and has probably had far-reaching effects in eliminating from consideration some promising avenues of research in connection with the development of atmospheric disturbances.

In recent years there has been a slow trickle of evidence, both theoretical and observational, that these so called "anomalous winds" occur more frequently than had been suspected. But, by and large, meteorologists are still not sufficiently aware of these winds nor of their importance. The purpose of the present study is not only to provide further evidence of the occurrence of anomalous winds, but also to demonstrate that these winds are germane to the development of dynamic instability in curved airflow and, as such, are relevant to the development of certain types of atmospheric circulations.

2. ELEMENTARY DYNAMICS OF ANTICYCLONIC MOTION

To introduce the problem, we shall review some elementary aspects of the dynamics of anticyclonic motion.

The gradient wind equation may be written:

$$K_t V^2+fV=b_n \tag{1}$$

were $K_t=1/R_t$=trajectory curvature considered positive for cyclonic motion; V=magnitude of the horizontal wind; f=Coriolis parameter; and $b_n=-\alpha\partial p/\partial n$=pressure gradient force. From equation (1)

$$V=-\frac{f}{2K_t}\left(1\pm\sqrt{1+\frac{4K_t b_n}{f^2}}\right) \tag{2}$$

Since V must always be positive, the solution with the plus sign has a physical meaning only when K_t is negative; i.e., when the flow is anticyclonic.

We shall confine our discussion to anticyclonic flow and put $K_t'=-K_t$. The two solutions of equation (2) reduce to:

$$V_1=\frac{f}{2K_t'}\left(1-\sqrt{1-\frac{4K_t' b_n}{f^2}}\right) \tag{3}$$

and

$$V_2=\frac{f}{2K_t'}\left(1+\sqrt{1-\frac{4K_t' b_n}{f^2}}\right) \tag{4}$$

From the above equations it can be seen that

$$V_1\leq\frac{f}{2K_t'} \tag{5}$$

and

$$V_2\geq\frac{f}{2K_t'} \tag{6}$$

We differentiate equation (1) with respect to V

$$\frac{db_n}{dV}=2VK_t+f \tag{7}$$

and note that db_n/dV can be zero; i.e., b_n has an extreme value if K_t is negative. This value is reached when

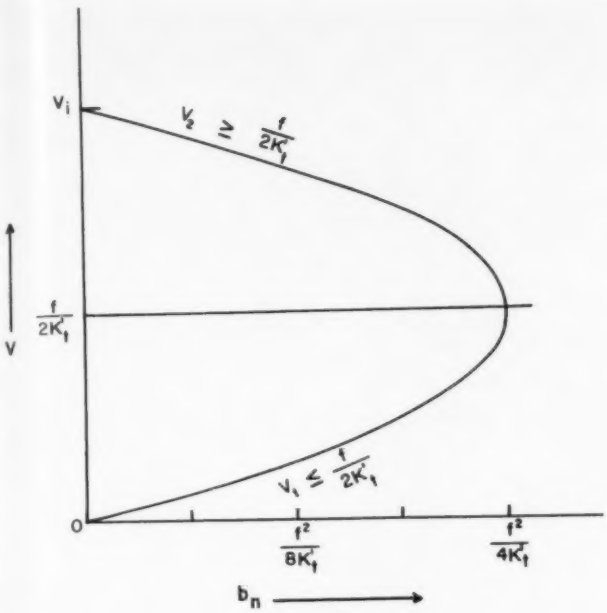

FIGURE 1.—Variation of gradient anticyclonic wind speed with pressure gradient.

$$V=-\frac{f}{2K_t}=\frac{f}{2K_t'} \tag{8}$$

and represents the maximum value

$$b_n=-\frac{f^2}{4K_t}=\frac{f^2}{4K_t'} \tag{9}$$

which the pressure gradient can attain in anticyclonic motion.

Figure 1 shows the variation of V with b_n in accordance with equation (1). It is seen that the two solutions meet at $V=f/2K_t'$ when the pressure gradient is at its maximum value $f^2/4K_t'$. From this point, where the wind is equal to twice the geostrophic wind V_g, the two solutions V_1 and V_2, corresponding respectively to equations (3) and (4) branch out. V_1 decreases with decreasing pressure gradient and vanishes when the latter becomes zero. This corresponds to the conditions normally observed in the atmosphere. We shall therefore term V_1 the normal solution of the anticyclonic gradient wind equation. V_2, on the other hand, increases with decreasing pressure gradient and at $b_n=0$ reaches the value $V_t=f/K_t'$ and the flow becomes inertial. Following Gustafson [7], we shall term V_2 the anomalous solution.

Figure 2 shows the variation of the gradient anticyclonic wind with trajectory curvature, assuming a constant pressure gradient. It is seen that, in contrast with

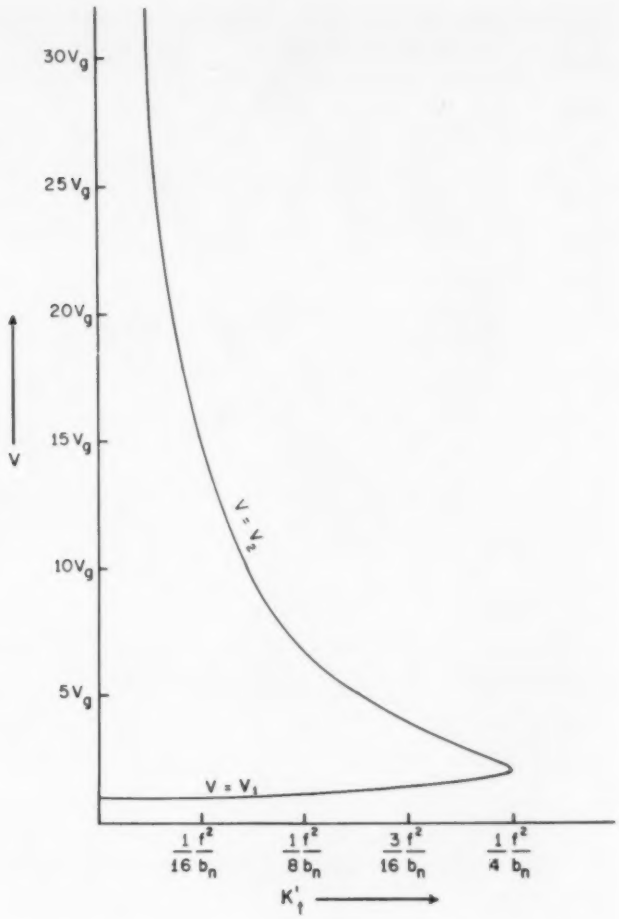

FIGURE 2.—Variation of gradient anticyclonic wind speed with trajectory curvature. V_g denotes the geostrophic wind.

normal anticyclonic winds which increase with increasing curvature, anomalous winds show a sharp decrease with increasing curvature.

As mentioned in the introduction, meteorologists in general have attributed little importance to the anomalous solution on the basis that it is seldom, if ever, realized in the atmosphere [5] or that its occurrence is limited to small-scale mechanically produced vortices, or to atmospheric eddies produced by friction [11]. The standard arguments in support of this view are usually some variation of the following:

a. The anomalous solution requires a clockwise rotation in space and, therefore, in the opposite sense to that of the earth. There is no known mechanism capable of producing such a motion on a large scale.

b. By expanding the quantity under the radical sign in equations (3) and (4), we obtain

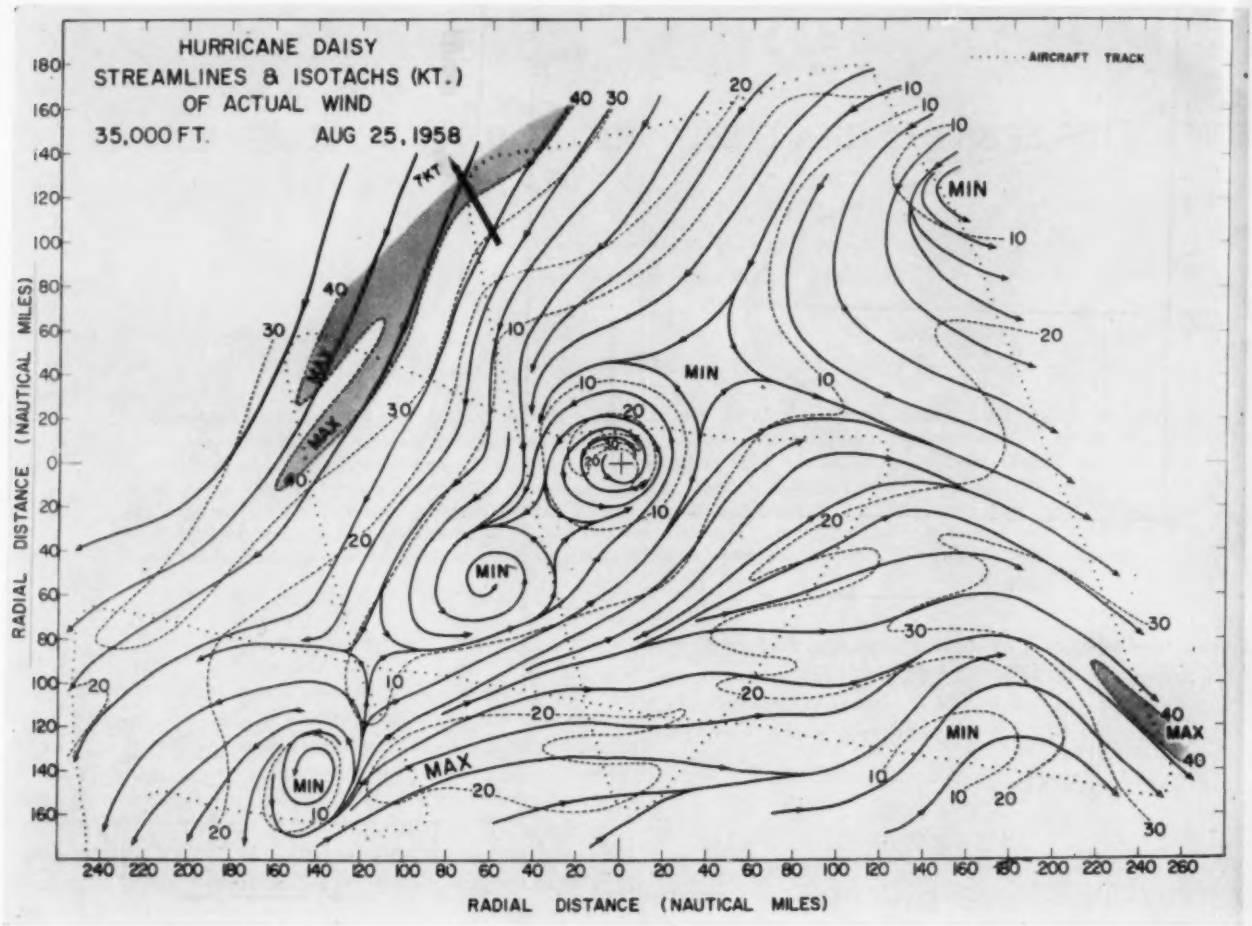

FIGURE 3.—Wind field at 35,000 ft. (pressure altitude, U.S. Standard), around hurricane Daisy on August 25, 1958.

$$V_1=\frac{f}{2K_t'}\left[1-\left(1-\frac{2K_t'b_n}{f^2}-\frac{2K_t'^2b_n^2}{f^4}+\cdots\right)\right]$$

$$=\frac{b_n}{f}+\frac{K_t'b_n^2}{f^3}+\cdots \tag{10}$$

and

$$V_2=\frac{f}{2K_t'}\left[1+\left(1-\frac{2K_t'b_n}{f^2}-\frac{2K_t'^2b_n^2}{f^4}+\cdots\right)\right]$$

$$=\frac{f}{K_t'}-\frac{b_n}{f}-\frac{K_t'b_n^2}{f^3}+\cdots \tag{11}$$

V_1 is thus continuous when the curvature decreases indefinitely and the isobars are nearly straight. On the other hand, for indefinitely small curvature, V_2 becomes infinitely large and would require an infinite supply of energy, which is not available in the atmosphere [5].

3. EVIDENCE OF THE OCCURRENCE OF ANOMALOUS WINDS

In contrast with the above arguments, there are others which indicate that both solutions for gradient anticyclonic flow are satisfied. Godson [6], for instance, considers a moving anticyclonic streamline system and expresses the gradient wind relation as follows:

$$V=\frac{fR_c+C\cos\psi}{2}\pm\left[\left(\frac{fR_c+C\cos\psi}{2}\right)^2-fR_cV_g\right]^{1/2} \tag{12}$$

where R_c=radius of contour curvature, C=speed of streamline system, ψ=angle from the direction of motion of the streamline system to the wind direction. Godson argues that if $C\cos\psi<0$, it is possible to obtain two values of V both of which are greater than $2V_g$ and thus correspond to the classically rejected root. On the other

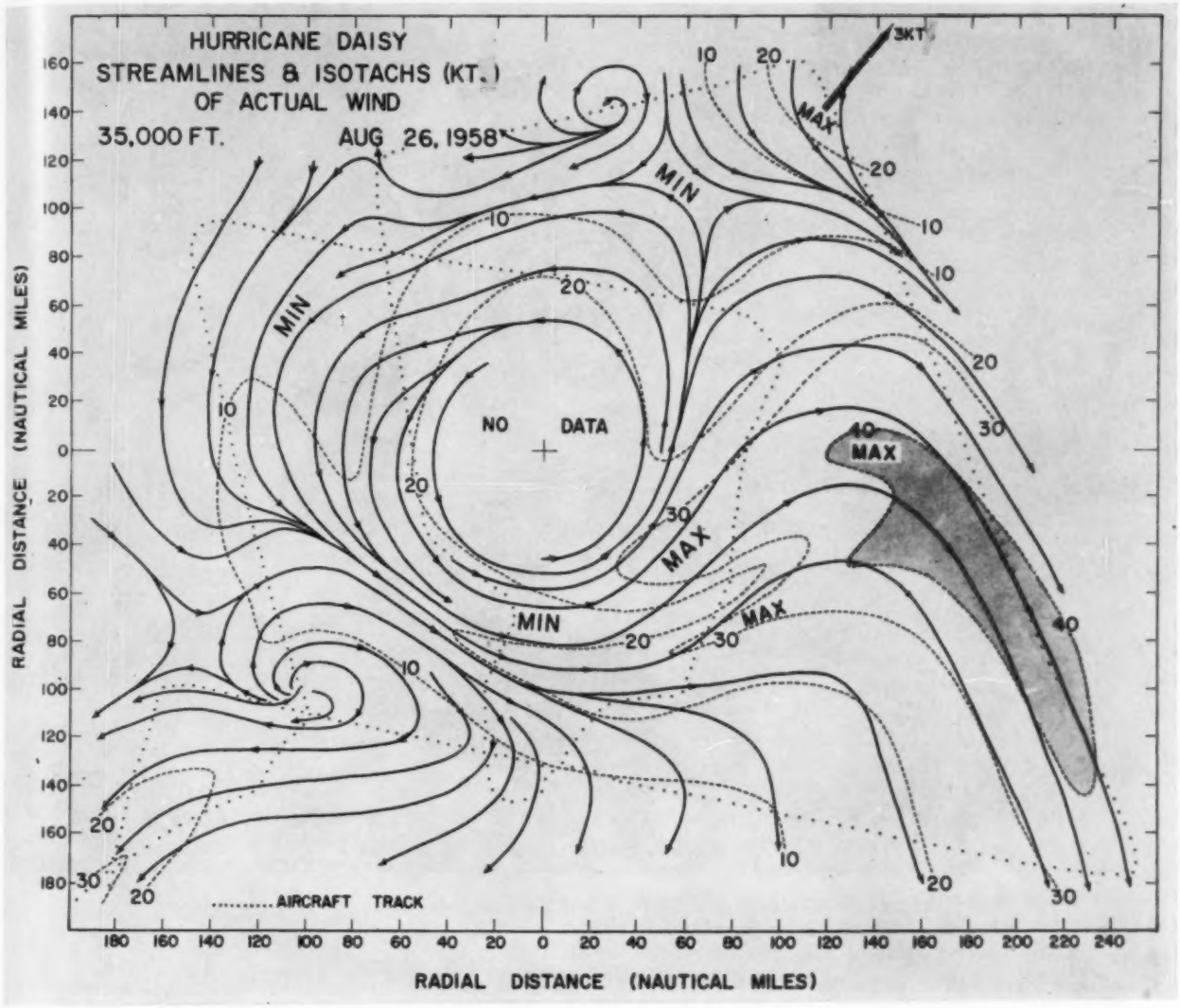

FIGURE 4.—Wind field at 35,000 ft. around hurricane Daisy on August 26, 1958.

hand if $C \cos \psi > 0$, it is possible to obtain values of V both of which are less than $2V_g$ and thus correspond to the classically accepted root. He concludes that both roots of the gradient wind equation for anticyclonic flow occur in the atmosphere.

On the observational side, indirect evidence that anomalous winds occur was provided by Gustafson [7] who compared observed winds with geostrophic winds in a moving pressure ridge at 700 mb. and applied the following criteria which follow directly from equations (5) and (6) above:

$$\left.\begin{aligned} V_1 &\leq 2V_g \cos\beta \\ \text{and} \qquad V_2 &\geq 2V_g \cos\beta \end{aligned}\right\} \tag{13}$$

where β is the deviation in direction between the observed and geostrophic winds, measured clockwise from due east. In a 3-day sequence Gustafson found consistent positive deviation from geostrophic directions to the west of the moving ridge and similarly consistent negative deviations to the east of it.

More recently, Angell [3] has furnished more direct evidence of the occurrence of anomalous flow from an evaluation of transosonde flights at 300 mb. In one instance the transosonde performed a full clockwise loop in 36 hours with an estimated angular velocity of -0.48×10^{-4} sec.$^{-1}$ This represents anomalous flow since the angular velocity of the earth at that locality (30°N.) is 0.36×10^{-4} sec.$^{-1}$ More significantly, perhaps, the transosonde trajectories suggested the occasional occur-

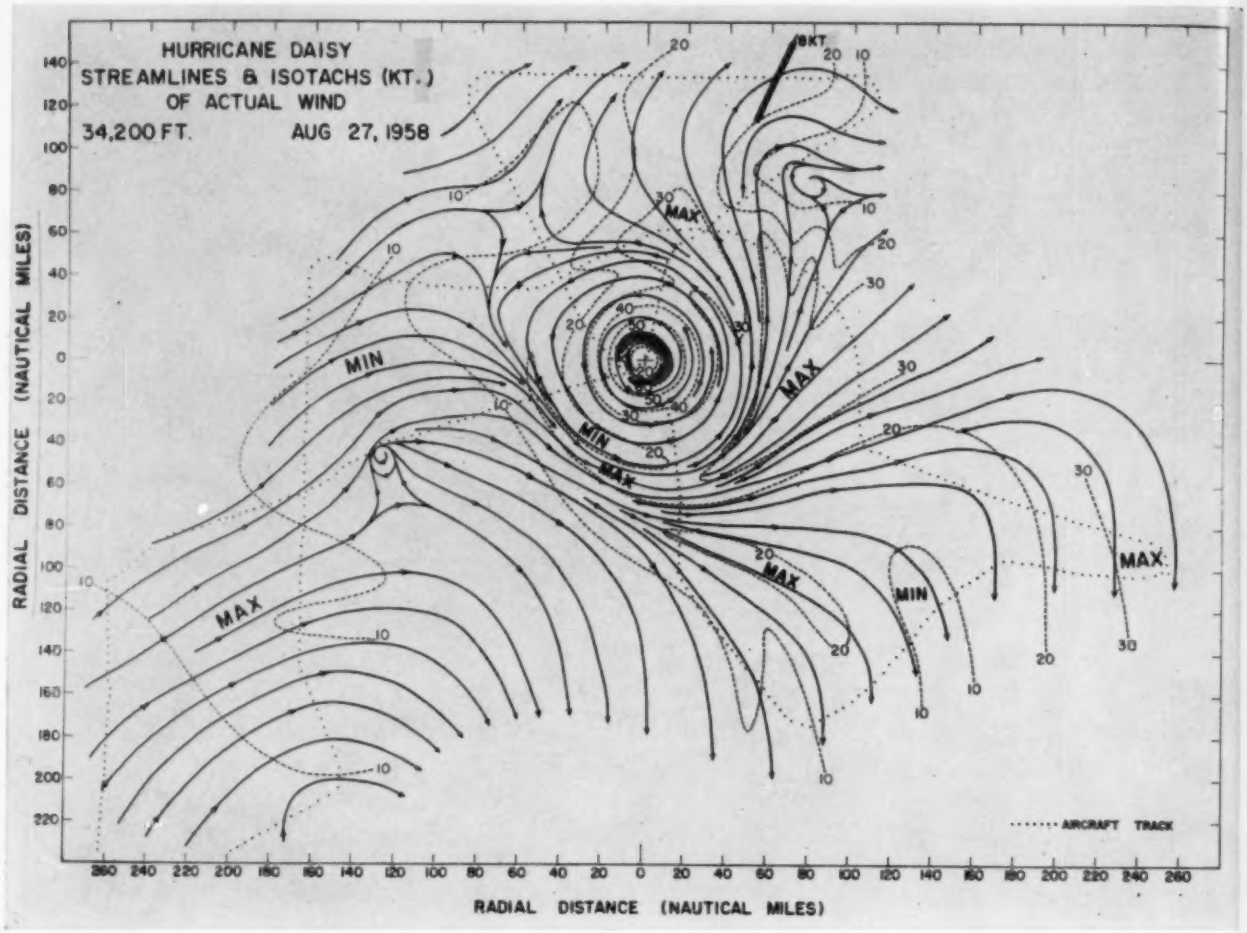

FIGURE 5.—Wind field at 34,200 ft. around hurricane Daisy on August 27, 1958.

rence of anomalous flow on the ridges of long waves in the westerlies. The significance of this fact will be discussed in section 7, below.

Since the summer of 1956, the National Hurricane Research Project (NHRP), U.S. Weather Bureau, has been operating three specially instrumented airplanes to make detailed observations in and near hurricane cores. A discussion of the characteristics and properties of the instrumentation was given by Hilleary and Christensen [10] and will not be repeated here. Among the most successful missions flown were those in connection with hurricane Daisy which developed near the Bahamas on August 24, 1958. This hurricane had a well-defined and concentrated wind circulation and presented a clear-cut radar configuration which greatly facilitated the location of the storm core. Flight missions were made at different levels on four days from August 25 to August 28, 1958. Among the elements measured were the wind, the temperature, and the radio and pressure altitudes. Quasi-instantaneous values of these parameters were punched on cards at specified intervals ranging from 10 seconds away from the core, to 2 seconds in the core. The punched cards were then evaluated by machine processing and the various parameters were plotted on a coordinate system fixed with respect to the storm center.

Figures 3, 4, and 5 show the wind field obtained by analyzing the observations made in the upper troposphere on August 25, 26, and 27. In making these analyses, it was necessary to regard as quasi-simultaneous, observations which, in fact, were made over a period of several hours. It is, however, believed that this shortcoming does not invalidate the results obtained.

From the wind fields thus obtained, values of the speed and direction were plotted on a rectangular grid of points 20 n.mi. apart. From these, computations of the quantity $2VK_t$ were made on the IBM 650 computer. The curvature of the trajectory K_t was computed from the following relations:

If u and v are the westerly and southerly components of the wind, and if we define

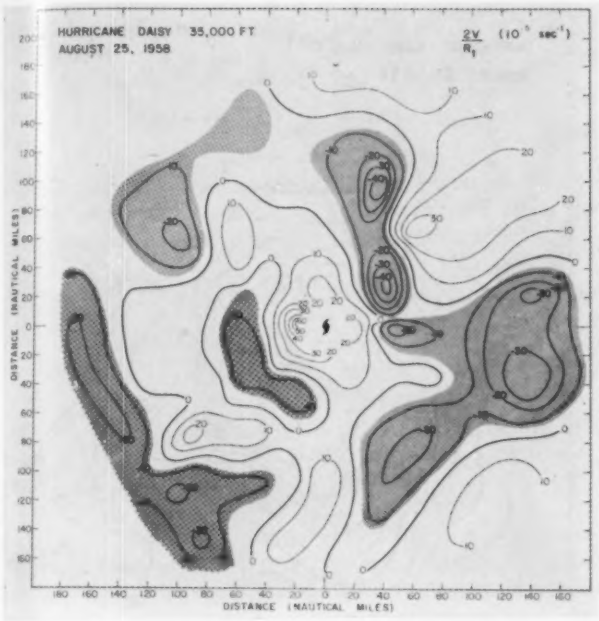

FIGURE 6.—Field of the quantity $2V/R_t$ at 35,000 feet (pressure altitude, U.S. Standard), around hurricane Daisy on August 25, 1958. Areas with anomalous winds are shaded.

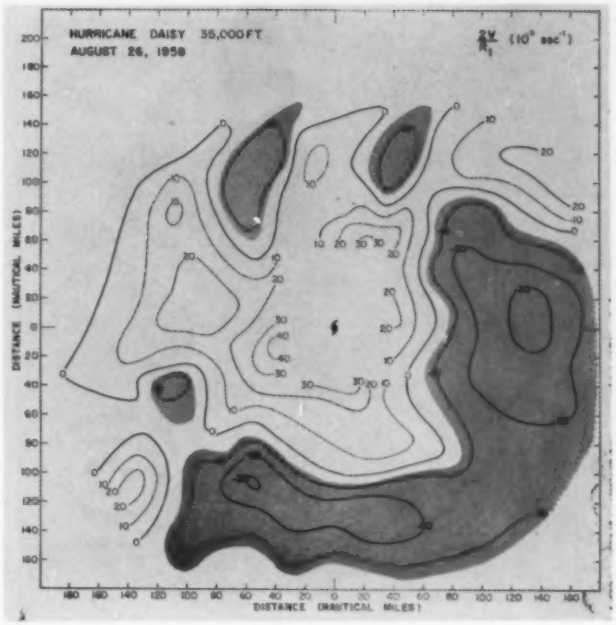

FIGURE 7.—Field of the quantity $2V/R_t$ at 35,000 ft. for August 26, 1958.

$$\psi=\tan^{-1}\frac{u}{v} \tag{14}$$

then

$$\begin{aligned}K_t&=-\frac{d\psi}{ds}=\cos^2\psi\left(\frac{u}{v^2}\frac{dv}{ds}-\frac{1}{v}\frac{du}{ds}\right)\\&=\frac{1}{V^2}\left(u\frac{dv}{ds}-v\frac{du}{ds}\right)\\&=\frac{1}{V^3}\left(u\frac{dv}{dt}-v\frac{du}{dt}\right)\end{aligned} \tag{15}$$

If the motion of the storm is represented by the vector $\mathbf{c}$ with components c_x and c_y in the east and north directions, respectively, and if we assume steady state conditions,

$$\begin{aligned}K_t&=\frac{1}{V^3}[u(\mathbf{V}-\mathbf{c})\cdot\nabla v-v(\mathbf{V}-\mathbf{c})\cdot\nabla u]\\&=\frac{1}{V^3}\left\{u[(u-c_x)]\frac{\partial v}{\partial x}+(v-c_y)\frac{\partial v}{\partial y}\right.\\&\qquad\left.-v\left[(u-c_x)\frac{\partial u}{\partial x}+(v-c_y)\frac{\partial u}{\partial y}\right]\right\}\end{aligned} \tag{16}$$

Figures 6, 7, and 8 represent fields of the quantity $2K_t V=2\ V/R_t$ corresponding to the wind fields of figures 3, 4, and 5, respectively. Regions where this quantity is negative and numerically greater than the Coriolis parameter, i.e., areas where the winds are anomalous, are shaded. The consistency of the patterns of these areas from day to day attests to their authenticity and demonstrates beyond any reasonable doubt that anomalous winds do occur. It will be noted, however, that the areas covered by these winds represent narrow strips of the order of 1 to 2 degrees of latitude in width, and are, therefore, likely to escape detection by ordinary synoptic analysis. In addition, the vertical extent of these winds is also limited, as can be noted from the fact that they are not found in figure 9 which represents the field of $2V/R_t$ a few thousand feet below that of figure 6. This is perhaps the reason why meteorologists in general have failed to realize both the reality and importance of these winds. The latter stems from the fact that they represent an important mechanism for the development of atmospheric instability as we shall now proceed to show.

4. THE CONCEPT OF INSTABILITY OF ATMOSPHERIC MOTION

The concept of instability in the atmosphere appeared with the initial developments in the theory of atmospheric disturbances. As early as 1878, Rayleigh [13] investigated conditions under which small displacements at the boundary between two air streams grow into larger disturbances. At about the same time, Helmholtz [8] found that, under certain conditions, unstable gravity waves developed at the interface between two liquids of different density and velocity. The above studies culminated in the polar front theory of cyclone formation.

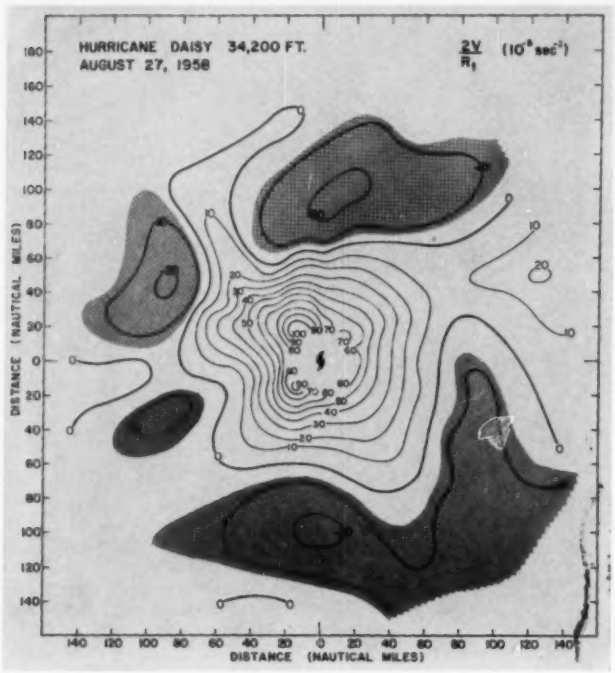

FIGURE 8.—Field of the quantity $2V/R_t$ for August 27, 1958, at 34,200 ft.

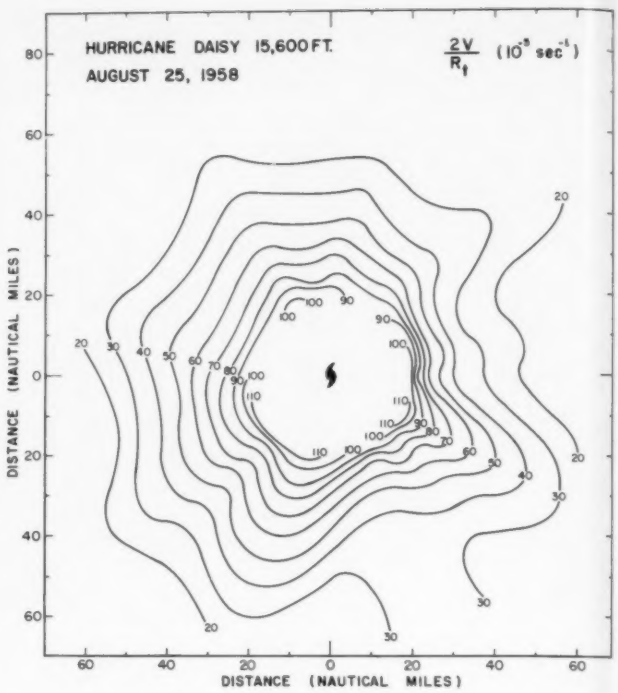

FIGURE 9.—Field of the quantity $2V/R_t$ at 15,600 ft. for August 25, 1958.

Paralleling the above studies, another series of investigations, beginning with those of Helmholtz [9] and Rayleigh [14] attempted to link instability in air currents with the quasi-horizontal distribution of the kinematic properties of the currents. This type of instability is usually known as dynamic instability.

In recent years, attention has been redirected to still another type of instability known as baroclinic instability. This type of instability, the importance of which was first pointed out by Margules [12], occurs by virtue of the vertical wind shear.

There is little doubt that the above three types of instability all play an important role in the atmosphere and there is an obvious need for a unified theory which combines them and brings out their relative importance and their interrelations. In the absence of such a theory, we must consider the particular type of instability which appears to have the most direct bearing on the problem at hand. In the present case, the importance of anomalous winds is best demonstrated by studying the circumstances attending the development of the so-called dynamic instability, with especial reference to atmospheric currents in curved motion.

5. DYNAMIC INSTABILITY IN CURVED AIRFLOW

In 1936, Solberg [16] investigated the conditions under which dynamic instability occurs in a steady symmetrical polar vortex which is initially in gradient equilibrium. Solberg's approach may be extended to any steady vortex in which the tangential variations of the wind are negligible in comparison with those in the radial direction.

Let us then consider such a vortex in which the angular speed ω is a function of the distance R from the axis of rotation. We shall proceed by the standard method and impose a small perturbation on this steady vortex and find out the circumstances under which the frequency of the total perturbed motion becomes imaginary.

If we disregard friction, we can express the equilibrium of forces acting on the steady vortex by the following equation,

$$\frac{V^2}{R^2}\mathbf{R}+\frac{2\Omega V}{R}\mathbf{R}-\theta\nabla\pi+\mathbf{g}=0 \qquad (17)$$

where V is the magnitude of the speed, Ω the earth's rotation, θ the potential temperature, $\mathbf{g}$ the gravity vector, and $\pi=c_p\,(p/1{,}000)^{R/c_p}$.

Let us now apply a uniform radial impluse to all the particles at distance R' from the axis so that at the time $t=t$ the particles form another circle with radius R. We stipulate that at any instant, the perturbed particles immediately acquire a pressure equal to that of the points which they are occupying at that instant. We further assume that the perturbed particles, in their displacement over a small distance S from their equilibrium position conserve both their potential temperature θ' and their

absolute angular momentum $M_a'=V'R+\Omega R'^2$ so that

$$\left.\begin{aligned}\theta-\theta'&=\mathbf{S}\cdot\nabla\theta\\ \text{and}\qquad M_a-M_a'&=\mathbf{S}\cdot\nabla M_a\end{aligned}\right\}\tag{18}$$

In addition to the forces indicated in equation (17), the perturbed particles sustain an acceleration $d^2\mathbf{S}/dt^2$ so that their motion is determined by the equation

$$\frac{d^2\mathbf{S}}{dt^2}+\frac{V'^2}{R^2}\mathbf{R}+\frac{2\Omega V'}{R}\mathbf{R}-\theta'\nabla\pi+\mathbf{g}=0\tag{19}$$

From equations (17) and (19), we obtain by subtraction

$$\frac{d^2\mathbf{S}}{dt^2}-\frac{V^2-V'^2}{R^2}\mathbf{R}-\frac{2\Omega}{R}(V-V')\mathbf{R}+(\vartheta-\theta')\nabla\pi=0\tag{20}$$

Now

$$V^2-V'^2=(V-V')\cdot 2V-(\delta V)^2\tag{21}$$

where $\delta V=V-V'$ is a perturbation quantity, the square of which may be neglected. Equation (20) thus becomes

$$\frac{d^2\mathbf{S}}{dt^2}-\left[\frac{2}{R}(\omega+\Omega)(V-V')\right]\mathbf{R}+(\vartheta-\theta')\nabla\pi=0\tag{22}$$

We now express the above equation in terms of the conservative quantity M_a and make use of the relations in (18); we obtain

$$\frac{d^2\mathbf{S}}{dt^2}-\left[\frac{2}{R^2}(\omega+\Omega)(\mathbf{S}\cdot\nabla M_a)+\frac{2}{R}(\omega^2+3\omega\Omega+2\Omega^2)\delta R\right]\mathbf{R}+(\mathbf{S}\cdot\nabla\theta)\nabla\pi=0\tag{23}$$

If the perturbation is very small compared to the dimensions of the vortex, i.e., if $(R-R')/R\approx 10^{-1}$, the term in δR in the above equation may be neglected and we finally have

$$\frac{d^2\mathbf{S}}{dt^2}-\left[\frac{2}{R^2}(\omega+\Omega)(\mathbf{S}\cdot\nabla M_a)\right]\mathbf{R}+(\mathbf{S}\cdot\nabla\theta)\nabla\pi=0\tag{24}$$

Let us assume that the displacement $\mathbf{S}$ is proportional to a function of the form $e^{i\nu t}$ and project equation (24) along two orthogonal directions: one corresponding to the vertical and the other to a radial direction. If the components of $\mathbf{S}$ along these directions are given by z and r, respectively, the projections of equation (24) along these directions are:

$$\left.\begin{aligned}\nu^2 z-\frac{2\omega_{az}}{R}\left(r\frac{\partial M_a}{\partial r}+z\frac{\partial M_a}{\partial z}\right)+\frac{\partial\pi}{\partial z}\left(r\frac{\partial\theta}{\partial r}+z\frac{\partial\theta}{\partial z}\right)&=0\\ \text{and}\qquad \nu^2 r-\frac{2\omega_{az}}{R}\left(r\frac{\partial M_a}{\partial r}+z\frac{\partial M_a}{\partial z}\right)+\frac{\partial\pi}{\partial r}\left(r\frac{\partial\theta}{\partial r}+z\frac{\partial\theta}{\partial z}\right)&=0\end{aligned}\right\}\tag{25}$$

where ω_a denotes the absolute rotation $(\omega+\Omega)$.

For nontrivial values of r and z, the determinant of the above system of linear equations vanishes and we obtain

$$\nu^4+\nu^2\left[\left(\frac{\partial\pi}{\partial z}\frac{\partial\vartheta}{\partial z}+\frac{\partial\pi}{\partial r}\frac{\partial\vartheta}{\partial r}\right)+\left(\frac{2\omega_{az}}{R}\frac{\partial M_a}{\partial r}-\frac{2\omega_{ar}}{R}\frac{\partial M_a}{\partial z}\right)\right]-\left(\frac{2\omega_{az}}{R}\frac{\partial\pi}{\partial z}+\frac{2\omega_{ar}}{R}\frac{\partial\pi}{\partial r}\right)\left(\frac{\partial M_a}{\partial z}\frac{\partial\vartheta}{\partial r}-\frac{\partial M_a}{\partial r}\frac{\partial\vartheta}{\partial z}\right)=0\tag{26}$$

Examining the order of magnitude of the various terms in equation (26), we find that

$$\left.\begin{aligned}&\frac{\partial\pi}{\partial z}\frac{\partial\theta}{\partial z}+\frac{\partial\pi}{\partial r}\frac{\partial\theta}{\partial r}=\nabla\pi\cdot\nabla\theta\approx 10^{-4}\\ &\frac{2}{R}\left(\omega_{az}\frac{\partial M_a}{\partial r}-\omega_{ar}\frac{\partial M_a}{\partial z}\right)=-2\boldsymbol{\omega}\cdot\nabla\times\mathbf{V}_a\approx 10^{-8}\\ &\frac{2}{R}\left(\omega_{az}\frac{\partial\pi}{\partial z}+\omega_{ar}\frac{\partial\pi}{\partial r}\right)\left(\frac{\partial M_a}{\partial z}\frac{\partial\theta}{\partial r}-\frac{\partial M_a}{\partial r}\frac{\partial\theta}{\partial z}\right)\\ &\qquad=(2\boldsymbol{\omega}_a\cdot\nabla\pi)(\nabla\theta\cdot\nabla\times\mathbf{V}_a)\approx 10^{-12}\end{aligned}\right\}\tag{27}$$

Solving for ν^2 and neglecting the last two terms of (27) in comparison with the first, we have

$$\nu_1^2=-\nabla\pi\cdot\nabla\theta\tag{28}$$

The value of this root is determined mainly by the static stability

$$-\frac{\partial\pi}{\partial z}\frac{\partial\theta}{\partial z}=\frac{g}{\theta}\frac{\partial\theta}{\partial z}\tag{29}$$

The second root ν_2^2 is obtained by dividing the third term of (27) by ν_1^2. Thus,

$$\nu_2^2=\frac{\frac{2}{R}\left(\omega_{az}\frac{\partial\pi}{\partial z}+\omega_{ar}\frac{\partial\pi}{\partial r}\right)\left(\frac{\partial M_a}{\partial z}\frac{\partial\theta}{\partial r}-\frac{\partial M_a}{\partial r}\frac{\partial\theta}{\partial z}\right)}{\frac{\partial\pi}{\partial z}\frac{\partial\theta}{\partial z}+\frac{\partial\pi}{\partial r}\frac{\partial\theta}{\partial r}}\tag{30}$$

The above equation will be greatly simplified if it is projected on an isentropic surface so that $\partial\theta/\partial r$ vanishes. In addition, since the angle between isobaric and isentropic surfaces is generally small, $(\partial\pi/\partial r)\approx 0$ and

$$\nu_2^2=[2\omega_{az}(\nabla\times\mathbf{V})_z]_\theta\tag{31}$$

Equation (31) is identical with Solberg's results for the polar vortex and states that the square of the frequency of the second root is equal to twice the product of the absolute rotation of the vortex and the vertical component of the absolute vorticity, as measured on an isentropic surface. If we now use a relative frame of reference fixed with respect to the earth, we have

$$\nu_2^2=\left[\left(\frac{2V}{R_t}+f\right)(\zeta+f)\right]_\theta\tag{32}$$

Since we are considering a steady vortex, the streamlines coincide with the trajectory and $R=R_t$. The frequency ν_2 becomes imaginary and the motion unstable when

$$\left[\left(\frac{2V}{R_t}+f\right)(\zeta+f)\right]_\theta<0\tag{33}$$

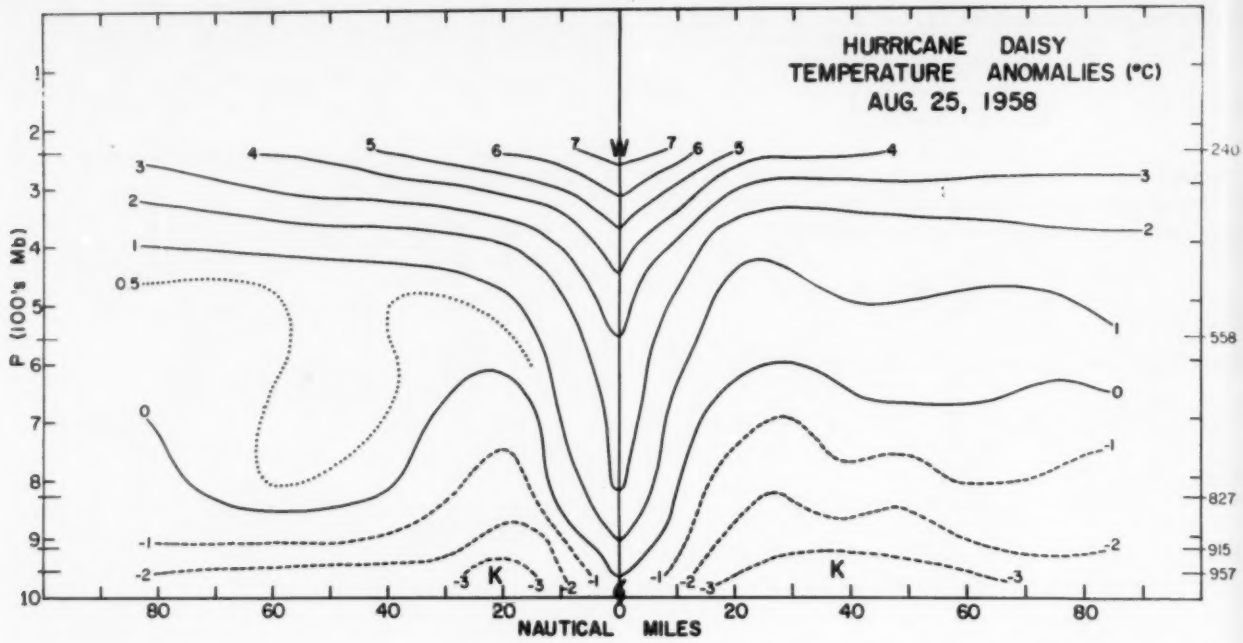

FIGURE 10.—Vertical cross-section of temperature anomalies from the mean August atmosphere in a direction perpendicular to that of the motion of hurricane Daisy, August 25, 1958. Pressures shown at the right edge indicate the levels at which data were available (analysis by J. A. Colón).

In other words, dynamic instability occurs with normal winds provided the absolute vorticity, as measured on an isentropic surface, is negative. Alternatively, instability occurs with positive absolute vorticity provided the wind, as measured on an isentropic surface, is anomalous.

The above criterion is identical with that obtained by van Mieghem [17]. The latter, however, did not envisage the possibility of the occurrence of anomalous winds and, therefore, equated the condition for the release of dynamic instability with the occurrence of negative absolute vorticity.

It should be noted that, according to the theory of equations, the second root may be obtained by subtracting ν_1^2 from the negative value of the coefficient of ν^2 in equation (26). If we then neglect the vertical wind shear ($\partial M_a/\partial z=0$), we have

$$\nu_2'^2=\left(\frac{2V}{R_s}+f\right)(\zeta+f) \tag{34}$$

which is similar to equation (32) except that the quantities are now measured on a level surface. Equation (34) is identical with the criterion for dynamic instability obtained by Sawyer [15].

Physically, the operation of the above criterion may be visualized by studying the balance of forces on an anticyclonic vortex which is initially in gradient balance. Let a particle be given an impulse toward lower pressure. If the flow is unstable, the particle tends to continue in the direction of the impulse. There are two cases to consider:

Case I: Instability with Normal Winds.—If the winds are normal, there is instability if the pressure gradient along the path of the particle increases at such a rate that the speed of the particle remains subgradient. This would require a rapid outward increase in anticyclonic rotation or a rapid decrease in cyclonic rotation expressed by the inequality

$$\left[\frac{1}{R}\frac{\partial}{\partial r}(VR)\right]_g<-f \tag{35}$$

Case II: Instability with Anomalous Winds.—From figures 1 and 2, it is seen that if the wind regime is anomalous, the speed increases with decreasing pressure gradient and trajectory curvature. Therefore, if the trajectory curvature of the particle remains constant, the pressure gradient along the trajectory should decrease at a fast rate; otherwise, the speed of the perturbed particle will eventually reach a speed greater than that appropriate for gradient equilibrium and its acceleration will be checked. Actually, however, the trajectory curvature decreases as the particle moves toward lower pressure. Therefore, instability can occur with a slower rate of pressure gradient decrease or, if the curvature decreases rapidly, instability can occur even with a slow outward increase of the pressure gradient.

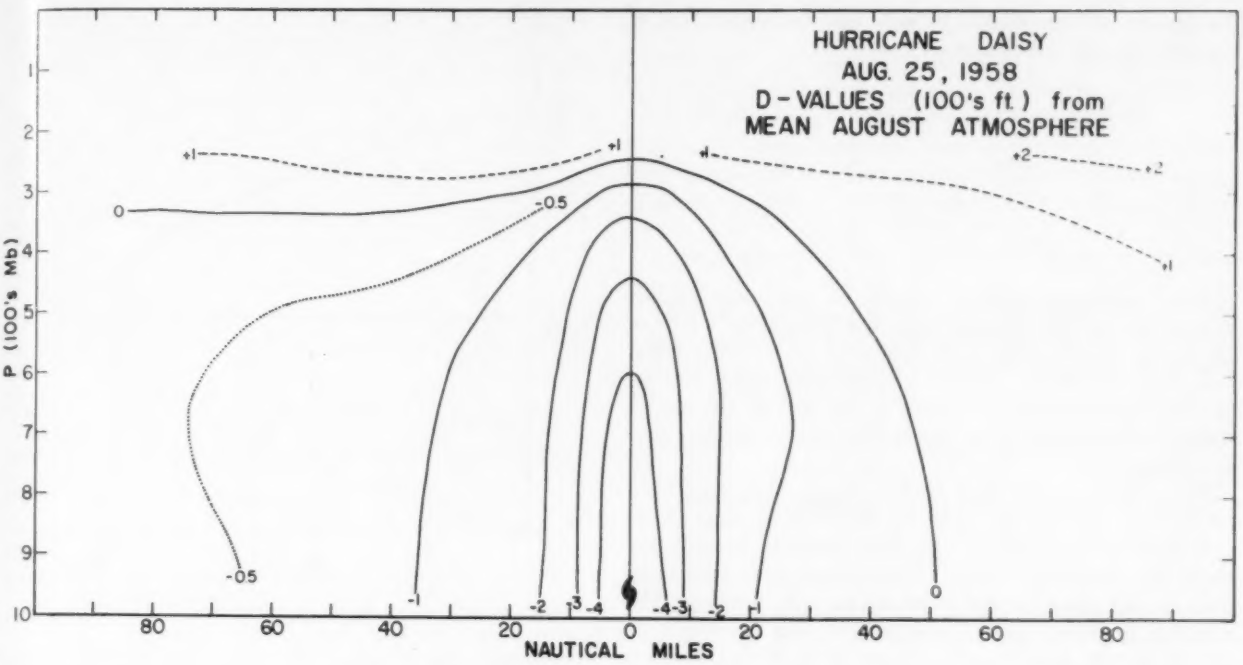

FIGURE 11.—Vertical cross-section of deviations of the altitudes of pressure surfaces from the mean August atmosphere ("D" values) in a direction perpendicular to that of hurricane Daisy, August 25, 1958 (analysis by J. A. Colón).

Equation (33) states that the motion is unstable so long as the combined effect of the change of wind speed curvature is such that

$$\left[\frac{1}{R}\frac{\partial}{\partial r}(VR)\right]_\phi > -f \tag{36}$$

6. A MECHANISM FOR THE DEVELOPMENT OF ANOMALOUS WINDS

An insight into the manner in which anomalous winds develop may be gained by considering the circulation theorem of Bjerknes which may be written [11]:

$$\left.\begin{aligned}\frac{dC_a}{dt}&=\frac{dC}{dt}+2\Omega\frac{d\sum}{dt}\\&=N_{a_1-p}\end{aligned}\right\} \tag{37}$$

$C_a=\oint_Q \mathbf{V}_a\cdot\delta\mathbf{r}$=absolute circulation around a closed curve Q.

$C=\oint_Q \mathbf{V}\cdot\delta\mathbf{r}$=relative circulation around the same curve.

Σ=the equatorial projection of the area within the curve Q.

N_{a_1-p}=the number of pressure-volume solenoids enclosed by the curve Q.

A comparison of figures 6, 10, and 11 indicates that there are few solenoids at the level and location where the anomalous winds occur. We may, therefore, set

$$\frac{dC}{dt}+2\Omega\frac{d\sum}{dt}=0 \tag{38}$$

or

$$C+2\Omega\sum=\text{constant} \tag{39}$$

If we approximate the hurricane to a simple circular vortex, the circulation at a distance R from the center is

$$C=2\pi R^2\omega \tag{40}$$

and

$$\sum=\pi R^2\sin\phi \tag{41}$$

where ϕ is the latitude.

Substituting the above values of C and Σ in (39), we obtain

$$R^2(\omega+\Omega_z)=\text{constant} \tag{42}$$

whence it can be seen that, in a circular vortex, disregarding the solenoid term in equation (37) is equivalent to assuming conservation of absolute momentum—a concept which is known to be applicable to upper-level hurricane circulation.

According to equation (42), if the vortex has horizontal convergence, the circles contract and ω increases. If, on the other hand, the circles expand as a result of horizontal

divergence, ω decreases. In this case, in order that ω should decrease sufficiently so that

$$\left.\begin{aligned} &\omega+\Omega_z\to 0 \\ \text{i.e.,}\quad &\\ &\frac{2V}{R}+f\to 0 \end{aligned}\right\} \tag{43}$$

R must approach infinity. Since the expansion cannot proceed so far, we conclude that the anomalous winds in figures 4, 5, and 6 were not produced by a symmetrical horizontal divergence of the air particles which arrived at these higher levels by ascent in the core of the storm. Another mechanism must be sought to account for their occurrence.

From figure 1 it is clear that a change of regime from normal to anomalous winds would be more difficult to accomplish if the pressure gradient force is much lower than the maximum value $f^2/4K'_t$, since this would require a big jump in the wind speed. If, however, the pressure gradient is nearly equal to the maximum, a comparatively small impulse would be sufficient to shift an air particle from the lower to the upper branch of the V curve of figure 1.

Let us visualize initial conditions characterized by an anticyclonic air stream in gradient equilibrium. In figure 12, let A be the equilibrium position of a particle in this stream. Now let us visualize that the equilibrium is disturbed by an increase in the pressure gradient brought about, for instance, by an interaction between tropical and extratropical pressure systems. Two cases may be discussed: *Case A.*—The increase of the pressure gradient force is from P to P_1, i.e., the resulting pressure gradient force is well below the maximum $f^2/4K'_t$. The wind, having become subgradient, the particle turns toward lower pressure and accelerates. Having reached the equilibrium speed B, unless there is considerable damping, the particle may slightly overshoot this position to B_1. It then oscillates with decreasing amplitude about the equilibrium position until balance is finally reached at B.

Case B.—The increase of the pressure gradient force is from P to P_2; i.e., the increased pressure gradient force is nearly equal to the maximum value $f^2/4K'_t$. In this case, the speed of the accelerating particle, by overshooting the equilibrium position, may reach the value B_3 which is in excess of the critical speed $f/2K'_t$. Whereas at B_2 the speed of the particle is supergradient, and at B_3 it is subgradient for the same pressure gradient. Thus, by overshooting the critical speed, the particle is henceforth constrained to move toward lower pressure and sustain further acceleration unless the distribution of the wind field along its path is such that the absolute vorticity is negative; in this case the motion will be stabilized in accordance with equation (33).

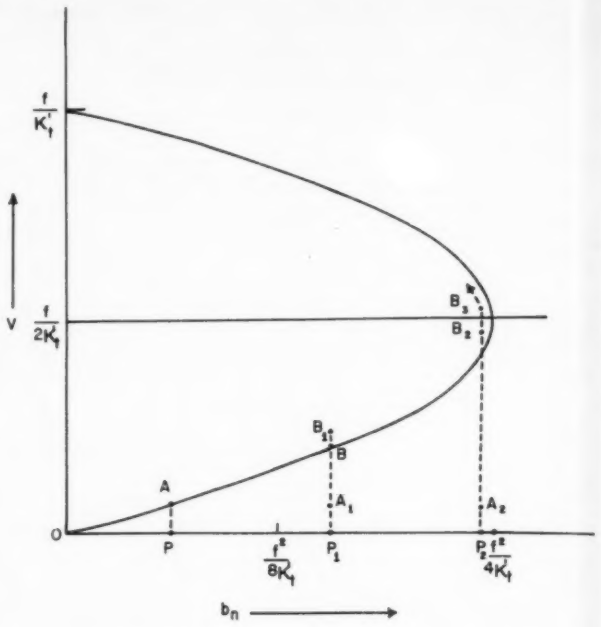

FIGURE 12.—Illustrating the development of anomalous winds (see text).

7. EXAMPLES OF SITUATIONS IN WHICH ANOMALOUS WINDS PLAY A ROLE

In a previous paper [1], the author suggested from theoretical considerations that the occurrence of anomalous winds in the manner described above provides a mechanism for triggering hurricane development. Details concerning how this is brought about and some observational evidence to this effect are given in a separate paper [2] and are beyond the scope of the present study. Here we would suggest that, in view of their essentially unstable nature, anomalous winds must play an important role not only in hurricane formation but also in other types of atmospheric development, especially those which occur downstream from a pressure ridge which has undergone marked intensification, or those accompanying the superposition of strong westerly winds on the crests of the long waves.

A case in point is that discussed by Bjerknes [4] linking the deepening of a wave trough with a strong intensification of the ridge upstream from it. Specifically, Bjerknes suggests that if the ridge intensifies so that the curvature of the contours exceeds a critical value

$$\frac{f^2}{4b_n}=\frac{f}{4V_g} \tag{44}$$

where V_g denotes the geostrophic wind, the air particles cannot follow the contours and must perforce flow to-

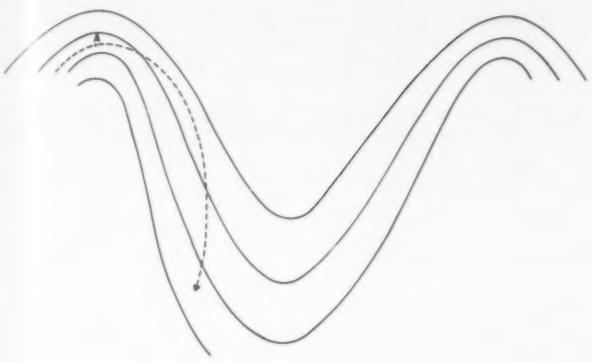

FIGURE 13.—Illustrating the cyclogenetic effect of anomalous winds. The dashed curve represents the probable trajectory of an air particle after its speed changes to the anomalous regime at the point A.

ward lower pressure and accelerate. The acceleration results in supergradient winds which then curve back to higher pressure, the net result being a deepening of the trough downstream from the ridge.

Now that the likelihood of the occurrence of anomalous winds in situations analogous to that described above has been demonstrated, the deepening of the trough may be looked at in a new light. Let us suppose that the wind becomes anomalous as a result of the strengthening of the pressure gradient to a value near the maximum possible for anticyclonic flow, and let us follow the trajectory of a particle situated at the point A in figure 13, where the wind changes regime and becomes subgradient in the manner discussed in the previous section. As a result, the air particle moves to lower pressure and accelerates. In doing so, its curvature decreases, as can be seen from the figure. Unless the pressure gradient along the trajectory increases rapidly, the progressively decreasing curvature requires an increasingly stronger speed for balanced motion (see fig. 2) and the particle, therefore, continues to accelerate. However, if the curvature vanishes so that the particle follows a straight trajectory, the wind instantly becomes supergradient and the particle must curve back to higher pressure. In the mean, the particle must, therefore, follow a slightly anticyclonic trajectory and is constrained by the geometry of the pressure distribution to curve back to higher pressure, as shown by the dashed curve in figure 13.

In this connection it is of interest to mention that Angell [3] has noted that anomalous flow toward higher pressure can occur continuously for several hours. Thus, by stipulating the occurrence of anomalous winds, we arrive at the same ultimate deepening envisaged by Bjerknes.

8. CONCLUSION

Although the observational evidence presented here is for the occurrence of anomalous winds over small regions of the atmosphere, it is significant to note:

A. that their occurrence may be dependent on large-scale processes, such as those involving the intensification of pressure ridges or the latitudinal shift of the westerlies; and

B. that their effect extends beyond the area where they occur.

The fact that these winds can occur only in anticyclonic motion again demonstrates the vital regulatory role of the high pressure regions in determining the state and motion of the atmosphere.

ACKNOWLEDGMENTS

The author wishes to acknowledge his indebtedness to his colleague, Dr. Stanley L. Rosenthal, for his help in programming the computations mentioned in section 3. The author also wishes to record his appreciation to Dr. José A. Colón for making available figures 10 and 11, and to Mr. Daryl T. Rubsam who is responsible for figures 3, 4, and 5. Finally, acknowledgment is due Mrs. Miree Moore and Mr. A. M. Recht for their help in plotting, and to Messrs. R. Carrodus and C. True for reproducing the figures.

REFERENCES

1. M. A. Alaka, "Dynamics of Upper-Air Outflow in Incipient Hurricanes," *Geophysica*, vol. 6, No. 3–4 1958, pp. 133–146.
2. M. A. Alaka, "The Occurrence of Dynamic Instability in Incipient and Developing Hurricanes." (To be published.)
3. J. K. Angell, "An Analysis of Operational 300-mb. Transosonde Flights from Japan in 1957–58," *Journal of Meteorology*, vol. 17, No. 2, Feb. 1960, pp. 20–35.
4. J. Bjerknes, "Extratropical Cyclones," *Compendium of Meteorology*, American Meteorological Society, Boston, 1951, pp. 577–598.
5. D. Brunt, *Physical and Dynamical Meteorology*, Cambridge University Press, 1939, 428 pp.
6. W. L. Godson, "Some Remarks Concerning the Gradient Wind Equation," *Bulletin of the American Meteorological Society*, vol. 30, No. 12, December 1949, pp. 342–346.
7. A. F. Gustafson, "On Anomalous Winds in the Free Atmosphere," *Bulletin of the American Meteorological Society*, vol. 34, No. 5, May 1953, pp. 196–201.
8. H. Helmholtz, "Über Atmosphärische Bewegungen," *Meteorologische Zeitschrift*, vol. 5, 1888, pp. 329–340.
9. H. Helmholtz, "On Atmospheric Movements," *Smithsonian Miscellaneous Collection*, vol. 34, 1893, (translated by C. Abbe).
10. D. T. Hilleary and F. E. Christensen, "Instrumentation of National Hurricane Research Project Aircraft," *National Hurricane Research Project Report* No. 11, 1957.
11. J. Holmboe, G. E. Forsythe, and W. Gustin, *Dynamic Meteorology*, John Wiley and Sons, New York, 1954, 348 pp.
12. M. Margules, "Über die Energie der Stürme," *Jahrbuch K. K., Zentralanstalt für Meteorologie und Geodynamik*, Wien, Bd. XL, 1905, pp. 1–26.
13. Lord Rayleigh, "On the Instability of Jets," *Proceedings of the Mathematical Society of London*, vol. 10, 1878, pp. 4–13.

14. Lord Rayleigh, "On the Stability of the Laminar Motion of an Inviscid Fluid," *Philosophical Magazine*, vol. 23, 1913, pp. 1001–1010.
15. J. S. Sawyer, "Notes on the Theory of Tropical Cyclones," *Quarterly Journal of the Royal Meteorological Society*, vol. 73, 1947, pp. 101–126.
16. H. Solberg, "Le mouvement d'inertie de l'atmosphère stable et son rôle dans la théorie des cyclones," *Procès-verbaux, l'Association Météorologique, UGGI, Edinbourg 1936*, Part II, 1939, pp. 66–82.
17. J. van Mieghem, "Hydrodynamic Instability," *Compendium of Meteorology*, American Meteorological Society, Boston, 1951, pp. 434–453.

THE WEATHER AND CIRCULATION OF AUGUST 1961

Record Heat from the Northern Plains to the Pacific Coast

JAMES F. ANDREWS

Extended Forecast Branch, U.S. Weather Bureau, Washington, D.C.

1. HIGHLIGHTS

August 1961 continued the succession of hot dry months in the northwestern United States[1] with average and daily temperatures reaching record levels in many areas. Severe drought persisted in the Northern Plains and by the end of the month conditions were comparable with the most severe drought of other years.

The Midwest and South were unseasonably cool, continuing a pattern that began in April of this year. The most persistent coolness occurred in the western Gulf States where mean temperatures for the month were at or near record levels.

This sharp contrast in weather regimes was also characteristic of the summer season and was related to an abnormal mid-tropospheric circulation.

2. MONTHLY MEAN CIRCULATION

The average circulation pattern at 700 mb. for August 1961 (fig. 1) featured an unusually strong ridge over western North America. The height anomaly center associated with this ridge was the highest ever observed in this area during the Extended Forecast Branch period of record (since 1933). A companion feature of this ridge was a deeper than normal trough over the southeastern United States.

In the Pacific and North America the pattern of 700-mb. height and its anomaly exhibited a meridional character, with a deep mid-Pacific trough helping to support the strong ridge in the climatologically favored area over western North America (fig. 1). Elsewhere in the hemisphere, from the Atlantic across Asia, the circulation was markedly zonal.

The middle-latitude westerlies were stronger than normal and displaced northward during August over the western portion of the hemisphere (figs. 2, 3). Greatest displacement was over North America where a band of wind speeds as much as 5 m.p.s. above normal was observed across central Canada (fig. 3B). These fast westerlies were related to the deep cyclonic center in northeastern Canada and strong ridge to the west (fig. 1). In the United States, however, weaker than normal westerlies predominated. The contrasting wind speed anomaly pattern in North America (fig. 3B) is also inherent in the 700-mb. height anomaly pattern (fig. 1). Across Canada the anomalous flow was westerly, while in the United States easterly anomalous flow prevailed.

The westerlies over the eastern portion of the hemisphere were displaced south of their normal August position, primarily as a result of the blocking High and area of 700-mb. height anomaly centered near Novaya Zemlya (figs. 1, 3). Fast westerly flow prevailed across the Atlantic, Europe, and into Asia, with greatest wind speed departures, as much as 6 m.p.s., in central Europe (fig. 3B).

3. AVERAGE MONTHLY WEATHER

RECORD HEAT AND DRYNESS IN THE NORTHWEST

The northwestern United States, from the northern Great Plains to the Pacific coast, experienced one of the hottest and driest months ever recorded. Temperatures for August averaged from 4° to more than 6° F. above normal in all but coastal areas (fig. 4), while less than half the normal amount of precipitation fell in the Northern Plains (fig. 5). In many areas stations with long-period records reported that August 1961 was the warmest month of record. A representative list of these stations is shown in table 1.

The hottest weather occurred quite generally during the first week when a strong ridge dominated western North America. Extreme heat from the Cascade Mountains to the northern Great Plains sent temperatures well over 100° F., with many stations establishing new absolute

TABLE 1.—*Monthly mean high temperature records established in August 1961*

Station	Temperature (°F.)		
	Average monthly	Departure from normal	Year records began
Devils Lake, N. Dak.	72.6	5.8	1904
Williston, N. Dak.	74.9	6.8	1878
Rapid City, S. Dak.	77.2	6.3	1887
Billings, Mont.	76.2	5.2	1894
Glasgow, Mont.	75.0	6.1	1893
Great Falls, Mont.	72.4	5.3	Before 1900
Havre, Mont.	72.9	4.9	1879
Sheridan, Wyo.	73.1	4.5	1907
Seattle, Wash.	69.3	4.1	1892
Portland, Oreg.	72.2	3.8	1902

[1] Reference to the United States in this paper will not include Alaska or Hawaii.

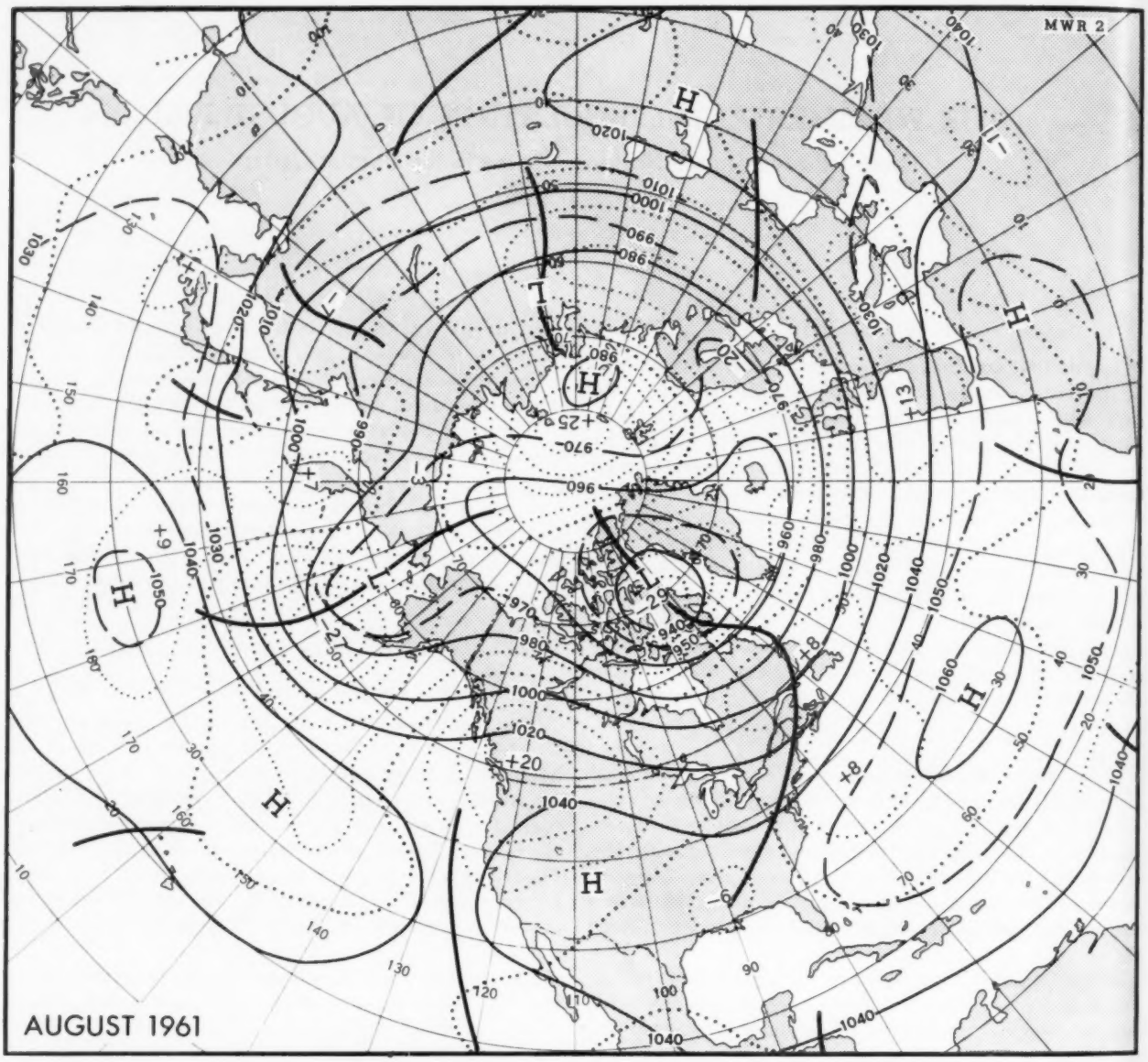

FIGURE 1.—Mean 700-mb. contours (solid) in tens of feet, and departures from normal (dotted) in 50-ft. intervals, for August 1961. Important circulation features were the unusually strong ridge over western North America and deep trough over southeastern United States.

TABLE 2.—*Maximum temperatures during August 1961 which equaled or exceeded previous highest recorded for any month.*

Station	Temperature (°F.)	Date
Helena, Mont.	*103	5
Kalispell, Mont.	105	5
Missoula, Mont.	105	4
Havre, Mont.	111	5
Boise, Idaho	110	4
Spokane, Wash.	*108	4
Pendleton, Oreg.	113	4

*Equaled previous record.

maximum temperature records as shown in table 2. In addition to the stations listed, a record high August temperature of 115° F. was reported at Lewiston, Idaho on the 4th. Nights were also unusually hot in the northern Plains where minima were occasionally in the mid-70's.

August continued the series of dry months that has left soil moisture reserves at a critically low level. At Williston, N. Dak., only 10 percent of the normal moisture fell, the driest August since observations began in 1878. Much of the precipitation in the Northwest was in the

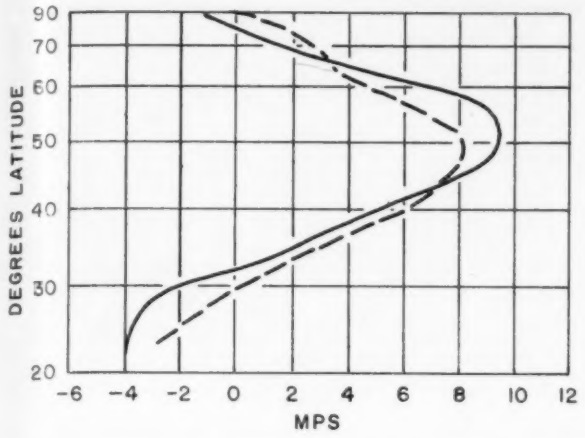

FIGURE 2.—Mean 700-mb. zonal wind speed profiles in the western portion of the Northern Hemisphere for August 1961 (solid) and August normal (dashed). The middle-latitude westerlies were stronger than normal and displaced northward.

form of widely scattered light showers which failed to add to soil moisture reserves.

Drought conditions in the Northwest were related to the abnormally strong ridge and area of positive 700-mb. height anomaly over western North America (fig. 1). Advection of vorticity from the deep mid-Pacific trough strengthened this ridge, normally found over western North America during the summer months. The westerlies, displaced some 10° north of their normal position over western Canada (fig. 3A), diverted cool, moist Pacific air masses well to the north of the drought area. At the end of the month, however, progression of the long-wave pattern began, thus bringing an abrupt end to the heat wave in the Northwest along with the first substantial rains of the month to Washington and northern Oregon.

PERSISTENT COOLNESS IN THE MIDWEST AND SOUTH

This was the fifth consecutive month that temperatures have averaged below normal in the area from the central Plains to the Appalachians and southward to the lower Mississippi Valley (fig. 1 in [1] and fig. 4). Greatest departures during August, as much as −4° F., were observed in eastern portions of the central and southern Plains. This was the coolest August of record at Shreveport, La., and Austin and Midland, Tex. Daily temperatures averaged below normal on nearly every day of the month in the west Gulf States with some cities, such as Jackson, Miss. and Shreveport, La., never exceeding normal.

These cool conditions were related to the trough over the Southeast and its associated large area of negative 700-mb. height anomaly (fig. 1). Furthermore, this circulation favored the unusually far southward displacement of cold fronts with their attendant cool air masses.

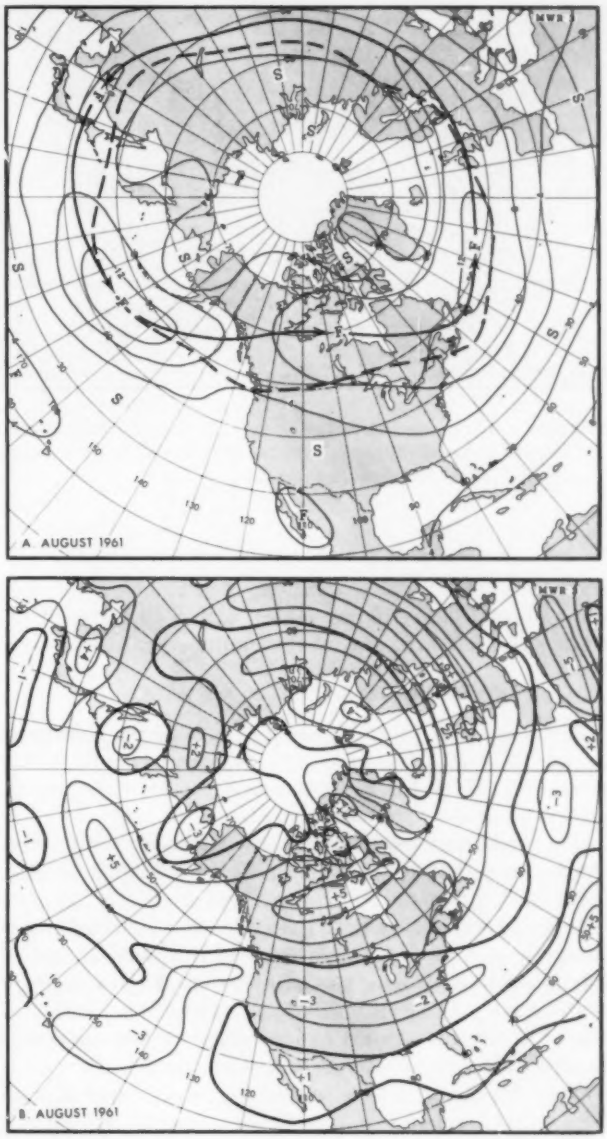

FIGURE 3.—(A) Mean 700-mb. isotachs, and (B) departures from monthly normal wind speeds, both in meters per second, for August 1961. Solid arrows in (A) indicate principal axes of maximum wind speeds, and dashed arrows their normal August positions. The westerlies over North America were displaced north of normal.

The distribution of precipitation bore a nearly typical relationship to the 700-mb. circulation. Less than normal amounts fell generally west of the mean trough while greater than normal amounts fell east of the trough in stronger than normal southerly flow (figs. 1, 5). Following two months of excessive precipitation, central Texas was unusually dry with the Dallas-San Antonio areas receiving less than 10 percent of their normal amounts. Frequent

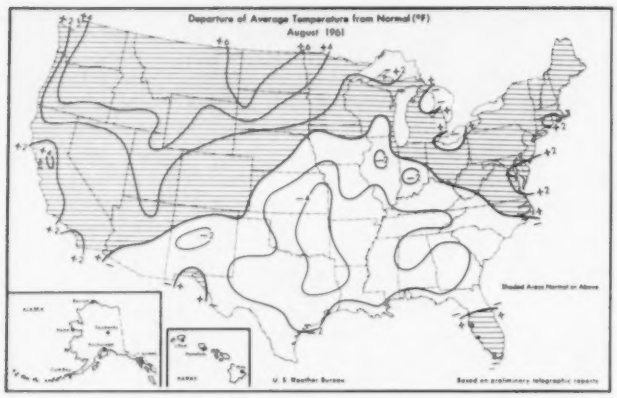
Departure of Average Temperature from Normal (°F)
August 1961
Shaded Areas Normal or Above
U. S. Weather Bureau
Based on preliminary telegraphic reports

FIGURE 4.—Departure of average surface temperature from normal (°F.) for August 1961. A strong temperature anomaly gradient prevailed in the Midwest. (From [8].)

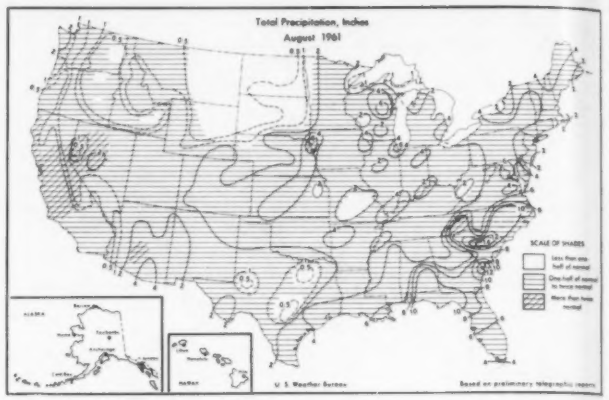

FIGURE 5.—Total precipitation (inches) for August 1961. The Northern Plains were very dry. (From [8].)

showers in the South Atlantic States resulted in many rainy days (0.01 inch or more) with Charleston, S.C., having 19 such days, the greatest number in August since 1898.

WEATHER ELSEWHERE IN THE NATION

A warm wet weather regime prevailed in the Southwest during August. Temperature departures were rather small, +2° F. or less in most areas (fig. 4), while precipitation amounts were mostly greater than normal.

The Southwest moist tongue was unusually active with shower and thunderstorm activity very frequent. Ely, Nev., had 24 days with thunderstorms, the greatest number of days with thunderstorms ever recorded there in any month in any year. Some of this activity spread into California where precipitation in August is very uncommon. The warm showery weather in the Southwest was associated with above normal mid-tropospheric heights and easterly anomalous flow (fig. 1).

The Northeast was also warmer than normal with temperature departures mostly less than 2° F. (fig. 4), while precipitation was generally near normal. In New England, the first 20 days of the month were very dry, the result of westerly anomalous flow in mean trough conditions over the area. During the latter part of the month this trough retrograded and weakened. As a result south and southeasterly anomalous flow became established, accompanied by frequent periods of precipitation. Most of the month's total rainfall fell at this time.

4. TROPICAL STORM ACTIVITY

During any August one or more tropical storms can be expected to develop in the Caribbean or North Atlantic [2], but none occurred in August 1961. It is generally considered that tropical storm development is related to the strength and position of the middle-latitude westerlies [3]. During this August the average circulation appeared quite favorable for generation of such storms. The 700-mb. height anomaly pattern agreed quite closely with the findings of Ballenzweig [4] for maximum storm occurrence. Furthermore, the associated upper-level westerlies were displaced north of normal (fig. 3A). It is evident that some of the basic elements necessary for tropical storm development were missing.

Tropical storm activity was confined primarily to the western Pacific, where four storms developed, three of which reached typhoon intensity.

Typhoon June developed near 12° N., 133° E. on the 1st. This storm moved steadily northwestward, losing much of its strength as it passed over Taiwan on the 6th, finally dissipating after moving into China on the 8th. Typhoon Kathy first appeared near Iwo Jima on the 15th. It also moved northwestward, striking Kyushu, Japan, on the 17th before filling on the 18th. The largest and most intense storm was typhoon Lorna. First appearing near 16° N., 129° E. on the 20th, Lorna grew rapidly to typhoon intensity. Moving northwestward Lorna's "eye" passed over southern Taiwan on the 24th, reached the China coast on the 25th, and dissipated inland on the 26th.

Tropical storm Marie developed near 23° N., 153° E. on the 29th. This storm moved slowly northward, turned on a westerly course and dissipated early in September, never reaching typhoon strength nor threatening any land areas.

5. THE SUMMER IN REVIEW

Summer of 1961 in the United States was characterized by contrasting regimes of weather associated with an abnormal mid-tropospheric circulation. In figure 6 are shown (A) the average circulation at 700 mb., (B) the departure of average surface temperature from normal, and (C) the total precipitation, for the months of June, July, and August.

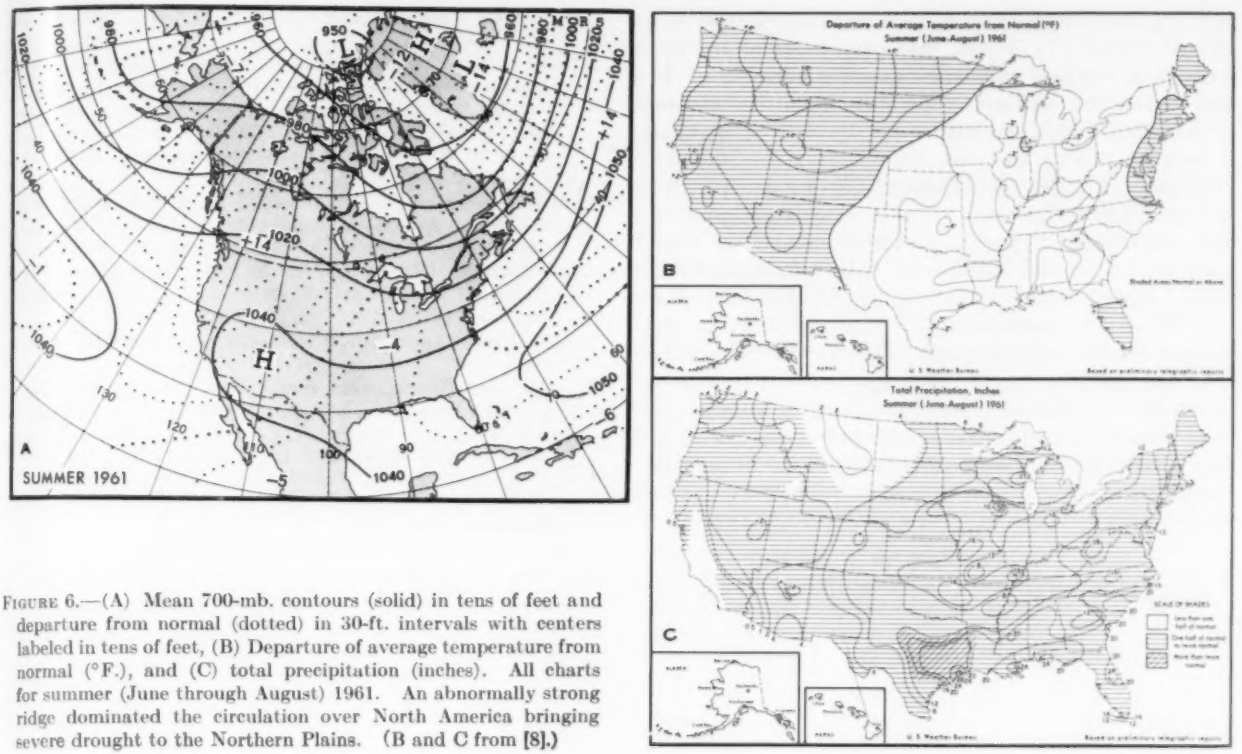

FIGURE 6.—(A) Mean 700-mb. contours (solid) in tens of feet and departure from normal (dotted) in 30-ft. intervals with centers labeled in tens of feet, (B) Departure of average temperature from normal (°F.), and (C) total precipitation (inches). All charts for summer (June through August) 1961. An abnormally strong ridge dominated the circulation over North America bringing severe drought to the Northern Plains. (B and C from [8].)

Unseasonable warmth prevailed throughout most of the western half of the Nation with greatest temperature departures, 4° F. or more, in the Northwest (fig. 6B). This was the warmest summer ever recorded in Walla Walla, Wash. since observations began in 1886. Kalispell, Mont., with a record dating to 1899, also had its warmest summer. Near record warmth was observed elsewhere in the Northwest.

Extreme dryness also prevailed in the area of greatest warmth. At Billings, Mont. this was the driest summer on record, while Devils Lake, N. Dak. experienced its second driest summer.

This hot dry weather regime was accompanied by increasing drought in the Northern Plains, conditions being most severe in northwestern North Dakota and eastern Montana. An index to measure drought severity has recently been developed by Palmer [5]. The index values depend on the temperature and precipitation during each month, the weather during preceding months, the climate of the place being studied, and the duration of the abnormally dry weather. At the end of May 1961 the drought index for northwestern North Dakota was —0.60 (incipient drought stage). By the end of August the index had reached —4.20, comparable to the extreme drought of 1934 when the drought index was —4.17 at the end of August.[2] Crop correspondents of the Department of Agriculture, in their report of September 11, 1961 [6], considered that extreme drought conditions existed in eastern Montana and the western Dakotas.

The tendency for summer drought to follow a warm dry spring in the Great Plains has been shown by Namias [7]. This year appears to be no exception since spring was warm and generally dry in the Northern Plains [8]. Furthermore, these conditions have existed since summer 1960, as is substantiated by the Palmer index which had been at the incipient to mild drought stage since that time.

In marked contrast with the West, most of the eastern half of the Nation enjoyed a cooler than normal summer. Greatest temperature departures (as much as 4° F. in some areas) and near record coolness were observed in the South (fig. 6B). It was the coolest summer ever reported at Baton Rouge, La. in a record dating to 1893, while at Abilene, Tex., this was only the second summer since 1886 that the temperature has failed to reach 100° F.

Precipitation averaged somewhat greater than normal in much of the East and South, with a large area in eastern and central Texas receiving more than two to three times the normal amount (fig. 6C). Most of the latter precipitation fell during June [9] and July [1].

Comparison between the mean 700-mb. circulation pattern for August 1961 (fig. 1) and that for summer of this

[2] A value of —4.00 is considered to be the threshold between severe and extreme drought.

year (fig. 6A) shows them to be remarkably similar in the United States. It follows that persistence of the circulation and weather anomalies was also very high. It is well known that surface temperature anomalies and mid-tropospheric height anomalies are most directly related in summer. Note the close "fit" during the summer of 1961 (figs. 6A, B). The abnormally strong ridge over western North America, with its associated subsidence and northward displaced westerlies tended to inhibit precipitation in the Northwest, with less than half the normal seasonal amounts falling over the Northern Plains (fig. 6C). An examination of the file of 700-mb. mean summer charts in the Extended Forecast Branch discloses that the positive height anomaly center over western North America during this summer was the strongest and most extensive positive anomaly ever observed in this area. Retrogression and deepening of the trough normally found along the east coast in summer was effected primarily by the unusually strong ridge to the west.

REFERENCES

1. R. A. Green, "The Weather and Circulation of July 1961," *Monthly Weather Review*, vol. 89, No. 10, Oct. 1961, pp. 414-418.
2. G. E. Dunn, "Tropical Cyclones," *Compendium of Meteorology*, American Meteorological Society, Boston, 1951, pp. 887-901.
3. H. Riehl, "On the Formation of West Atlantic Hurricanes," Part I of "Studies of Upper-Air Conditions in Low Latitudes," Dept. of Meteorology, University of Chicago, *Miscellaneous Reports*, No. 24, 1948, pp. 1-67.
4. E. M. Ballenzweig, "Relation of Long-Period Circulation Anomalies to Tropical Storm Formation and Motion," *Journal of Meteorology*, vol. 16, No. 2, Apr. 1959, pp. 121-139.
5. W. C. Palmer, "Drought in Northwestern North Dakota," U.S. Weather Bureau, *Weekly Weather and Crop Bulletin, National Summary*, vol. XLVIII, No. 28, July 10, 1961.
6. U.S. Dept. of Agriculture, Statistical Reporting Service, Sept. 11, 1961.
7. J. Namias, "Factors in the Initiation, Perpetuation, and Termination of Drought," *Publication No. 51*, International Association of Scientific Hydrology, Commission of Surface Waters, (IUGG 1960 Meetings in Helsinki), pp. 81-94.
8. U.S. Weather Bureau, *Weekly Weather and Crop Bulletin, National Summary*, vol. XLVIII, Nos. 24, 36, and 37, June 12, September 4, 11, 1961.
9. L. P. Stark, "The Weather and Circulation of June 1961—A Hot, Dry Month in the West," *Monthly Weather Review*, vol. 89, No. 9, Sept. 1961, pp. 368-373.

Weather Note

EXCESSIVE RAINFALL IN THE MONTGOMERY, ALA. AREA ON AUGUST 31, 1961

ARTHUR R. LONG

Weather Bureau Airport Station, Montgomery, Ala.

[Manuscript received September 8, 1961]

A band of heavy thundershowers occurred in the Montgomery, Ala. area on the night of August 30–31, 1961.

At Montgomery the 65-year maximum 1-hour precipitation record of 3.81 in., which occurred on July 20–21, 1899, was broken when 4.16 in. fell between 3:10 a.m. and 4:10 a.m. CST, on August 31, 1961. For the 2-hour period 3:10 a.m. to 5:10 a.m., 4.51 in. fell, breaking the former 2-hour record of 4.38 in. set on November 9, 1927.

Several cooperative stations received heavy rainfall also, most of which fell between midnight and 7 a.m. on August 31. Some of the heavier amounts were: Mathews, 6.05 in.; Troy, 6.75; Brundidge, 4.13; Elba, 6.58; and Geneva, 5.64 in. At Milstead, Ala., a total of 11.50 in. fell during the 24-hour period ending at 11 a.m. on the 31st.

This excessively heavy rainfall caused considerable damage by flooding streets and residences in Montgomery and washouts on highways and one railroad in the surrounding area. Numerous highways were closed for periods of one to three days.

Publications by Weather Bureau Authors

H. S. Ayer, "On the Dissipation of Drainage Wind Systems in Valleys in Morning Hours," *Journal of Meteorology*, vol. 18, No. 4, Aug. 1961, pp. 560–563.

C. M. Boettger, "Air Pollution Potential East of the Rocky Mountains: Fall 1959," *Bulletin of the American Meteorological Society*, vol. 42, No. 9, Sept. 1961, pp. 615–620.

R. F. Dale (with R. H. Shaw), "Low Precipitation Observational Bias at Cooperative Climatological Stations," *Bulletin of the American Meteorological Society*, vol. 42, No. 8, Aug. 1961, pp. 561–570.

G. A. deMarrais, "Vertical Temperature Difference Observed Over an Urban Area," *Bulletin of the American Meteorological Society*, vol. 42, No. 8, Aug. 1961, pp. 548–554.

R. R. Dickson, "Meteorological Factors Affecting Particulate Air Pollution of a City," *Bulletin of the American Meteorological Society*, vol. 42, No. 8, Aug. 1961, pp. 556–560.

S. Fritz, " 'Cyclone-Prints' from Satellite (TIROS I)," *Interavia*, vol. 15, 1960, pp. 1384–1385.

K. J. Hanson, "The Albedo of Sea-Ice and Ice Islands in the Arctic Ocean Basin," *Arctic*, vol. 14, No. 3, Sept. 1961, pp. 188–196.

D. M. Hershfield, "Estimating the Probable Maximum Precipitation," *Proceedings of the American Society of Civil Engineers*, Sep. 2933, Sept. 1961.

L. Holloway, "Alignment Chart for Satellite Orbit Calculation," *Journal of the Astronautical Sciences*, vol. VIII, No. 2, Summer 1961, pp. 60–61.

D. Holmes and S. Teweles (with Other Members of Joint Scientific Advisory Group to the Meteorological Rocket Network), "The Meteorological Rocket Network—An Analysis of the First Year of Operation," *Journal of Geophysical Research*, vol. 66, No. 9, Sept. 1961, pp. 2821–2842.

N. F. Islitzer, "Short-Range Atmospheric-Dispersion Measurements from an Elevated Source," *Journal of Meteorology*, vol. 18, No. 4, Aug. 1961, pp. 443–450.

H. E. Landsberg, "Temperature Fluctuations and Trends Over the Earth," Correspondence, *Quarterly Journal of the Royal Meteorological Society*, vol. 87, No. 373, July 1961.

J. T. Lee and C. L. David, "Squall-Line Structure and Development as Depicted by Horizontal Traverses by the Tornado-Research Aircraft," *Bulletin of the American Meteorological Society*, vol. 42, No. 9, Sept. 1961, pp. 595–602.

J. D. McQuigg, "The Weather Bureau State Climatologist and His Service to Agriculture," *Weatherwise*, vol. 14, No. 4, Aug. 1961, pp. 154–157.

C. H. Pierce, "Boston—A Maritime City with a Continental Climate," *Weatherwise*, vol. 14, No. 4, Aug. 1961, pp. 138–141, 167–168.

M. J. Schroeder, "Down-Canyon Afternoon Winds," *Bulletin of the American Meteorological Society*, vol. 42, No. 8, Aug. 1961, pp. 527–542.

M. J. Schroeder, "Topometeorology—The Local Scale," Correspondence, *Bulletin of the American Meteorological Society*, vol. 42, No. 8, Aug. 1961, p. 590.

D. P. Springer, "Agricultural Meteorology—The New Science Team," *The Science Teacher* (Journal of the National Science Teachers Association), vol. 28, No. 3, Mar. 1961, pp. 6–10.

H. Wexler (with M. Neiburger), "Weather Satellites," *Scientific American*, vol. 205, No. 1, July 1961, pp. 80–94.

L. F. Whitney and S. Fritz, "A Tornado-Producing Cloud Pattern Seen from TIROS I," *Bulletin of the American Meteorological Society*, vol. 42, No. 9, Sept. 1961, pp. 603–614.

O. L. Wulf (with S. B. Nicholson), "The Diurnal Variation of K Indices of Geomagnetic Activity on Disturbed Days in 1940-1948," *Journal of Geophysical Research*, vol. 66, No. 8, Aug. 1961, pp. 2399–2404.

Recent Articles in Other Weather Bureau Periodicals

Mariners Weather Log, vol. 5

No. 5, September 1961:

"The Storm Surge," by N. Arthur Pore, pp. 151–156.

"The Hurricane's Central Pressure and the Highest Wind," by Raymond H. Kraft, p. 157.

Weekly Weather and Crop Bulletin, National Summary, vol. XLVIII

No. 33, August 14, 1961:

"Grasshoppers and the Weather," by A. Boyd Pack, p. 8.

No. 38, September 18, 1961:

"Hurricane Carla, September 4–14 (A Preliminary Report)," pp. 7–8.

No. 41, October 9, 1961:

"Has Drought Ended in Northern Great Plains?" by Wayne C. Palmer, p. 8.

"An Example of Crop Damage Due to Excessive Rainfall," by Albert V. Hardy, p. 8.

U.S. GOVERNMENT PRINTING OFFICE: 1961